

Dissertation
submitted to the
Combined Faculties for the Natural Sciences and for Mathematics
of the Ruperto-Carola University of Heidelberg, Germany
for the degree of
Doctor of Natural Sciences

Put forward by
Dipl.-Phys. Tobias Binder
Born in Braunschweig
Oral examination: 15.04.2014

Measurements of grain boundary networks in
deep polar ice cores

-

A digital image processing approach

Referees: PD Dr. Christoph Garbe
Prof. Dr. Kurth Roth

Abstract

Ice covers a significant part of the Earth's surface and is one key component of the global climate system. A thorough understanding of ice flow is crucial for modeling the response of ice sheets to past and upcoming climate changes. Glen's law, a experimentally derived exponential relationship between stress and strain rate, is usually applied. However, it does not adequately capture microstructural changes observed for high total shear strains and long time scales which cannot be reproduced by laboratory experiments. Deep ice cores provide insights into the natural evolution of microstructure (grain boundary networks). Large sets of sublimation groove images, mapping grain boundaries in high resolution, are available along the EDML (East Antarctica) and NEEM (Greenland) ice cores. A digital image processing approach has been developed to derive grain size, grain shape, shape of grain boundaries, and density of sub-grain boundaries in a consistent way. An automatic assignment to c-axes orientation measurements allows estimating the error of calculated parameters. Depth profiles along both ice cores are presented and interpreted based on variations in impurity content, temperature differences, and involved time scales. Furthermore, the presence of effective negative pressures caused by air bubbles and clathrate hydrates is taken into account.

Zusammenfassung

Eis bedeckt einen signifikanten Teil der Erdoberfläche und ist eine Schlüsselkomponente des globalen Klimasystems. Umfassende Kenntnisse des Eisfließens sind entscheidend für die Modellierung der Reaktion von Eisschilden auf vergangene und zukünftige Klimawechsel. Glens Gesetz, ein experimentell abgeleiteter Zusammenhang zwischen Spannung und Verformungsrate, wird üblicherweise verwendet. Jedoch erfasst dieser nicht die mikrostrukturellen Änderungen, die für hohe gesamte Schubverformungen und lange Zeitskalen beobachtet werden, welches durch Laborexperimente nicht reproduziert werden kann. Tiefe Eisbohrkerne geben Einblick in die natürliche Entwicklung der Mikrostruktur (Korngrenznetzwerke). Große Bilddatensätze von Sublimationskerben, die Korngrenzen hochauflösend abbilden, sind entlang der EDML (Ostantarktis) und NEEM (Grönland) Eisbohrkerne verfügbar. Eine digitale Bildverarbeitungs-Methode wurde entwickelt, um Korngröße, Kornform, Korngrenzform und die Subkorngrenzdichte systematisch zu bestimmen. Eine automatische Zuordnung zu gemessenen c-Achsen Orientierungen erlaubt es die Fehler der berechneten Parameter abzuschätzen. Tiefenprofile entlang beider Eisbohrkerne werden gezeigt und interpretiert auf Grundlage von Variationen im Staubgehalt, Temperaturdifferenzen und der beteiligten Zeitskalen. Daneben wird die Sogwirkung von Blasen und Klathrathydraten berücksichtigt.

Contents

1	Introduction	1
2	Image acquisition along ice cores	5
2.1	Introductory remarks	5
2.2	Characteristics of the analysis method	6
2.3	Sublimation groove mapping	10
2.3.1	Sublimation process	10
2.3.2	Image acquisition	11
2.3.3	Error estimation	15
2.4	C-axes orientation measurements	17
2.4.1	Optical anisotropy	17
2.4.2	Image acquisition	17
2.4.3	Error estimation	20
2.5	Combined method	21
3	Extraction of grains and grain boundaries	23
3.1	Introductory remarks	23
3.2	Previous studies	24
3.3	Boundary probabilities	25
3.3.1	Combination of different filters	25
3.3.2	Random Forest	26
3.3.3	Gradient/misorientation based	29
3.3.4	Error estimation	29
3.4	Segmentation of grains and grain boundaries	30
3.4.1	Seeded region growing	30
3.4.2	Extraction of bubbles	31
3.4.3	Error correction	33

4	Matching of grains and grain boundaries	37
4.1	Introductory remarks	37
4.2	Coarse matching	38
4.2.1	Affine transformation	38
4.2.2	Estimation of mismatches	41
4.3	Grain pairs and conglomerates of grains	43
4.3.1	Motivation	43
4.3.2	Bijjective mapping and candidates for extension	43
4.3.3	Verification of conglomerates	46
4.3.4	Error estimation	48
4.4	Exploitation of matching for error estimation	48
4.4.1	Invisible/unextracted grain boundaries	48
4.4.2	Artifacts among extracted sublimation grooves	50
4.5	Fine matching	53
5	Parameterization of grains and grain boundaries	55
5.1	Introductory remarks	55
5.2	Grain size	56
5.2.1	Previous studies	56
5.2.2	Grain size parameters	57
5.3	Sources of error in grain size parameterization	59
5.3.1	Invisible/unextracted grain boundaries	59
5.3.2	Artifacts among extracted sublimation grooves	60
5.3.3	Other sources of error	61
5.4	Potential for improvements	66
5.4.1	Image acquisition/combined method	66
5.4.2	Extraction of grains and grain boundaries	67
5.5	Grain shape	68
5.5.1	Previous studies	68
5.5.2	Grain shape factors	69
5.5.3	Error estimation	71
5.6	Grain boundary length and shape	72
5.6.1	Previous studies	72
5.6.2	Implemented parameters	73
5.6.3	Error estimation	74
5.7	Orientation of c-axes	75
5.7.1	Previous studies	75

5.7.2	Implemented parameters	76
5.7.3	Error estimation	77
6	Extraction of sub-grain structures	79
6.1	Introductory remarks	79
6.2	Sublimation grooves	80
6.2.1	Scientific relevance	80
6.2.2	Extraction	80
6.2.3	Applicability	83
6.2.4	Error estimation of sub-grain boundary density	86
6.3	C-axes misorientation	87
6.3.1	Scientific relevance	87
6.3.2	Preliminary results toward automatic extraction	88
6.4	Potential for improvements	88
6.4.1	Extraction of smooth directions of the gradient	88
6.4.2	Assignment of c-axis misorientations	90
7	Evolution of micro-dynamic properties with depth	93
7.1	Introductory remarks	93
7.2	Grain growth	93
7.2.1	Current models	93
7.2.2	Grain size	95
7.2.3	Influence of changing impurity concentrations	100
7.2.4	Grain size sensitivity and vertical strain rate	102
7.3	Densification	104
7.3.1	Current models	104
7.3.2	Pressurization of air bubbles	104
7.3.3	Clathration	106
7.3.4	Grain shape	107
7.4	Evolution of dislocation density	110
7.4.1	Current models	110
7.4.2	Grain boundary shape	110
7.4.3	Sub-grain boundary density	112
8	Summary	115
	References	119
	List of Figures	135

List of Tables	137
Acknowledgments	139

Chapter 1

Introduction

Ice covers a significant part of the Earth's surface and is one key component of the global climate system. Ice sheets represent large fresh water reservoirs and influence the evolution of sea level by changing flux of ice towards the coast and draining into the oceans. In addition, the mass balance of ice sheets is affected by changes in precipitation and thus snow accumulation. During the last decade the methods to quantify mass change in polar ice sheets has been greatly improved. A recent inter-comparison combining different remote sensing techniques (Shepherd *et al.* , 2012) shows that East Antarctica is gaining mass at an average rate of 14 ± 43 Gt/yr between 1992 and 2011. However, the West Antarctic Ice Sheet and the Antarctic Peninsula are increasingly losing mass. Due to uncertainties in the measurement methods it is not yet clear whether Antarctica as a whole is gaining or losing mass. Between 1958 and 2007 the Greenland Ice Sheet gained mass at a rate of 469 Gt/yr on average (Ettema *et al.* , 2009), with an uncertainty of 20% (Howat *et al.* , 2011). Considering these uncertainties, a thorough understanding of ice flow is crucial for modeling the response of ice sheets to past and upcoming climate changes.

Previous climate changes have left their fingerprints, among others, in the form of stratigraphic variability in ice sheets. In central Antarctica counting of annual

layers along ice cores is not feasible as annual cycles are barely distinguishable (Ekaykin *et al.* , 2002). Instead, one-dimensional ice flow models are used to derive the age as a function of depth (Parrenin *et al.* , 2007). An improved understanding to which degree and on which time scale flow induced disturbances in the layering may occur is crucial for the interpretation of ice-core paleoclimate records (Faria *et al.* , 2010).

To model large-scale ice flow, Glen’s law (Glen, 1955) is usually applied. This law is an experimentally derived exponential relationship between stress and strain rate and is, strictly speaking, only applicable in the secondary-creep stage between 0.5% and 2% strain (Budd & Jacka, 1989). For higher strain the ice is in the state of tertiary creep, which is associated with microstructural changes. This regime is characterized in particular by the rotation of the crystallographic c-axes towards the direction of compression, which leads to a strong anisotropy in flow properties (Azuma & Higashi, 1985). The latter can be explained by the high mechanical anisotropy of single ice crystals. They can in principle deform by glide of dislocations on all geometric planes of the crystal lattice, (Hirth & Lothe, 1992; Weertman & Weertman, 1992), but the stress required to deform a crystal by basal slip is about 60 times lower than by non-basal slip at similar strain rates (Duval *et al.* , 1983). Mean-field approaches facilitate upscaling from micro- to macro-scale (see review in Montagnat *et al.* , 2013). Their applicability depends strongly on the micro-dynamic basis. The deformation of polycrystalline ice with homogeneously distributed c-axes is characterized by the development of an internal stress field due to plastic incompatibility between grains (Ashby & Duval, 1985; Duval *et al.* , 1983; Castelnau *et al.* , 2008). A preferred orientation of c-axes suppresses the generation of internal stresses. In large scale models simulating ice sheet flow, the effect of anisotropy is typically implemented by an enhancement factor (Faria *et al.* , 2013b, and references therein).

During deformation, magnitude and variation of internal stresses are reduced by dynamic recovery and recrystallization. Both reduce the stored strain energy of the polycrystal by re-arrangement of dislocations into low-energy structures

(e.g., sub-grain boundaries). Dynamic recrystallization includes, but is not limited to, the migration of grain boundaries into grains with a higher dislocation density. This process can potentially redistribute impurities embedded in the material (Zener drag, e. g., Olgaard & Evans, 1986). Impurities are of major importance, as these are interpreted as climate proxies in ice cores. As the impurity content in ice shows characteristic patterns that reflect climate signals (e.g. measured along the GRIP (Greenland) ice core; Fuhrer *et al.* , 1993), redistribution of impurities implies that the original climate chronology signal may potentially be disturbed. So far, not much attention has been paid to this possible error source as the onset of dynamic recrystallization is assumed to occur in the very deepest part of deep ice cores (e.g., De La Chapelle *et al.* , 1998; Montagnat & Duval, 2000). This assumption, mainly based on laboratory experiments (Duval & Castelnau, 1995), has been put in doubt by recent studies on firn (Kipfstuhl *et al.* , 2009) and deep ice cores (Weikusat *et al.* , 2009b; Faria *et al.* , 2013a,b). These studies suggest that grain boundary migration may be more important in shallower depths than previously assumed.

Deep ice cores drilled in Antarctica and Greenland as well as ice-penetrating radar measurements revealed multi-scale variability in stratigraphy, microstructure and impurities (Faria *et al.* , 2009). Recent studies suggest that this leads to strong variations in mechanical properties, which could be the reason for large-scale folding (NEEM community members, 2013). The mechanisms coupling multi-scale variability to mechanical properties are not yet clear, nor quantified. Small changes in chemical impurity concentrations seem to have a much stronger impact on the deformation behavior of ice in shallower depths than previously thought (Hörhold *et al.* , 2012). In addition, changing rheology due to variations in grain size might have been underestimated so far (De Bresser *et al.* , 2001).

Analysis of ice microstructure along deep ice cores has been performed since the mid 1960s (Camp Century, Greenland and Byrd, Antarctica) and has been mainly limited to calculation of average grain size and determining the eigenvalues of the c-axes distribution (Faria *et al.* , 2013a). These parameters have been used to

analyze the prevailing deformation processes throughout ice sheets. However, one reason for the lack of knowledge about the link between microstructure and rheology is that the few recorded parameters are insufficient for micro-dynamic studies. In particular, a parameterization of the strength and variability of internal stress fields is required. The extraction of highly resolved grain boundaries serves as basis for this parameterization and is achieved by mapping of sublimation grooves evolving on polished ice core section. This technique was initially applied to analyze the structure of firm and bubbly ice (Arnaud *et al.* , 1998) and was further developed by Kipfstuhl *et al.* (2006). To obtain an adequate quantification of multi-scale variability and mechanical implications, ice core sections have to be analyzed in high depth resolution.

The extraction of grain boundaries and parameterization of their properties from large data sets requires the application of automated image processing techniques. The development of a dedicated approach is the objective of this thesis. Automated evaluation allows for a systematic and objective comparison of the properties of grain boundary networks. Consequently, it is to show that variability along one ice core as well as between ice cores drilled at sites with different stress regimes and temperatures can be quantified by the developed techniques.

The stress regimes typical for natural ice bodies cannot be replicated by laboratory conditions due to differences in size and time scales (Sammonds, 1999). The introduction of parameters related to the strength and variability of internal stress fields might allow for resolving the discrepancy between experiments and natural observations. Based on this quantification, the present micro-dynamical basis used in mean-field approaches can be rethought, which will improve our ability to predict flow properties of ice and thus the behavior of ice sheets.

Chapter 2

Image acquisition along ice cores

2.1 Introductory remarks

The following description of image acquisition techniques focuses on microstructure images acquired along the EDML ice core (drilled between 2001 and 2006 in East Antarctica, Dronning Maud Land, 2774 m depth) and the NEEM ice core (drilled between 2008 and 2011 in Greenland, 2537 m depth). All sections are cut along the vertical core axis according to a cutting scheme which ensures that different analyses (including destructive ones) can be conducted continuously along the entire ice core.

The data set of microstructure images acquired along the EDML ice core comprises 300 sections, whereas 750 sections have been analyzed along the NEEM ice core. Image acquisition has been conducted by collaborators at the Alfred Wegener Institute (AWI) in Bremerhaven, Germany. The microstructure mapping technique (in the following referred to as *sublimation groove mapping*) applied to ice core sections of the EDML ice core is described in detail by Kipfstuhl *et al.* (2006). For analysis of the NEEM ice core a different, currently unpublished, technique has been applied. If not otherwise specified, details mentioned in the following can be traced back to personal communications.

A special feature of the NEEM data set is that, additionally to sublimation grooves mapping, *c-axes measurements* have been applied to the same set of sections. Furthermore, there are differences in storage conditions and camera systems in comparison with the EDML data set. Only recently, it has become possible to systematically analyze the influence of specific settings and procedures on the feasibility to extract, in the ideal case, identical grain structures from both methods. A discussion on the potential for improvements can be found in Section [5.4.1](#).

The author contributed substantially to the development of image processing techniques applicable to the mentioned data sets. Observations described in the following have been gained on that basis. However, a comparison to microstructure analysis of the alpine KCI ice core (drilled at Colle Gnifetti) showed that the dependence on the method is much stronger than on the ice core.

2.2 Characteristics of the analysis method

Quality of images

After drilling an ice core, various time-consuming processing steps are required before it is possible to acquire an image of the microstructure. This applies in particular to the preparation of polished ice core sections using a microtome. In progressively smaller intervals thin layers are shaved off from the surface. The acquisition of sublimation groove images (Section [2.3.2](#)) can be performed in the considerably shorter period of a few seconds. In various image analysis tasks in Earth sciences, the question arises as to whether an enormous effort (by means of image processing) should be placed on trying to recover a corrupted image if it is possible to acquire images of considerably better quality with little effort (Heilbronner & Barrett, 2013). This reasoning applies even to sublimation groove mapping because the enhancement of image quality achieved by readjusting the focus of the camera or repeated polishing of the surface can be checked directly.

Corrupted images can be caused, for instance, by condensation. Frequently encountered problems have stimulated and are still stimulating methodical improvements. For instance, a previous camera system (applied by Horn, 2009) has been replaced because of considerably uneven illumination. The drilling fluid utilized for drilling the EDML ice core affected the sublimation behavior at the sample boundary and is no longer in use. Nevertheless, artificial structures forming during ice core storage or sample preparation can still occur and call for automated corrections by the image processing approach (Section 3.4.3).

Pressure relaxation and ice core storage

Air bubbles are closed off at the firn-ice transition at approximately 100 m depth. Slowly, the bubble pressure approaches the overburden pressure. When ice has been exposed to 50 bars (at about 700 m depth) for millennia and is brought up to the surface pressure relaxation occurs (Gow, 1971). Based on the observation of cracks and splintering immediately after the removal of the overburden pressure, a depth range is denoted as *brittle zone*. Relaxation stresses in this zone are particularly high as pressurized air bubbles occur abundantly. At depths where the hydrostatic pressure in an ice sheet reaches the dissociation pressure of air hydrates (about 800 m) the transformation from air bubbles to air hydrates is expected to start (Miller, 1969). The transition from air bubbles into clathrate hydrates takes place as a slow diffusion process over millennia resulting in a broad depth range of coexistence (Cuffey & Paterson, 2010).

The brittleness was found to decline with time which is the reason for storing cores from the brittle zone for several months before processing. An important task for microstructure analyses is to estimate the possible change on the grain scale during relaxation. In the Greenland ice sheet bubbles exist in greater depths as the accumulation rate is higher. Consequently, the brittle zone of ice cores in Greenland is more extensive and higher relaxation stresses are expected.

Relaxation is measured on macroscopic scale by the decrease in density or the volume expansion. Highest relaxation rates have been observed for the brittle zone

(primarily as a result of expansion of pressurized air bubbles) and only minimal relaxation for the ductile zone below (Gow, 1971; Gow *et al.*, 1997). Miyamoto *et al.* (2009) analyzed the dependency of relaxation rates on the storage temperature. At -20°C and -50°C the time period required for a volume expansion of 5% were measured for different samples of the Dome Fuji ice core between 1000 m and 2500 m depth. For a storage temperature of -50°C the time periods are for all samples at least five times longer than for -20°C . The samples from 1000 m and 1200 m required less than a year at -20°C for 5% volume expansion, at greater depth (after disappearance of all bubbles) relaxation rates are significantly lower. Another finding by Miyamoto *et al.* (2009) was that the generation of tiny bubbles, cleavage cracks and the decomposition of air hydrate crystals can be avoided effectively at a storage temperature of -50°C .

The present NEEM ice core has been stored at temperatures significantly higher than -50°C , during summer the storage temperature in the trench exceeded even -20°C . Therefore, extensive relaxation between 600 and 1160 m (the brittle zone) has become visible in the sublimation groove images by abundant occurrence of small grains in the vicinity of bubbles. Due to the limited extension of the brittle zone and lower storage temperatures the relaxation effect on the microstructure of the EDML ice core is expected to be less pronounced.

Sample preparation

The Polishing of ice core section is performed by a microtome (Kipfstuhl *et al.*, 2006). Scratches in the microtome blade (which can be caused, e. g., by dust particles on the surface) result in line structures on the polished surface. These artifacts can be identified on the basis of their straightness and orientation as samples are always moved along the (vertical) core axis under the blade.

Crystallographic information versus depth resolution

Sublimation groove mapping and c-axes orientation measurements (Section 2.4.2) with the latest equipment have in common that the time required for the acquisi-

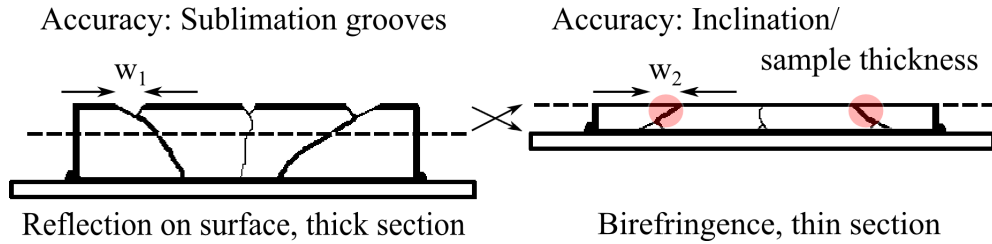


Figure 2-1: Combined application of the methods *sublimation groove mapping* (left) and *c-axes orientation measurements* (right) to one ice core section. Accuracy in the position of grain boundaries is quantified by measurable widths $w_1 \approx 0.02$ mm and $w_2 \approx 0.10$ mm. Drawings not to scale.

tion of microstructural information on 6×9 cm² sections is shorter or similar to that for sample preparation. This was not feasible in the past (e. g., Thorsteinsson *et al.* , 1997) and enables high depth resolution.

The disadvantage of sublimation groove mapping is that crystallographic information is generally not accessible. To compensate for this, all sections from the NEEM ice core were also analyzed by an automated c-axis fabric analyzer. For this purpose, additional processing of the reverse side of the sections is required (see Fig. 2-1 for a brief overview. The details are discussed in Section 2.5).

Both methods differ substantially from each other in image acquisition techniques as well as factors limiting the accuracy in the position of grain boundaries. Along the NEEM ice core, sublimation groove evolving on the surface of thick sections have been mapped by means of reflection microscopy. In this case, the width of grooves (w_1) reflects the accuracy in the position of grain boundaries. In contrast, the accuracy for measurements utilizing birefringence of light passing thin sections (as in c-axes orientation measurements) is given by the inclination of the grain boundary surface (w_2). w_1 and w_2 represent measurable widths facilitating a quantitative comparison of accuracy. Further details are described in the next two Sections.

The achieved diversity of observed microstructures would be by far unachievable, if the full crystallographic orientation (c- and a-axis) or the volume extension of grains and grain boundaries were recorded by methods like *Electron Backscat-*

ter Diffraction (EBSD, Weikusat *et al.* , 2011a). However, these methods are amongst others crucial for an improved understanding of the effect of inclusions (air bubbles, air hydrates, solutes, dust particles) on the microstructure.

2.3 Sublimation groove mapping

2.3.1 Sublimation process

Sublimation of ice surfaces is similar to chemical or thermal etching of surfaces of metals, minerals or ceramics. Following the theory of thermal grooving (Mullins, 1957) for metal polycrystals, grain boundary grooves form an equilibrium between the two surface tensions and the grain boundary tension. The produced sharp ridges are further flattened by preferential evaporation and surface diffusion. First studies of ice etching and dislocation etch pits were conducted by Kuroiwa & Hamilton (1963). Surface sublimation was initially utilized to analyze the structure of firn and bubbly ice (Arnaud *et al.* , 1998) and was further developed by Kipfstuhl *et al.* (2006) to capture various microstructural features on the grain scale. The term *microstructure mapping* employed by Kipfstuhl *et al.* (2006) for this method is a synonym for *sublimation groove mapping* used in the following to clearly differentiate it from *c-axes orientation measurements*.

The sublimation behavior depends on air temperature and humidity. In an ice laboratory both parameters can be kept constant. As this is not the case at drill sites, differences in the sublimation behavior and consequently the image quality can occur. As mentioned before, ice core storage at “warm” drill sites (and subsequent analysis under controlled conditions) induces changes of the grain structure. The sublimation groove mapping along the EDML and NEEM ice core has been performed at the drill sites. Special care has been taken not to pollute or touch the polished surfaces. Even warm breath close to the sample surface can affect the sublimation process by condensation. The possibility of disturbances can only be reduced but not completely excluded, i. e. some artificial structures may be visible in the images.

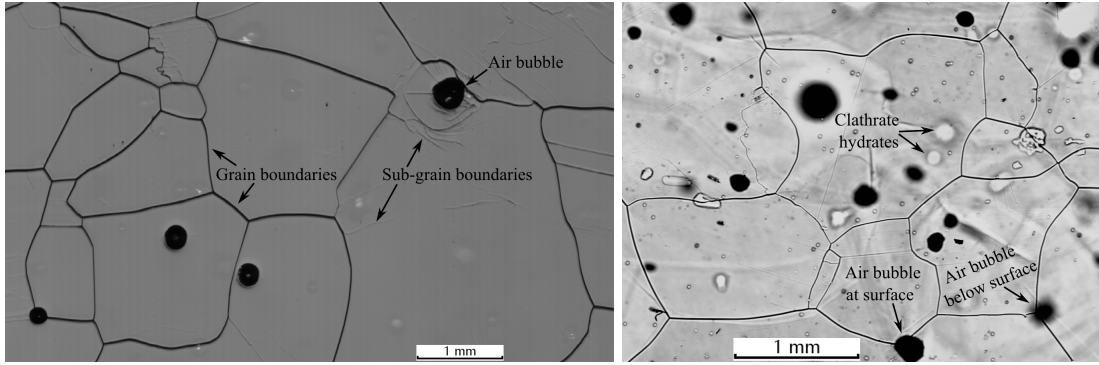


Figure 2-2: Visible features in an image from the NEEM ice core (322 m, left) and one from the EDML ice core (996 m, right).

Limited X-ray Laue diffraction measurements have provided full crystallographic misorientation values at the site of sublimation grooves (Weikusat *et al.*, 2011b). The combination leads to the conclusion that sublimation groove mapping is sensitive to grain boundaries as well as to different sub-grain boundary types.

2.3.2 Image acquisition

Illumination methods, width of sublimation grooves

Different illumination methods have been utilized to map sublimation grooves. Grain boundaries along shallow cores drilled at Vostok (East Antarctica) were analyzed in coaxial reflected light (Arnaud *et al.*, 1998) as differences in surface orientation lead to differences in contrast. Direct bright-field illumination, developed by Schäfter+Kirchhoff GmbH and applied along the NEEM ice core, also represents reflected illumination, i. e. coalignment of the light source and the camera. In contrast, the method described by Kipfstuhl *et al.* (2006) and applied along the EDML ice core utilizes transmitted illumination. Examples for images of the NEEM and the EDML ice core are shown in Fig. 2-2. Grain boundaries, sub-grain boundaries and air bubbles truncated at the surface are visible in both data sets. Owing to a depth of field of at least 0.3 mm, air bubbles just below the surface and clathrate hydrates are accessible in the EDML data set. The apparent width of sublimation grooves (denoted by w_1 in Fig. 2-1) covers a range between 0.01 and 0.04 mm.

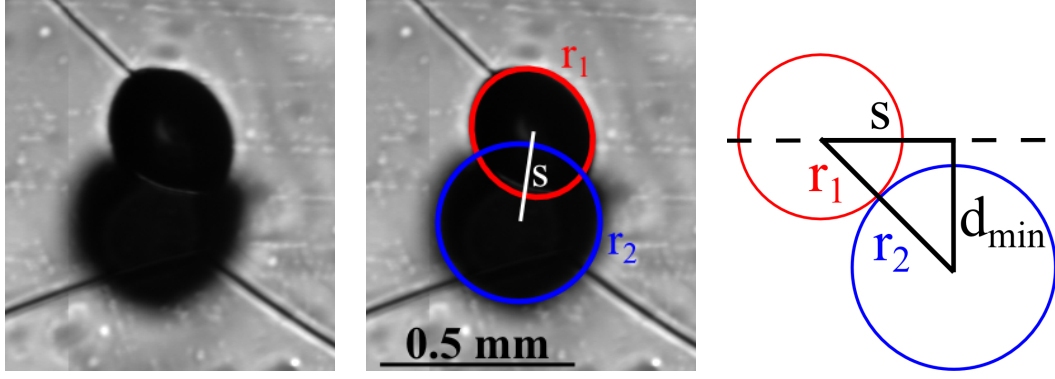


Figure 2-3: Assuming spherical shape of two overlapping bubbles (EDML, 206 m) allows to estimate the minimal depth of field d_{min} . Original image (left), manual fit of cross-sections (middle) utilized to determine r_1 , r_2 and s , assumption of bubble extension perpendicular to the image plane (right).

Differences in depth of field, focusing

The mentioned estimation of depth of field for the transmission microscopy system is derived from two overlapping air bubbles from an image at 206 m depth (EDML) as shown in Fig. 2-3. Similar to the approach developed by Ueltzhöffer *et al.* (2010), spherical shape is assumed. If the spheres of both bubbles are complete and at shortest possible distance, the minimal distance d_{min} between the visible cross-sections (the minimal depth of field) is given by Eq. 2.1. In this specific case, values for r_1 , r_2 and s have been obtained manually. An estimation of d plays an important role for quantifying the stronger impact of visible pore space on grain size calculations along the EDML ice core compared to the NEEM ice core (Section 5.3.3). Additionally, an automatic differentiation between bubbles on the surface characterized by sharp edges and bubbles exhibiting blurred edges below the surface is implemented.

$$d \geq d_{min} = \sqrt{(r_1 + r_2)^2 - s^2} = \sqrt{(0.171 + 0.210)^2 - 0.233^2} \cdot \text{mm} \approx 0.3 \text{ mm} \quad (2.1)$$

Prior to this work, transmitted illumination was chosen with the aim of a system-

atic analysis of inclusions along deep ice cores. Variations in size, number and arrangement of air bubbles have been quantified (Ueltzhöffer, 2009; Ueltzhöffer *et al.*, 2010; Bendel *et al.*, 2013). Micro-inclusions, air hydrates and slip bands can be analyzed with this method as well (e. g., Faria & Kipfstuhl, 2004; Faria *et al.*, 2010).

Focus on the systematic analysis of grain boundaries has been laid by Weikusat *et al.* (2009b); Kipfstuhl *et al.* (2009). The direct bright-field illumination integrated in a *large area scanning microscope* (LASM) facilitates a more efficient analysis and will be applied for the mapping of grain boundary grooves in the future. By that, a line-scanning device is employed and the efficiency is increased as it is no longer necessary to stitch typically 1500 overlapping micrographs acquired with an xy stage (Ueltzhöffer, 2009). The different illumination methods applied along the EDML and NEEM ice cores require slight modifications of the image analysis approach to extract grain boundaries and grain sizes.

Both camera systems have in common that the focus has to be adjusted manually. As sections have a (slightly) different height, it has not been feasible to scan all 750 sections from the NEEM ice core with uniform focus. The same applies to the sections from the EDML ice core. Occasionally, the focus has been re-adjusted while one of the micrographs was recorded.

Resolution of camera systems

The resolution is determined by means of repeated mapping of millimeter measuring tapes. Measurements on the microscope stage applied for analysis of the EDML ice core yielded a resolution of 307 ± 1 pixel/mm independent of the direction. The line-scanning device applied for analysis of the NEEM ice core is characterized by a resolution of 193.5 ± 1 pixel/mm perpendicular to the scan direction. As sections of the NEEM ice core are scanned in two overlapping parts displaced perpendicular to the scan direction, the occurrence of small-scale fluctuations parallel to the scan direction can be analyzed. The maximum deviation amounts to 30 pixels within less than a millimeter as shown in Fig. 2-4. However,

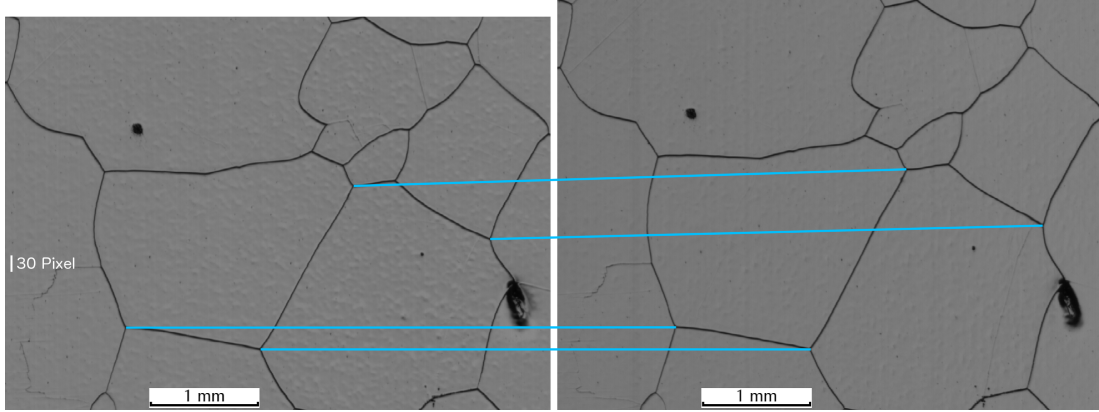


Figure 2-4: Sections of the NEEM ice core are scanned in two overlapping parts (left/right). Maximum deviation found in a NEEM section, 2131 m.

the deviation in more than 99% of all stitched image pairs is less than 1 pixel/mm as obtained by manual validation. The scanning speed is calibrated so that the resolution along the corresponding direction amounts to 200 ± 1 pixel/mm. The direction-dependent deviation in scaling of approximately 3% calls for a preprocessing step. However, at the point in time when this deviation was quantified most images of the NEEM data set had already been processed. In order to provide consistency, the direction-dependent scaling is taken into account in the context when coordinates are transformed to those of *c*-axes measurement (Section 4.2) assuming that the fabric analyzer exhibits isotropic scaling.

Gray values of mapped sublimation grooves, sub-grain boundaries

Thresholding on gray values to distinguish between grain boundaries and the inside of grains is feasible in images from the NEEM data set. The reason for this is that the distribution of mean gray values per (extracted) grain boundary covers less than half the range of possible values (0-255). Mean gray values per grain boundary extracted along the EDML ice core cover almost the entire range (Fig. 2-5).

Grain boundaries in ice exhibiting a full crystallographic misorientation of less than 5° are commonly referred to as sub-grain boundaries (e. g., Montagnat & Duval, 2000). This definition is utilized to identify sub-grain boundaries in the

NEEM data set and requires an assignment of crystallographic measurements (Section 4.3).

An approximate identification of sub-grain boundaries in the NEEM data set based on corresponding gray values is feasible if the distribution exhibits a peak at low gray values and a tail of higher gray values with significantly lower frequency (top row in Fig. 2-5). This applies for less than half of the acquired images. In a high number of cases, grain boundaries appear generally brighter and the distribution does not exhibit a noticeably high frequency at the lower end of gray values (bottom row). Here, setting a gray value threshold is not practicable. A lack of universal technical feasibility to identify sub-grain boundaries leads to an underestimation of mean grain size.

Weikusat *et al.* (2009b) transferred the conclusions drawn by an analysis of thermal groove geometry in ceramic polycrystals (Saylor & Rohrer, 1999) to the EDML data set and employed the term *sub-grain boundary* to all shallow sublimation grooves. Following this approach, a global threshold (140 on 8-bit scale of gray values) in mean gray value per boundary is chosen in the present context to discriminate between grain and sub-grain boundaries in the EDML data set. Without any doubt, this definition, respectively, the choice termination of the threshold is arbitrary. Therefore, the discriminating is applied subsequent to all other processing steps and serves only as estimation for the influence on the mean grain size profile.

2.3.3 Error estimation

The quantification of errors, a benchmarking of the applied image acquisition and processing technique, requires ground truth data (not available) or a second, independent method. A central role here is played by the concurrent measurement of *c*-axis orientations as discussed in Section 2.5.

Errors caused by disturbances of the sublimation process (e. g., by the drilling fluid utilized for drilling the EDML ice core) and sample preparation range from

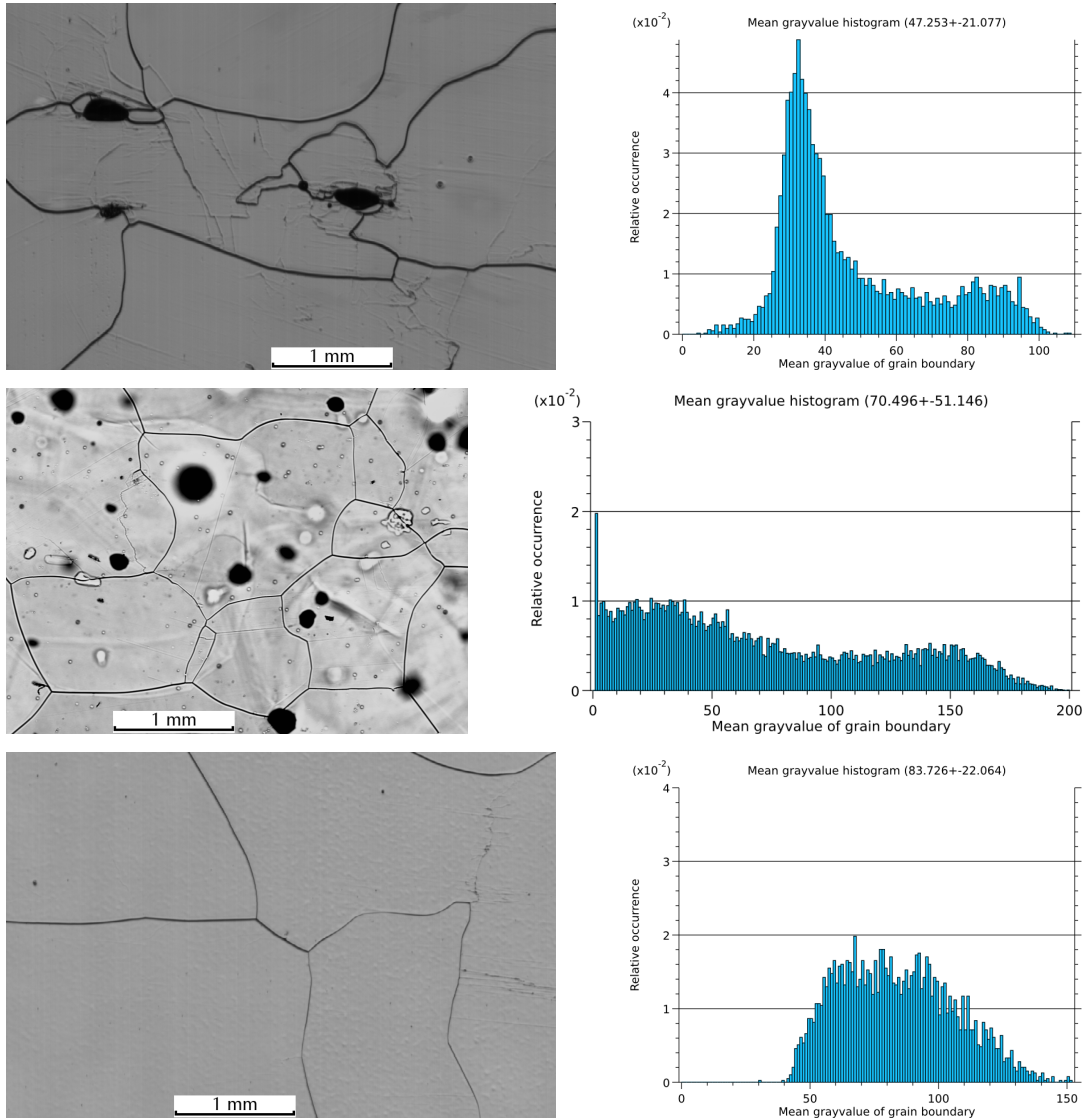


Figure 2-5: Thresholding on gray values to identify sub-grain boundaries is only possible in cases like shown in the top (NEEM, 1026 m) or middle (EDML, 996 m) row. Several NEEM images are similar to that shown in bottom row (NEEM, 2202 m). Right: Mean gray values of grain boundaries. This analysis is preceded by extraction of grain boundaries.

clearly identifiable structures to black lines hardly distinguishable from grain boundaries. The influence of both types of artifacts is reduced by manual, respectively, automatic corrections (Section 3.4.3). The influence of small grains created during ice core storage is reduced by the definition of a lower cut-off in grain size (Section 5.2.2).

Differences in the sublimation behavior and adjusted focus as well as in illumination predominantly affect the feasibility to discriminate between grain and sub-grain boundaries based on gray values.

2.4 C-axes orientation measurements

2.4.1 Optical anisotropy

The optical properties of ice are characterized by uniaxial anisotropy. As the c-axis forms the optical axis of the crystal, incident light is split into a component whose polarization is perpendicular to the c-axis and a component whose polarization is parallel to the c-axis. Those components propagate with different refractive indices and phase speeds through the crystal. Except the case of light propagating along the c-axis, a component of a linear polarized light beam is coupled into the plane perpendicular to the initial polarization and can pass a polarizer (referred to as analyzer). The intensity of light passing the analyzer depends on the orientation of the optical axis of ice with respect to the microscope table and the sample thickness.

2.4.2 Image acquisition

Fabric analyzer, thin sections

Automated c-axis fabric analyzers became available around the year 2000 (Wang & Azuma, 1999; Wilen, 2000). The G50 fabric analyzer (Wilson *et al.*, 2003) applied for c-axis measurements along the NEEM ice core utilizes nine LEDs arranged in a circle around the vertical axis as light source. For every pixel

the co-latitude (θ) and azimuth (ϕ) angles are acquired by a CCD camera by eight different alignments of the crossed polarizers. Both angles represent the full orientation of c-axes with respect to the microscope table. Additional information can be found in (Eichler, 2013), a Diploma thesis compiled in close collaboration with this work.

In contrast to the mapping of sublimation grooves, thin sections (about 300 μm) are required. The standard procedure for sample preparation is described by Langway, Jr. (1958), improvements have been proposed by Durand *et al.* (2006b). The latter emphasizes that (uniform) thickness of the section is an important parameter. On the one hand, the accuracy in grain boundary position is limited by the thickness, but on the other hand, the intensity of light passing the analyzer necessitates a minimal thickness of the section.

Spatial resolution, grain boundary position

The limited accuracy in grain boundary position originates from the inclination of grain boundary surfaces within the thin section. This explains why the extraction of grain boundary networks from c-axes orientation measurements is often considered as a by-product (Wilén *et al.*, 2003). In contrast to previous versions of the fabric analyzer, pixel-wise *quality* estimations are provided. Low quality values represent inconsistent information obtained for different illumination/alignments of the crossed polarizers in the vicinity of grain boundaries. In firn and in ice close to the firn-ice transition, air bubbles possessing an extension similar to the thickness of the sample are found. At these sites the inaccuracy in grain boundary position is further increased.

The mask applied to c-axis measurements in the context of segmentation of grains (Section 3.4.1) is mainly based on the quality estimates. The width of excluded pixels (denoted by w_2 in Fig. 2-1) covers a range between 0.06 and 0.3 mm along grain boundaries and more than 1 mm at air bubbles as shown in Fig. 2-6. The range of $0.06 \text{ mm} \leq w_2 \leq 0.3 \text{ mm}$ corresponds approximately to an inclination of the grain boundary surface against the surface of the section between 45° and

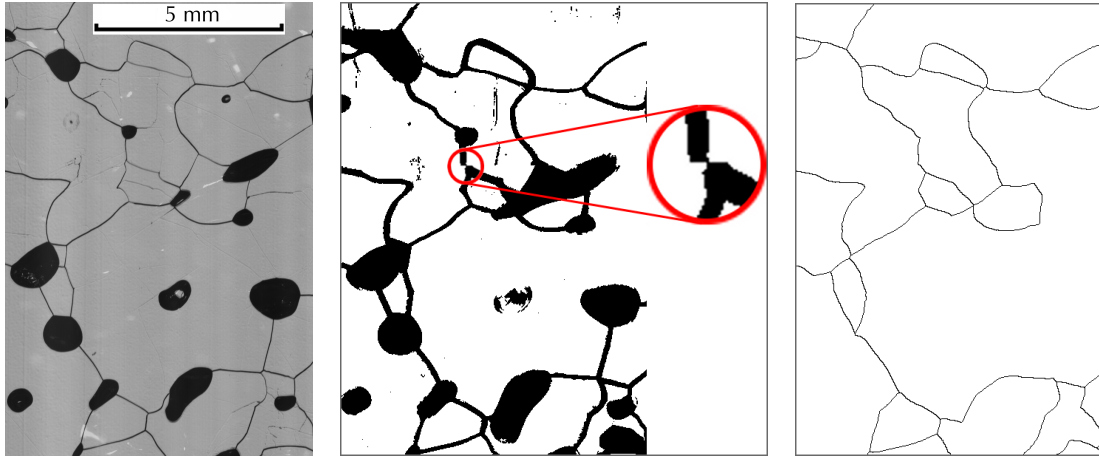


Figure 2-6: Comparison between width of grain boundary sublimation grooves (left), width of excluded pixels in c-axes measurements (middle) - mismatch at the border between two tiles is magnified, segmentation obtained from c-axes measurements (right). KCI-35_01.

79°. Even though the segmentation approach allows to reduce the width of grain boundaries, the difference in apparent width (in average: $w_1 \approx 0.02$ mm, $w_2 \approx 0.10$ mm) cannot be neglected. Mismatches of a few pixels occur at the border between two tiles exhibiting similar width than the boundary itself.

C-axes measurements have been performed at a resolution of 50 ± 1 pixel/mm. Acquisition at a higher resolution is technically feasible, but would consume much more time than in the present case where the time required for the acquisition of microstructural information on 6×9 cm² sections is similar to that for sample preparation. With the decrease in section quality with time in mind (Section 2.2) time exposure forms a critical factor for microstructure analysis along deep ice cores. However, the width of excluded pixels limiting accuracy is not expected to decrease significantly. A comprehensive study of resolution remains a task for future research. In the following, it is assumed that no direction-dependence of resolution occurs.

Angle resolution, denoising

Eichler (2013) performed measurements on two quartz monocrystals with prepared orientations to estimate the errors in co-latitude and azimuth angles. The

difference between the average measured value and the theoretical orientation of the crystal has been determined to be less than 3° . At tile borders differences in orientation of several degrees occur. In addition, measurements led to the conclusion that the noise of the co-latitude signal increases with θ . Both the discontinuities at tile borders and the noise in the co-latitude call for corrections.

To avoid artificial segmentation of tile borders, the calculation of misorientation (Section 3.3.3) is performed for each tile individually. The noise of the co-latitude signal is reduced by means of a 8-neighborhood median filter, which is one of the most widely applied method for this purpose (Heilbronner & Barrett, 2013). An extraction and parameterization of sub-grain structures based in c-axis measurements would necessitate an evaluation of the influence of this filter on derived misorientations. Even though the angle resolution and the current denoising technique allows extraction of grains and calculation of misorientations across long, closed grain boundaries extracted from the corresponding sublimation groove image (Section 4.4.2), a systematic analysis of internal misorientations is currently not feasible.

2.4.3 Error estimation

Errors in the position of grain boundaries extracted from fabric analyzer measurements could be quantified in more detail by matching them to grain boundaries extracted from sublimation grooves on the same sample (Section 4.4). As the more accurate grain boundaries (sublimation grooves) are consistently available, the inaccurate grain boundaries (c-axes measurements) available only along the NEEM are not considered any further. However, a similar estimation is performed in Section 4.2.2 by quantifying the mean deviation between matched grains originating predominantly from this inaccuracy.

Mismatches of a few pixels occur at the border between two tiles in the measurements acquired along the NEEM ice core (Fig. 2-6). Eichler (2013) traced this mismatch back to a slight rotation of the CCD camera with respect to the stage

axes. As a re-adjustment of the camera and re-measurement of the sections is not feasible, all recorded tiles have to be rotated individually. A rotation angle $\alpha = 0.4^\circ$ reveals the best compensation.

2.5 Combined method

Motivation

Strengths and weaknesses of sublimation groove mapping and c-axis orientation measurements suggest to develop a combined method. Highly resolved grain boundaries and high sensitivity to sub-grain boundaries combined with information on the c-axes orientation approximate the information accessible by methods like EBSD which cannot be applied at a set of sections of similar size. Numerical simulations of microstructural development apply similar representations and transferability is crucial to adapt them to nature (e. g., Elle: Jessell *et al.* , 2001; Jessell & Bons, 2002; Bons *et al.* , 2008). However, full crystallographic orientation, in particular the a-axes orientation, cannot be revealed. As dislocation glide perpendicular to the c-axis (on the basal plane) is energetically favored by a factor 60 (Duval *et al.* , 1983) the c-axis orientation is of major interest in deformation studies.

Preparation of a thin section

As shown in Fig. 2-1, the surface on which sublimation grooves have been imaged is frozen onto a second glass plate. The (first) glass plate fixed to the opposite side is detached. The subsequent steps, i. e. the preparation of a thin section utilizing a band saw and a microtome, are conducted following Langway, Jr. (1958).

Error estimation

In case of a combination of different methods, results have to be evaluated in terms of a distinction between accumulation and reduction of error. Furthermore, the transformation of structures from one image type to another generates an additional error: the inaccuracy of the transformation. In the ideal case, this

inaccuracy is intimately linked and, therefore, indistinguishable from errors in the position of grain boundaries extracted from fabric analyzer measurements. As measured mismatches depend on the data base, the portion of matched grains plays an important role to characterize the quality of a transformation (Section 4.3.3).

The matching of grains and grain conglomerates extracted from both analysis types facilitates the validation of grain boundaries extracted from sublimation groove images (Section 4.4). Sub-grain boundaries can be characterized by not being extracted from the fabric analyzer measurements and low misorientations of c-axes between both sides. In case of vanishing misorientations, the segmented boundary represents possibly an artifact hardly distinguishable from grain boundaries and, therefore, detected by none of the methods utilized for error correction (Section 3.4.3).

Artifacts like scratches created during sample preparation affect both methods. As they are automatically identified in the sublimation groove images, the counterparts extracted from the fabric analyzer measurements can be identified utilizing the matching of grain conglomerates.

Chapter 3

Extraction of grains and grain boundaries

3.1 Introductory remarks

The techniques described in the following have been adjusted/developed to process the data sets introduced in Chapter 2. As further explained in Sections 3.3.2 and 3.3.4, rankings of feature importance and validation data have been used to obtain a configuration which enables a robust and consistent processing of complete data sets. A motivation for choosing every applied filter/operator is provided. However, if not otherwise specified, the influence of parameters and thresholds used throughout this Chapter on the derived parameterization (Chapter 5) have been determined experimentally.

Only recently it has become possible to perform a more systematic evaluation of individual thresholds and processing steps. A discussion on the potential for improvements can be found in Section 5.4.2.

The image processing framework developed by the author is implemented as plain C++ code using open source libraries/software packages. Further details are described by Binder *et al.* (2013a).

3.2 Previous studies

Adjustment to image type

The extraction of grains and grain boundaries has been performed on a wide range of microstructure images. In structural geology, the analysis of thin sections under cross-polarized light is well established and brought forward the development of dedicated image analysis methods (e. g., Bartozzi *et al.* , 2000; Heilbronner, 2000). From the image analysis perspective, the acquisition of birefringence patterns simplifies the extraction of individual grains. The maximum response of an adequate edge filter, e. g., the Sobel filter applied on ice samples by Gay & Weiss (1999), coincides in general with grain boundaries. The detection of the latter is more difficult for similar orientations of neighboring grains which increases in frequency with depth along deep ice cores. A toolbox to extract and parameterize grain boundary networks and the c-axis distribution has been developed by Durand *et al.* (2006b).

The analysis of images capturing only sublimation (respectively, etching) grooves and no crystallographic information call for more advanced methods. The ongoing application of manual grain boundary correction/tracing (e. g., Herwegh, 2000; Spaulding *et al.* , 2010) or individual thresholding (as applied by Horn, 2009; Weikusat *et al.* , 2009b) indicates that a universal edge detector does not exist. The *Lazy Grain Boundary* method introduced by Heilbronner (2000) follows the idea to apply more than one filter and to compile the best boundaries that can be detected by each of them. The problem with this approach is that not the filters are combined, but the segmented boundaries. The *Random Forest* approach overcomes this problem as all selected filters are compiled to pixel-wise boundary probability forming the basis for segmentation.

Skeletonization

The size of the smallest details that are to be resolved is crucial when selecting the method of image processing. If focus is laid on grain size and not on

highly resolved grain boundaries, morphological operations including skeletonization, which can be traced back to Serra & Cressie (1982), can be applied. Such an approach has been developed for sublimated ice surfaces by Arnaud *et al.* (1998). Skeletonization is usually only applied to binary images, meaning that the extracted skeleton is distinguished from other possible results based on general geometric assumptions. Therefore, serrated and energetically unfavorable grain boundaries rarely occur. The analysis of sublimation grooves suggest that this assumption represents an oversimplification even at shallow depths (Kipfstuhl *et al.* , 2006, 2009).

Wide undetermined bands around grain boundaries in c-axes orientation measurements require the application of skeletonization. If a similar approach is applied to sublimation groove images (as by Arnaud *et al.* , 1998) the surplus in information about the position/shape of grain boundaries will not be exploited.

3.3 Boundary probabilities

3.3.1 Combination of different filters

To extract different features or different appearances of one feature, the combination of different filters is required. A faint, narrow boundary can only be detected by a small filter (considering a narrow neighborhood per pixel), whereas a blurred boundary gives only response if the considered neighborhood is sufficiently large. The response of a filter applied to an image is again an image, possibly a stack (matrix) of images.

A set of linear and shift-equivariant filters, which are based on scalar, vectorial, and tensorial quantities, forms the basis for several classification tasks (Binder *et al.* , 2013a). The convolution of an image with Gaussian kernel of standard deviation σ (defining the size of the considered neighborhood) represents the first step to calculate the gradient filter (first-order derivative), the Laplace filter (second-order derivative), and the Hessian filter (matrix of second-order deriva-

tives). Diagonalization of the latter yields eigenvalues and eigenvectors, which characterize the principle directions of pure curvature. The radius of the discrete analog of the Gaussian introduced by Lindeberg (1994) is given by

$$r = \sigma \cdot (3 + 0.5 \cdot n), \text{ where } n \text{ is the order of the derivative filter.} \quad (3.1)$$

The eigenvalues and eigenvectors of the structure tensor (Förstner, 1986; Harris & Stevens, 1988) provide information on the predominant directions of the gradient. The boundary tensor, as introduced by Köthe (2003), provides a measure for boundary energy, which is independent of the symmetry of the boundary.

3.3.2 Random Forest

Concept

If the aim was to highlight boundaries in a single image, the obvious approach would be to visually compare the responses of different filters. The comparison would probably comprise mathematical operations between two images, e. g., subtraction or addition. However, at some point the human observer would start to establish a decision tree like “If the response of filter 1 lies in the range between x and y , consider filter 3...”. An implementation of this decision tree would probably reveal correctly highlighted boundaries in this image, but it would remain unclear how successful the decision tree can be applied to similar images. A frequent problem is overfitting to the data, which could be avoided if different human observers implemented a decision tree, and a pixel-wise average over the classifications revealed by all decision trees was calculated.

The Random Forest approach (Breiman, 2001) follows the same procedure, with the difference that the interaction with the user is reduced to a minimum. Application to similar segmentation problems exhibited highly accurate results (Ren & Malik, 2003). Training data has to be generated before bootstrap samples (subsets) are chosen randomly with replacement. Some training points may be

covered several times whereas others are not considered at all. The generation of decision trees from all bootstrap samples (in the present case 256) is sufficient to avoid overfitting. The automatic generation also covers an evaluation of the importance of underlying filters (features). *Mean Decrease Gini* is directly linked to the sum of decisions made on a certain filter (considering all trees in the forest) and has been utilized to derive rankings of feature importance (e. g., Calle & Urrea, 2010).

Application, set of filters

One specific Random Forest classifier (Binder *et al.* , 2013a) is applied to calculate pixel-wise boundary probabilities on the sublimation groove images both of the NEEM and the EDML ice core. The set of selected filters has remained unchanged compared to the approach described before (Binder, 2011). Iterative addition of training data improved the capability to highlight boundaries even if the sublimation behavior and the adjusted focus/illumination lead to a wide distribution of gray values along grain boundaries (bottom row in Fig. 2-5).

The calculation of filters on sublimation groove images requires an additional preprocessing step. A Laplace filter with a Gaussian kernel of radius 8 pixels is applied to highlight the center of symmetric grain boundaries as local maxima. In case of asymmetric bubble boundaries adjacent minima and maxima are induced. A morphological minimum operator with a disc of radius 5 pixels allows to compensate for artifacts as reflections or boundaries becoming lighter in the vicinity of a bubble (for illustrations see Binder *et al.* , 2013a).

The set of applied filters is formed by:

- Strength of predominant gradient direction derived from the structure tensor of the preprocessed image ($\sigma = 1.0$, $\sigma' = 0.6$)
- Strength of predominant gradient direction derived from the structure tensor of the preprocessed image ($\sigma = 1.5$, $\sigma' = 0.9$)

- Strength of the second-strongest curvature direction derived from the Hessian matrix of the preprocessed image ($\sigma = 2.0$)
- Boundary energy derived from the boundary tensor of the preprocessed image ($\sigma = 1.0$)
- Difference of two Gaussian smoothed original images ($\sigma_1 = 0.8, \sigma_2 = 6.0$): The contrast between two differently smoothed images is of particular importance to highlight the center of asymmetric bubble boundaries.

All required parameters are directly linked to the radius of applied Gaussian kernels, see Eq. 3.1, and are adapted to the structures to be extracted. The width of boundaries is typically between 3 and 8 pixels. As this range cannot be processed adequately by one setting of the structure tensor, two different widths are combined.

Thresholding

Pixels characterized by low boundary probability (200 of 256 decision trees classify them as *no boundary*) serve as seeds for the segmentation of grains (Section 3.4.1). Higher performance is achieved by gray value thresholding which is only possible on sublimation groove images of the NEEM ice core (for details see Binder, 2011). Advantage of uniform gray values in the inside of grains as well as the narrow range of gray values along grain boundaries is taken. As shown in Fig. 2-5, both aspects do not apply to the EDML data set due to the considerable depth of field of the image acquisition system.

It cannot be ruled out that single pixels representing a grain boundary exhibit gray values lighter than the threshold. Interruption of up to 5 pixels are closed by a morphological minimum operator. The rare occurrence of wider interruptions, possibly related to insufficient sublimation of the surface, implicates that the grain boundary is not extracted. In contrast, brighter segments form a distinctive feature of sub-grain boundaries, which are considered as artifact in the present context. The frequency of missing and artificial boundaries and their influence on

the derived mean grain size is quantified in Section 5.3.1, respectively, in Section 5.3.2.

3.3.3 Gradient/misorientation based

The gradient is one of the most important filters in low-level image analysis. The toolbox developed by Durand *et al.* (2006b) is based on the Sobel filter, (as suggested by Gay & Weiss, 1999) which consists of approximations of the derivative in x- and y-direction. The necessity of manual corrections for similar orientation of neighboring grains encouraged further development. The applied G50 fabric analyzer (Wilson *et al.* , 2003) allows to substitute the gradient visible in color images by misorientation values (γ), expressed by the angles between two adjacent measurements of c-axis orientation

$$\gamma(\mathbf{c}_1, \mathbf{c}_2) = \arccos |\mathbf{c}_1 \cdot \mathbf{c}_2|. \quad (3.2)$$

In case of c-axis measurements, bubble boundaries are not visible, i. e. the term *boundary* refers only to grain boundaries. Excluding low quality values (Section 2.4.2) and high misorientation values forms an efficient way to ensure that neighboring grains (even for similar orientation) are separated on a pixel level. This method has been developed by Eichler (2013) and comprises the finding that information about the position of the grain boundaries inside the exclusion zone is not accessible. Therefore, the map of boundary probabilities is binary. Regions of not excluded pixels reaching a minimum size (a threshold of 500 pixels has been applied by Eichler, 2013) serve as seeds for the segmentation of grains.

3.3.4 Error estimation

Manually generated training data on another image has been used to improve the classifier, but such validation data cannot be regarded as objective. In a similar way, mentioned thresholds have been adjusted. As boundary probabilities are intermediate results, an estimation of errors is conducted for the parameters

whose calculation is described in Chapter 5. The assignment of grains and conglomerates of grains extracted from sublimation groove images to counterparts extracted from c-axis measurements allows to systematically analyze the contribution of individual thresholds and processing steps to deviations in matched grain structures (see Section 4.3).

3.4 Segmentation of grains and grain boundaries

3.4.1 Seeded region growing

Selection of seeds

Based on gray values, low boundary probabilities or low misorientations, which typically include more than half of the pixels in an image, have been assigned to the seeds of individual areas (see previous two Sections). The region growing algorithm has been introduced by Adams & Bischof (1994). Köthe (1995) emphasized that the selection of seeds is crucial for good performance.

Similar to the threshold in size applied by Eichler (2013), small seeds are excluded for the segmentation of sublimation groove images to reduce the probability of over-segmentation, which represents a general problem of region growing algorithms. Seeded region growing does not include the generation of additional seeds. Consequently, it is verified that small seeds cannot be connected to neighboring seeds, as the closing radius is chosen smaller than the minimum width of grain boundaries of 3 pixels. Furthermore small seeds cannot form local minima in boundary probability before they are removed by a threshold of 1000 pixels. Seeds constituting local minima are exempted from the grain size threshold.

Extension of seeds, cost functions

A further difference in the segmentation of sublimation groove and fabric analyzer images is the definition of the cost function determining which pixels are preferentially aggregated to the seeds. Region growing on the basis of binary

boundary probabilities (misorientation based) represents skeletonization, which results in smooth and energetically favorable boundaries. In contrast, the position of a boundary in sublimation groove images is determined by maximizing the boundary probability along the segmented perimeters. This approach resembles watershed region growing (Vincent & Soille, 1991).

Discretization of boundaries, exclusion of truncated areas

Region growing algorithms are very appropriate in the present case as they yield areas closed up by adjacent boundaries (Binder *et al.*, 2013a). Both elements are discretized and form the basis for parameterization (Chapter 5). Discretization of grain boundaries is carried out in inter-pixel coordinates. Consequently, every integer coordinate is assigned to an area. Areas truncated by the border of the section/image are excluded from the segmentation.

Over-segmentation

The basic idea behind the present segmentation approach for sublimation groove images is to avoid losing a single boundary (possibly between large areas) whenever it is possible at the expense of over-segmentation. Iteratively, artificial boundaries are removed (Section 3.4.3). Nevertheless, occasionally sublimation grooves are not extracted. The segmentation of fabric analyzer images does not comprise further processing steps. Every discretized area (larger than 500 pixels) is treated as grain. A validation, respectively, error estimation of boundaries extracted from both image types is performed in the context of matching grains and grain conglomerates (Section 4.4).

3.4.2 Extraction of bubbles

Extraction in NEEM data set

So far, bubble and grain boundaries have not been distinguished during the processing of sublimation groove images. Gray value thresholding, applied for the generation of seeds in images of the NEEM ice core, simultaneously enables the

discrimination between the inside of grains and bubbles. As all captured bubbles exhibit sharp boundaries in this data set, high boundary probabilities are obtained both for grain and bubble boundaries (after appropriate training of the first Random Forest classifier).

A second Random Forest classifier exploiting the

- mean boundary probability derived from the first Random Forest classifier
- difference of mean gray values of adjacent areas
- sum of neighboring areas size
- mean of absolute curvature

allows to distinguish between *grain boundaries*, *bubble boundaries* and candidates for *artificial boundaries* (for details see Binder, 2011).

Extraction in EDML data set

The bubbles mapped along the EDML ice core exhibit sharp boundaries if they are cut, and blurred boundaries if they are located beneath the surface. To ensure that the perimeter of grains is not interrupted by bubbles beneath grain boundaries, both types of bubbles are extracted in a preprocessing step. A morphological maximum operator with a disc of radius 10 pixels (contrary to the minimum operator for closing gaps) allows to remove grain boundaries completely. Subsequently, the contours of bubbles are discretized based on uniformly applicable gray value thresholds in the original image (70, maximum value/brightness: 255) and in the image resulting from the maximum operator (80). In this way the sharpness of the boundaries is not considered. Light structures entirely enclosed by bubbles are removed, as they may represent snow flakes or other artificial reflections. This functionality is optional, as it is not applicable if the pore space is not separated (above the firn-ice transition).

At the position of extracted bubble boundaries the boundary probability is set

to maximum, and the interiors of bubbles are considered as seeds. Subsequent to seeded region growing, the gradient is calculated for isolated bubbles. In order to establish comparability between the inside of grains extracted from the NEEM and the EDML ice cores, bubbles without connection to the perimeter of grains and low gradient magnitude are merged with the surrounding area. However, air bubbles located along the perimeter remain, as the grain boundary above commonly cannot be reconstructed. This source of error is discussed in the context of parameterization (Section 5.3.3).

3.4.3 Error correction

Disturbances of the sublimation process

In case of disturbances of the sublimation process the response of the set of filters to single pixels may resemble that of grain boundaries. If artificially high boundary probabilities are positioned close to each other, the morphological minimum operator with a disc of radius 5 pixels (intended to close interruptions of boundaries) will connect them. It may happen that several (predominantly small) areas are segmented. Even if single pixels exhibit high boundary probabilities, the mean boundary probability along an artificial boundary is usually lower than along a grain boundary. As the Random Forest classifier on boundary level includes this criterion, boundaries classified as highly probable artifacts are removed.

Disturbances of the sublimation process caused by the drilling fluid used for drilling the EDML ice core (bottom left example in Fig. 3-1) represent an extreme case. A high number of artificial seeds and thus a drastic increase in the number of segmented areas is induced. Automatic correction would be possible, but rather time-consuming. As these artifacts are limited to a narrow band of varying width at the border of the section, the most efficient solution is manual modification of the image defining the seeds for the segmentation of grains.

Vertical scratches and tile borders

During preparation of the surface of ice core sections by a microtome vertical scratches are generated. They can be distinguished from grain boundaries by an accumulation of boundary pixels on one specific line inclined by less than 2° , a maximum in Hough space. Compared to this approach, which has successfully been applied before (Binder, 2011), the identification of vertical scratches by Hough transform is optimized by defining a running window. This takes into account that for an individual scratch artificially dividing an area it is more likely to continue in close vicinity than at the opposite end of the surface of the section.

In some cases, artifacts are hardly distinguishable from grain boundaries or may coincide with one of them as shown in the right example in Fig. 3-1. The present segmentation/correction algorithm is not capable to extract the almost invisible grain boundary and to entirely remove the vertical scratch. The sensitivity is chosen so that in some cases artifacts remain undetected and in only very rare cases grain boundaries are removed (for an evaluation see Section 5.4.2). Despite its shape and orientation, the grain boundary shown in the upper left example is not detected as artifact, as no continuation in close vicinity is found.

Boundaries matching tile borders of the EDML micrographs acquired with an xy stage are identified via the obtained stitching information (Ueltzhöffer, 2009).

Ghost boundaries

Occasionally, ghost boundaries are visible in sublimation groove images, as remnants left by a moving grain boundary (Fig. 3-2). A shadow next to the new position provides an exact marker of the boundary's original position (Riesterer, 2009). In case of segmented ghost boundaries, small areas are formed between the current and the previous position of the grain boundary. A high proportion of these areas lies below a threshold of 500 pixels in size. After designating, an area for merging one of the neighboring areas has to be selected. Previously, the

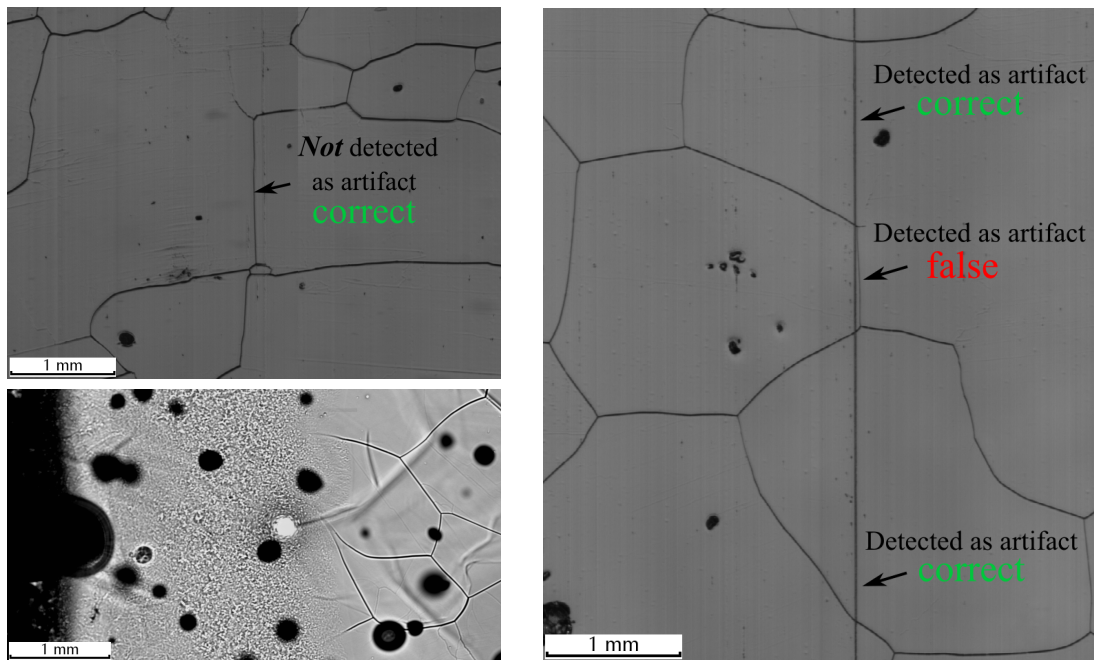


Figure 3-1: Top left: Vertical grain boundary in the center is not detected as artifact as no continuation in close vicinity is found (NEEM, 1757 m). Right: Overlapping scratch and grain boundary, grain boundary in the center is inadvertently removed (NEEM, 2099 m). Bottom left: Disturbances of sublimation process caused by drilling fluid (EDML, 494 m).

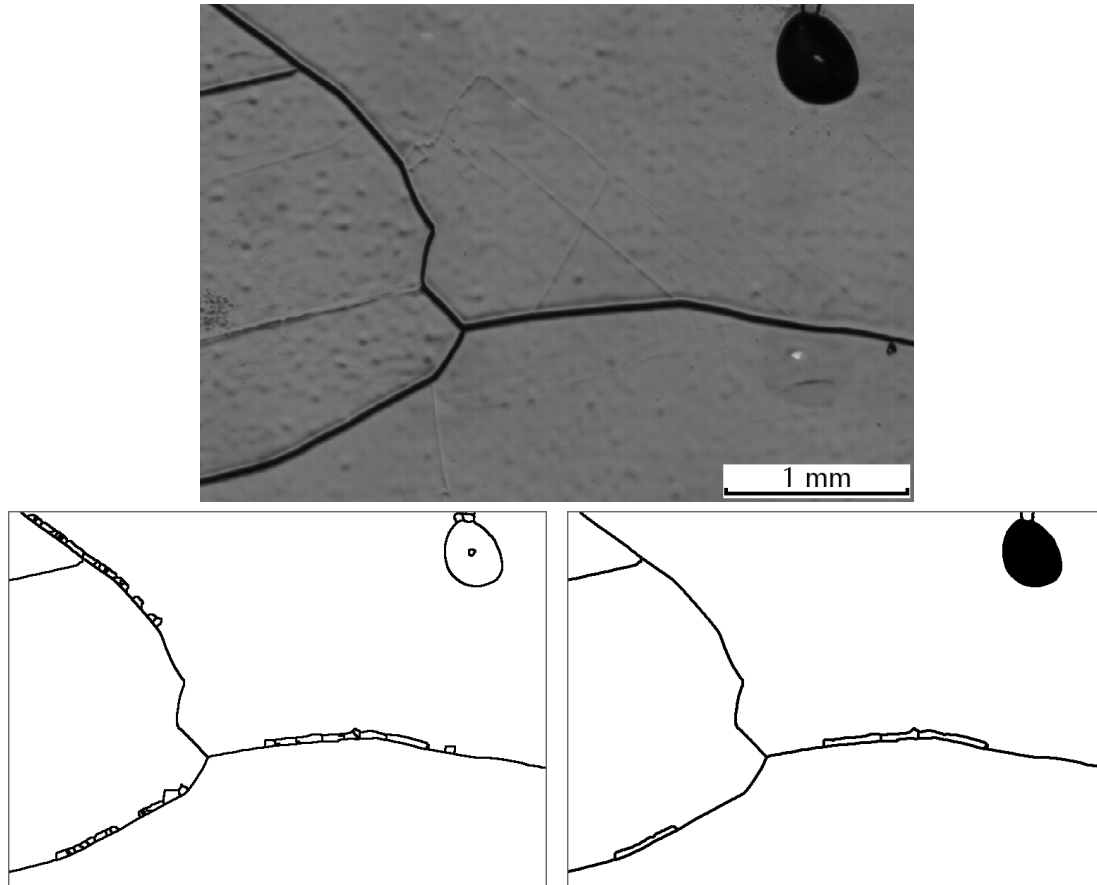


Figure 3-2: Top: Sublimation groove image from NEEM data set (≈ 600 m) exhibiting ghost boundaries. Bottom left: Result of seeded region growing, over-segmentation emerged between current and previous position of the grain boundary. Bottom right: Small areas are merged, gray value as merging criterion ensures that merging is performed along ghost boundaries. Threshold in size: 500 pixels (0.013 mm^2).

area sharing the longest boundary with the designated area has been selected. Preference to merging along the ghost boundary is given by comparing the gray values, as ghost boundaries are generally brighter than the actual grain boundary.

Chapter 4

Matching of grains and grain boundaries

4.1 Introductory remarks

The approach to automatically match grains and grain boundaries extracted from sublimation groove mapping and c-axes orientation measurements represents a novel development. Even though the matching of measurements from the same object acquired by different techniques constitutes a research area since the early 90s (e. g., Crowley & Demazeau, 1993), the approach developed and implemented by the author is adapted to consider strengths and weaknesses of both image acquisition techniques.

The matching algorithm is currently applied to six sections from the NEEM data set. They have been selected such as to cover different depth regimes (inducing difference, amongst others, in visible pore space) as well as different grain size distributions. A medium-term objective, which is a straightforward generalization of the work presented here, is to match all sections from the NEEM data set. The task is challenging because three different instruments for c-axes measurements have been applied. Up to now, only a portion of the available sections has been

analyzed by Eichler (2013); Montagnat *et al.* (2014).

The work presented in this Chapter augments this by the development of an algorithm to assign grains and grain boundaries automatically to their counterparts. The feasibility to match both image types is analyzed (Section 4.4) in order to draw conclusions regarding the potential for improvements (Section 5.4). Two error functions are defined in Section 4.3.3 which allow quantification of the agreement of grains and grain conglomerates. Another important measure is the coverage, i. e. the area of the cross-section covered by reliably matched grain structures.

If not otherwise specified, parameters and thresholds used throughout this Chapter have been determined experimentally.

4.2 Coarse matching

4.2.1 Affine transformation

Parameterization, initial guess

The objective of this Section is to describe the automatic derivation of an affine transformation rule for a given combination of a sublimation groove image and a c-axes orientation measurement (Section 2.5). The transformation to convert coordinates (x, y) to corresponding coordinates (x', y') covers rotation, shearing, scaling and displacement and is determined by 6 parameters:

$$\begin{pmatrix} x' \\ y' \end{pmatrix} = \begin{pmatrix} \lambda_{11} & \lambda_{12} \\ \lambda_{21} & \lambda_{22} \end{pmatrix} \begin{pmatrix} x \\ y \end{pmatrix} + \begin{pmatrix} x_0 \\ y_0 \end{pmatrix}. \quad (4.1)$$

The transformation matrix can be decomposed into rotation, shearing (choosing the x-axis does not limit the generality) and scaling matrices. Since the determinants of the first two matrices always equal 1, the combined determinant is given

by

$$\det \begin{pmatrix} \lambda_{11} & \lambda_{12} \\ \lambda_{21} & \lambda_{22} \end{pmatrix} = \det \begin{pmatrix} \cos \theta & \sin \theta \\ -\sin \theta & \cos \theta \end{pmatrix} \cdot \det \begin{pmatrix} 1 & k \\ 0 & 1 \end{pmatrix} \cdot \det \begin{pmatrix} s_x & 0 \\ 0 & s_y \end{pmatrix} = s_x \cdot s_y \quad (4.2)$$

with the rotation angle θ , the shear element k and the scaling factors s_x and s_y . An initial guess for Eq. 4.2 is obtained by comparing the resolutions of sublimation groove mapping (193.5 ± 1 pixel/mm, respectively, 200 ± 1 pixel/mm) and c-axes orientation measurement (50 ± 1 pixel/mm): $\lambda_{11} = s_x$ and $\lambda_{22} = s_y$. As a consequence of the initial assumption $\lambda_{12} = \lambda_{21} = 0$ and the unknown displacement (x_0, y_0) , significant deviations may occur whose upper limit is estimated by a radius of search, $r \leq \sqrt{(x_0)^2 + (y_0)^2}$. An appropriate choice for r is 15-25 mm.

Validation of grain pairs, construction of grids

In the following, the center of mass positions of all grains extracted from one image type $\{(x_c, y_c)_i\}$ are transformed. For each element, an assignment to the center of mass position among $\{(x'_c, y'_c)_j\}$ which exhibits best agreement in corresponding grain sizes (A_i and A'_j) within the radius of search is performed. The degree of agreement ($K_{i,j}$) is calculated by

$$K_{i,j} = \max \left\{ \frac{A'_j}{A_i \cdot s_x \cdot s_y}, \frac{A_i \cdot s_x \cdot s_y}{A'_j} \right\}. \quad (4.3)$$

Owing to methodical differences in image acquisition, the found matches are not necessarily correct. In contrast, the limited accuracy in the position of grain boundaries extracted from c-axes measurements leads to deviations in grain size, i. e. thresholding on $K_{i,j}$ would either be insufficient to validate matches or would exclude many correct pairs. In case of a global displacement larger than most grain cross-sections, the majority of matches may be incorrect necessitating manual correction. However, this occurs only rarely and is not discussed further.

Given that the grains with center of mass coordinates $(x_c, y_c)_i$ and $(x'_c, y'_c)_j$ are

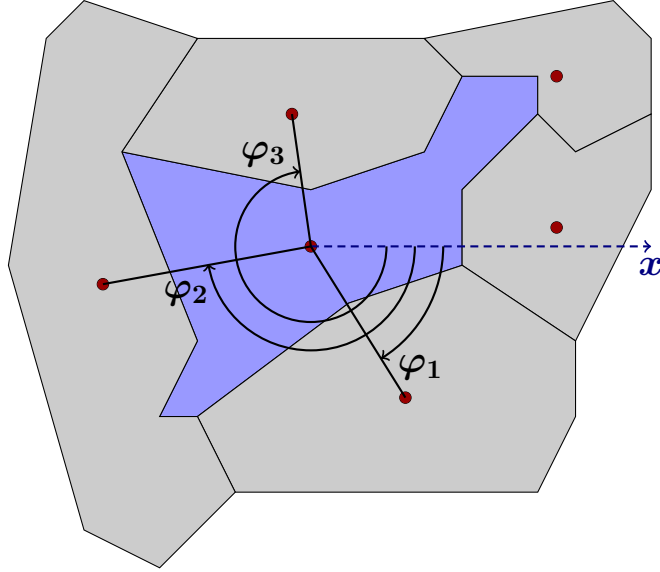


Figure 4-1: Matched grains are validated by their neighborhood. These grains are ordered by angles $(\varphi_1, \varphi_2, \varphi_3)$ enclosed by the positive x-axis and the connection of center of mass positions.

assigned to each other, the validation is carried out by considering the neighborhood of the grain in both segmentations. Neighbors are ordered by the angles enclosed by the positive x-axis and the connection of center of mass positions in clockwise direction (see Fig. 4-1).

Consistency of the number of neighbors is not required. Instead, grain pairs are considered if all neighbors in the segmentation with fewer neighbors are found. The mean degree of agreement (defined in Eq. 4.3) is calculated for all possible configurations. The different configurations emerge through rotation of one set in relation to the other and discarding different neighbors in the larger set. If the mean K of all grain pairs in the best configuration (lowest K) amounts below 1.5, the central grain pair is regarded as validated. Iteratively, a grid of validated grain pairs is constructed. However, thresholding on the grid size turned out to be more adequate. In the current implementation, grids composed of at least 9 connected validated grain pairs are taken into account to derive all 6 parameters entering Eq. 4.1.

Deviations, least square fitting

Even if all grain pairs represent correct matches, the transformation of center of mass positions according to the transformation rule presented above will exhibit slight deviations. A distinction between artifacts among the validated grain pairs and method-related deviations is not trivial. If less than half of the validated grain pairs represent artifacts, the RANSAC (random sample consensus) algorithm (Fischler & Bolles, 1981) constitutes a robust method to perform multivariate regression analysis of

$$x' = \lambda_{11} \cdot x + \lambda_{12} \cdot y + x_0 \quad \text{and} \quad y' = \lambda_{21} \cdot x + \lambda_{22} \cdot y + y_0. \quad (4.4)$$

The number of grain pairs is typically in the order of 100 which allows enumerating all possible subsets of three grain pairs instead of generating random subsets as originally proposed. For each subset the parameters are estimated. Other grain pairs which are in good agreement with this estimation (small residuals) are considered as part of the consensus set. The subset characterized by the largest consensus set is determined. By iterating over all possibilities the result is clearly defined and inaccuracies caused by random sampling are excluded. Subsequently, least squares fitting (Gauss, 1887) is performed on the basis of the best subset and its consensus set.

4.2.2 Estimation of mismatches

Grain pairs not considered when deducing the transformation rule are not necessarily artifacts. The question arises how adequately correct grain pairs (even those characterized by inconsistent neighborhoods or excluded by the RANSAC algorithm) are described. Therefore, all grain pairs obeying a bijective mapping (see Section 4.3.2) and passing a strict threshold $K < 1.1$ are taken into account to derive an estimation of mismatches. Individual mismatches are parameterized by the vector $\vec{m}_{i,j}$ pointing from the transformed coordinates of the center of mass position to the position of the counterpart. Averages and standard deviations of

Table 4.1: Mismatches are estimated utilizing the vectors connecting the center of mass position of a grain with the transformed position of the matched grain. Mean distance of the vector, $|\vec{m}_{i,j}|$, is compared to sum vector \vec{s} with corresponding standard deviation.

image pair	$ \vec{m}_{i,j} $ in mm	\vec{s} in mm
NEEM, 756 m	0.11 ± 0.10	$(-0.013, -0.011) \pm (0.121, 0.090)$
NEEM, 850 m	0.12 ± 0.20	$(-0.036, 0.015) \pm (0.215, 0.095)$
NEEM, 1026 m	0.11 ± 0.10	$(0.025, 0.019) \pm (0.095, 0.111)$
NEEM, 1757 m	0.15 ± 0.23	$(-0.019, -0.012) \pm (0.156, 0.227)$
NEEM, 1801 m	0.13 ± 0.13	$(-0.048, -0.013) \pm (0.148, 0.102)$
NEEM, 2203 m	0.08 ± 0.08	$(0.006, -0.006) \pm (0.084, 0.071)$

the length of these vectors are listed for 8 image pairs in Tab. 4.1. In addition, the mismatch vectors are combined to a sum vector

$$\vec{s} = \frac{1}{\# \text{ pairs}} \sum_{\text{pairs}} \vec{m}_{i,j} \quad \text{with} \quad \vec{m}_{i,j} = \begin{pmatrix} x'_{c,j} \\ y'_{c,j} \end{pmatrix} - \begin{pmatrix} \lambda_{11} & \lambda_{12} \\ \lambda_{21} & \lambda_{22} \end{pmatrix} \begin{pmatrix} x_{c,i} \\ y_{c,i} \end{pmatrix} - \begin{pmatrix} x_0 \\ y_0 \end{pmatrix}. \quad (4.5)$$

The distribution of $|\vec{m}_{i,j}|$ serves as basis for the 0.2 mm wide range of tolerance employed to match conglomerates of grains. The distribution of the components of \vec{s} provides information about how adequately a set of grain pairs is described by a global transformation. A well-balanced transformation is characterized by \vec{s} close to zero. Calculations of \vec{s} , for instance, solely for grain pairs found in the upper left corner of the section would allow to add \vec{s} to (x_0, y_0) so that deviations in this specific region decrease. For all considered image pairs no systematic change in \vec{s} from one region in the image to another is found.

The components of the standard deviation calculated analogously to \vec{s} are larger than components of the mean and would remain unchanged. This indicates that center of mass positions do not allow to further decrease the observed mismatches. Values for $|\vec{m}_{i,j}|$ and standard deviations in \vec{s} lie in the range of w_2 , the width of excluded pixels along grain boundaries in c-axes measurements (Section 2.4.2): $0.06 \text{ mm} \leq w_2 \leq 0.3 \text{ mm}$. This agreement confirms the assumption that the different accuracy in grain boundary position constitutes the main reason for

observed mismatches.

4.3 Grain pairs and conglomerates of grains

4.3.1 Motivation

A major reason for the development of the combined method is the possibility to automatically derive c-axis misorientations across grain boundaries extracted in high resolution by sublimation groove mapping. An essential condition is the reliable assignment of individual c-axis orientations to one side of the extracted sublimation groove. This is fulfilled for the enclosed grain boundary when two connected grains extracted from a sublimation groove image are bijectively mapped to two connected grains extracted from a fabric analyzer image. The algorithm to obtain a bijective mapping described in the following serves, even further, as basis to construct conglomerates of grains.

4.3.2 Bijective mapping and candidates for extension

Derivation and adequacy of mappings

Initially, the center of mass positions of all grains are transformed. As the positions of grain boundaries are given in inter-pixel coordinates, transformed center of mass positions cannot be located on grain boundaries. The transformed position is either located within a grain, a bubble or an incomplete grain at the border excluded from the segmentation. In the latter two cases, the closest grain (center of mass) is identified. Small grains extracted from a sublimation groove image constitute an exception. They are only identified as closest grain if $K < 5.0$. Otherwise, a considerably larger grain should exist in close vicinity. The corresponding center of mass positions are transformed back. If this procedure results in an unambiguous grain pair, size and shape may exhibit good agreement or differ significantly as shown in Fig. 4-2.

Almost exclusively correct/complete grain pairs may pass a strict threshold of

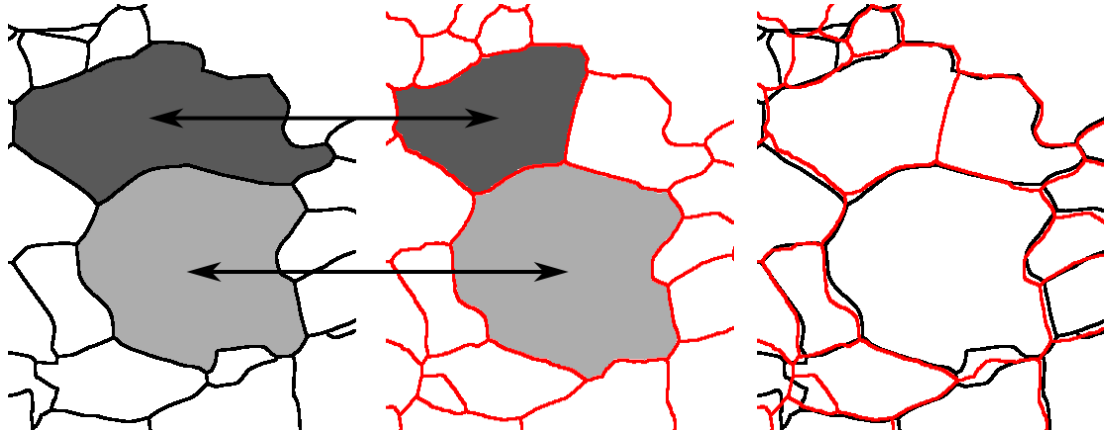


Figure 4-2: Segmentations of grains from sublimation groove images (left) and fabric analyzer image (middle) are matched by bijective mapping as indicated by arrows. Segmentations drawn upon each other (right). Image: NEEM 186610_2.

$K < 1.1$ as utilized before. But, in many cases, the mapping can be completed by adding one or many neighboring grains. The 1 : 1 assignment is considered a special case of an 1 : n assignment. This comprises the case that several grains extracted from a sublimation groove image are assigned to a single grain from a fabric analyzer image and vice versa.

In contrast, the conceivable case of a $n_1 : n_2$ assignment is not considered as it would probably include merging across undetected high-angle grain boundaries. The chosen approach is to discard grains necessitating a $n_1 : n_2$ assignment and to quantify their portion, respectively, impact (Section 4.3.3).

Evaluation of adjacent grains

The challenge is to identify correct 1 : n assignments and to differentiate them from artificial conglomerates. As in the 1 : 1 case, thresholding exclusively on K is not adequate. However, consider first the question which grains constitute candidates for an extension. Assume, the bijective mapping between grain i_1 (in one image) and grain j (in the other image) necessitates an extension of grain i_1 . All grains $i_2 \dots i_m$ ($m \geq n \geq 1$) possessing a center of mass position inside and within a range of tolerance outside the transformed perimeter of grain j should be considered. The range of tolerance is set to 0.2 mm in order to

cover the major share of mismatches (see Tab. 4.1). The problem arises that each grain with center of mass within the range of tolerance (inside and outside the transformed perimeter) may also be regarded as candidate for extension of a neighboring grain. Being part of two conglomerates would cause inconsistent results, amongst others regarding the portion of covered/uncovered grains. If an extension by grains extracted from a sublimation groove is required, the evaluated merging criteria (Section 3.4.3) can be utilized.

It is more probable that a grain i_g ($2 \leq g \leq m$) with center of mass within the range of tolerance should be merged across a grain boundary visible as faint line than across a grain boundary visible as pronounced dark line. An additional merging criterion requires that the candidate for extension shares at least 25% of its perimeter with the grain to be extended. In case of doubt, the grain i_g remains unconsidered. Grains inside the transformed perimeter and more than 0.2 mm away from it do not have to obey the merging criteria to be regarded as candidate for extension. The grain i_1 is unconditionally extended by completely enclosed grains which does not apply to bubbles which remain segmented separately.

As merging criteria are not available for grains extracted from a fabric analyzer image only (but all) grains inside the transformed perimeter are considered for extension in this case. Owing to the threshold of 500 pixels employed for the extraction of grains from fabric analyzer images (Eichler, 2013), the occurrence of center of mass positions within the range of tolerance is rare as the minimal grain size corresponds to an equivalent grain radius (Section 5.2.2) of 0.25 mm.

In principle, all possible combinations between grain i_1 and the candidates among $\{i_g\}$ could be evaluated. As they are carefully selected, complexity can be limited by evaluating only two combinations for the extension of grain i_1 (the second one is omitted for an extension in the segmented fabric analyzer image):

1. extension by all candidates inside the transformed perimeter
2. extension by all candidates inside and outside the transformed perimeter

4.3.3 Verification of conglomerates

An assignment between the set of grains $i_1 \dots i_n$ (in one image) and grain j (in the other image) is only possible if size and overall shape as well as small-scale roughness and overall orientation exhibit good agreement. The latter two aspects are quantified by the perimeter ratio and the ellipse flattening factor as described in Section 5.5. Deviations in both shape factors are calculated analogously to Eq. 4.3 and are added in quadrature forming a geometric error function.

The estimation of quasi-continuous orientations of local tangent vectors along grain boundaries is part of the parameterization described in Section 5.6. Extending the range of angles to 2π (or even further) allows to obtain a steady profile following the perimeter of a grain. As these profiles exhibit different length, re-scaling of one profile is required. As the shorter profile obtained from c-axes measurements is characterized by a much smoother profile of tangent orientations, the more serrated profile obtained from segmented sublimation grooves is downscaled utilizing a cubic spline interpolation (Bartels *et al.*, 1998) so that a similar degree of smoothness is achieved. A comparison of profiles is shown in Fig. 4-3. The starting points are chosen by selecting the pixel reached by moving upwards along the y-axis from the center of mass position. As shifts may occur, a synchronization step is performed utilizing cyclic cross-correlation. The specific characteristic of the method is that points of the first profile are shifted by 2π to preserve steadiness when crossing the border of the sliding window fixed to the second profile. To avoid a continuous increase in angles, the profile is iteratively lowered. Consequently, after a complete shift the first profile has reached its initial state. It is worth mentioning that the anisotropy in scaling given for the sublimation groove images of about 3% (Section 2.3.2) induces slight deviations in the profiles.

The correlation coefficient at the position of optimal synchronization (R) enters

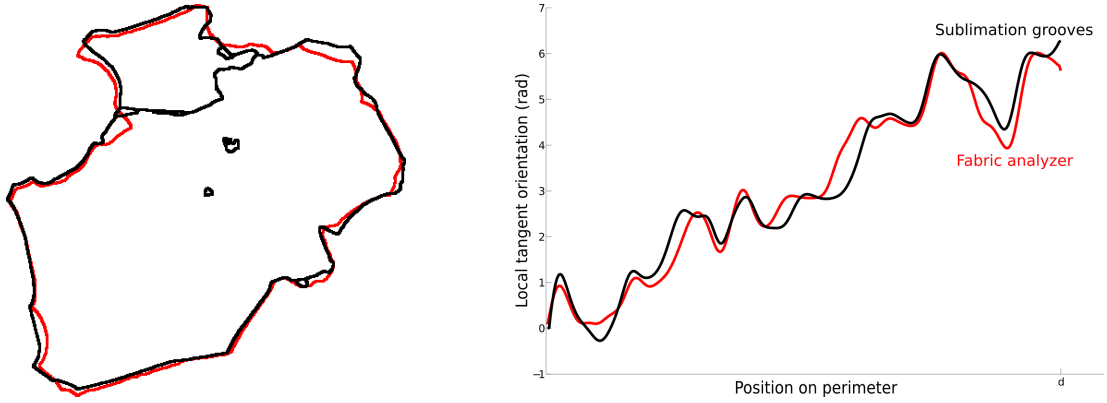


Figure 4-3: Left: Conglomerate of 7 grains segmented from sublimation grooves (black) is matched to single grain segmented in fabric analyzer measurement. Right: Comparison of profiles of local tangent orientations allows to validate assignment as correct. Starting points are “at the top” of visualization (left), parameterization in clockwise direction.

the (empirically derived) second error function

$$\text{erf}_2(K, R) = \sqrt{K^2 + \frac{1.5}{R^2}}. \quad (4.6)$$

Combined thresholding on both error functions (with critical value 1.69) enables distinguishing between correct and artificial conglomerates. The question arises what should be preferred: Either a set of conglomerates covering 99% of the cross-section (referred to as coverage) under the premise of several false assignments or a set of lower coverage that exhibits almost no false conglomerates with high probability. The latter case is considered in the following to ensure that conclusions drawn from conglomerates are not significantly affected by false matches. Corresponding coverage values are listed in Tab. 4.2 and show that at least half of the cross-section of the sample is covered by matched grains and conglomerates of grains. The observed change of coverage with depth can be explained by the change in grain size. In ice core sections exhibiting predominantly large grains a larger proportion of the grain structure can be reliably matched than in ice core sections characterized by a high number of small grains as for the fourth image pair.

Table 4.2: Quantification of the area of the cross-section covered by matched grain structures.

image pair	coverage
NEEM, 756 m	66%
NEEM, 850 m	71%
NEEM, 1026 m	76%
NEEM, 1757 m	48%
NEEM, 1801 m	58%
NEEM, 2203 m	73%

4.3.4 Error estimation

The quantification of errors induced by incorrect assignments of grains/conglomerates of grains to each other would require ground truth data (not available) or a second, independent method. The algorithm presented here is highly adapted to the underlying image acquisition techniques and the significant mismatches generated by methodical limitations. The implemented method to validate conglomerates is adjusted so that the covered region is reduced to the proportion that can be reliably assigned to their counterparts in the other image. In this way, the possibility of inadvertent removal/insertion of grain boundaries due to incorrect assignments is reduced. The obtained degree of coverage allows to estimate errors in the derived parameterization, but is not sufficient to replace mean grain size and other parameters by the corresponding value derived only from matched conglomerates. The unconsidered grains would require $n_1 : n_2$ assignments for which a discrimination between true and artificial grain boundaries is not as straightforward as in the $1 : n$ case.

4.4 Exploitation of matching for error estimation

4.4.1 Invisible/unextracted grain boundaries

It should be recalled that only the c-axis is considered. As full crystallographic orientation, in particular the orientation of a-axes, cannot be revealed, misorientations are underestimated in the following. This underestimation may be tolerable

as less than 10% of sub-grain boundaries are characterized by an a-axes misorientation significantly larger than the c-axis misorientation (Weikusat *et al.* , 2011b; Faria *et al.* , 2013b). A systematic analysis of full crystallographic orientation by methods like EBSD or X-ray Laue diffraction would take several weeks for a single ice core section. Such analyses are limited to single (sub-)grain boundaries.

Basically two cases can lead to conglomerates of several grains extracted from a fabric analyzer image mapped to a single grain extracted from a sublimation groove image. In one case, the inner grain boundary (or boundaries) represent artifacts like scratches created during sample preparation, for which no automatic correction has been developed so far (Eichler, 2013). The main reason is that a vanishing misorientation across a segmented grain boundary does not represent a sufficient criterion. The frequency of low misorientations between random grain pairs has been determined to a few percent at shallow depth (Svensson *et al.* , 2009; Durand *et al.* , 2009) and reaches values of more than 10 percent in the lower 1000 m of the NEEM ice core (Eichler, 2013). The observation that a grain boundary exhibiting less than 5° misorientation is not segmented in a sublimation groove image constitutes another, independent indicator. Misorientation is readily accessible by the twisting of mean c-axis vectors of both adjacent grains segmented in the fabric analyzer image.

In the second case, the segmentation of sublimation grooves may be incomplete despite the efforts of not losing a single boundary. Grain boundaries inside the conglomerate exhibiting more than 5° misorientation provide evidence for this case. The progressing alignment of c-axes with depth induces that missing grain boundaries are not reliably detected at greater depths. Reasons for their emergence range from insufficient sublimation of the surface in the context of image acquisition to different types of error correction, part of the extraction of grains and grain boundaries. The influence of missing grain boundaries on the derived mean grain size is discussed in Section 5.3.1.

In Tab. 4.3, the properties of missing grain boundaries are compared to validated

Table 4.3: Number of missing and validated grain boundaries. Corresponding mean length and mean linearity are compared. Total increase in grain boundary length is derived from proportion and length of missing grain boundaries.

image pair	missing	validated	length [mm]	linearity	total increase
NEEM, 756 m	20	516	1.98 / 2.16	0.88 / 0.88	3.6%
NEEM, 850 m	8	405	1.60 / 2.24	0.85 / 0.87	1.4%
NEEM, 1026 m	9	350	2.48 / 2.64	0.74 / 0.86	2.4%
NEEM, 1757 m	47	693	1.44 / 1.50	0.91 / 0.91	6.5%
NEEM, 1801 m	31	771	1.56 / 1.62	0.87 / 0.90	3.9%
NEEM, 2203 m	17	1116	1.98 / 1.80	0.88 / 0.88	1.7%

grain boundaries. Only in the case that both adjacent grains divided by a grain boundary in the segmentation of one image type are assigned to two adjoining grains (or conglomerates of grains) segmented in the other image type, the grain boundary is regarded as validated. Consequently, the influence of missing grain boundaries on the total increase in grain boundary length is over-estimated. The ratio between the distance between the starting and ending point and the actual length of grain boundary is referred to as linearity. The results show that invisible/unextracted grain boundaries are in most cases slightly shorter, but reveal similar curvature (mean curvature is inversely proportional to linearity).

4.4.2 Artifacts among extracted sublimation grooves

In the following, the case that an extracted sublimation groove is not represented by a counterpart in the segmented fabric analyzer image is considered. An analysis of the induced decrease in mean grain size can be found in Section 5.3.2. For this purpose, grain boundaries exhibiting less than 5° misorientation are removed. As misorientation alone does not represent a sufficient criterion to detect artifacts or sub-grain boundaries, the non-existence in the independent segmentation approach is interpreted as second, and therefore, a sufficient indicator.

The correction algorithm (Section 3.4.3) does not allow revealing all artificial boundaries. One reason underlying the incompleteness is to reduce the probability that “correct” grain boundaries are inadvertently removed. Sub-grain boundaries

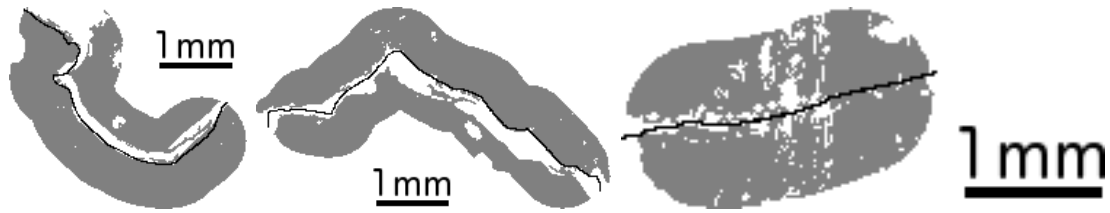


Figure 4-4: Three exemplary ranges of considered c-axes measurements (gray) around the transformed position of extracted sublimation groove (black) to obtain misorientation. A mask (Section 3.4.1) excludes inconsistent measurements (white), predominantly the case along “correct” grain boundaries.

are considered as artifacts as well. Differences in sublimation behavior, adjusted focus and illumination impeded sub-grain boundaries from being identified based on gray values in the NEEM data set.

Non-existence of grain boundaries in the segmentation of a fabric analyzer image necessitates the determination of a range of considered c-axis orientations on both sides of the potentially artificial grain boundary. The coordinates of the extracted sublimation groove are transformed into coordinates of the c-axis measurement. It should be recalled that within a range of 0.1-0.2 mm around the transformed position uncertainty exists whether c-axis measurements are assigned to the correct side of the boundary.

The mask applied to c-axis measurements in the context of segmentation of grains (Section 3.4.1, shown in Fig. 2-6) allows to exclude positions where the measurement of c-axis orientation exhibits inconsistency. As this is predominantly the case along grain boundaries, excluding these measurements already ensures that the largest part of considered c-axis measurements is assigned to the correct side (e. g., see Fig. 4-4). Incorrect assignments may occur, but their influence can be reduced if most considered positions are located outside a range of uncertainty. This is accomplished by considering all positions which are less than 0.6 mm away from the closest pixel among the transformed representation of the grain boundary. It is necessary to ensure that the distance to the closest pixel does not exceed the distance to the starting/ending position as the assignment of those positions to one side of the boundary is not clearly defined.

Table 4.4: Number of artificial and validated grain boundaries. Corresponding mean length and mean linearity are compared (artifacts / validated). Total decrease in grain boundary length is derived from proportion and length of artificial grain boundaries.

image pair	artifacts	validated	length [mm]	linearity	total decrease
NEEM, 756 m	131	784	0.71 / 1.37	0.67 / 0.88	8.0%
NEEM, 850 m	93	703	0.93 / 1.23	0.66 / 0.87	9.0%
NEEM, 1026 m	79	547	0.78 / 1.66	0.70 / 0.86	6.4%
NEEM, 1757 m	95	825	1.40 / 1.23	0.87 / 0.91	11.7%
NEEM, 1801 m	146	898	1.33 / 1.39	0.84 / 0.90	13.4%
NEEM, 2203 m	120	1320	1.32 / 1.48	0.83 / 0.90	7.5%

Without any doubt this determination of a range of considered c-axis orientation is not the “optimal” choice. Instead, a general exclusion of positions within a range of 0.1-0.2 mm around the transformed position of the grain boundary would be possible as well as a consideration of the gradient in c-axis orientation across the boundary. However, a gradient in co-latitude and azimuth angles cannot be converted into a misorientation without defining a reference length. A systematic study of misorientation as the change in c-axis orientation within a defined reference length remains a task for future research. In the present scope, the identification of artifacts is performed with the objective of estimating their influence on the main grain size in relation to other influences. The maximal distance of 0.6 mm is considered as a balanced choice between consideration of too few and too many measurement points. In the first case, mean c-axis orientation on one side of a short boundary is frequently derived from only one or two points passing the mask or is not possible as no point is left. In the second case, small-scale misorientations are potentially averaged out.

In Tab. 4.4, the properties of artificial grain boundaries are compared to validated grain boundaries. Compared to missing and validated grain boundaries, artifacts exhibit quite considerably different properties: They are in most cases shorter and more curved.

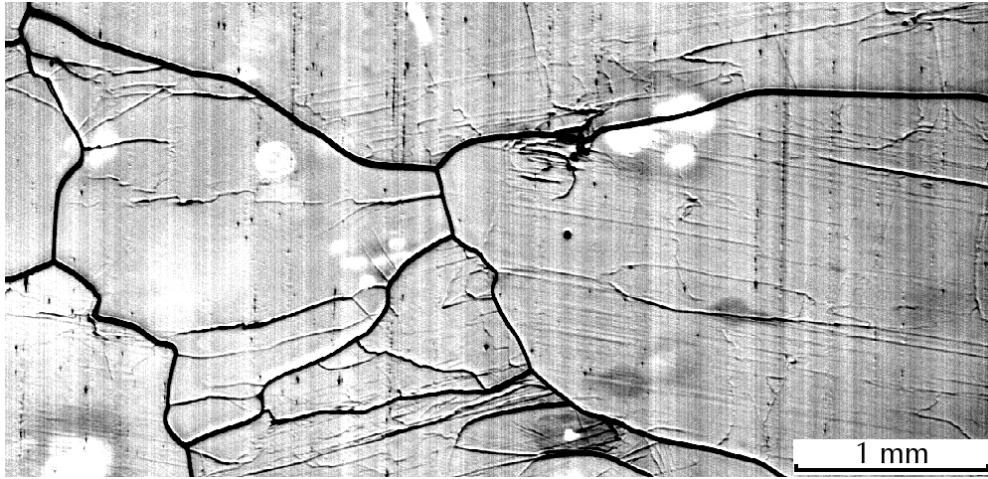


Figure 4-5: Sublimation grooves in an image from the NEEM data set (1026 m), contrast has been enhanced. Narrow, faint sublimation grooves occur at the site of sub-grain boundaries.

4.5 Fine matching

The question arises whether mismatches can be reduced by a second, fine matching step applied to a single conglomerate or limited region in the image. This would be possible if the sub-grain structures independently extracted from both image types (Chapter 6) allowed to obtain good agreement, e. g., by cross-correlation. This approach has been implemented, but fails mainly because of the difference in resolution.

The apparent width of sublimation grooves covers a range between 0.01 and 0.04 mm. Frequently, the distance between two narrow, faint sublimation grooves representing sub-grain boundaries approaches the width of the widest grain boundaries as shown in Fig. 4-5. After application of the median filter, the smallest resolvable structure from c-axes measurements is 0.06 mm wide.

C-axes measurements acquired at higher resolution possibly allow to obtain sub-grain structures of similar width as faint sublimation grooves. As related to the inclination of grain boundaries, the width of the mask utilized to exclude inconsistent measurements is not expected to decrease.

Chapter 5

Parameterization of grains and grain boundaries

5.1 Introductory remarks

The microstructural parameters described in the following have been extracted by the author from nearly all sublimation groove images of the NEEM and the EDML data set. A section is excluded if it is suspected of exhibiting a higher influence of artificial structures or if it comprises grains of similar size as the entire section. For the latter case emerging for sections from depths close to bedrock an alternative definition of mean grain size is applied.

The distribution of c-axes orientation along the NEEM ice core is not analyzed in the present context as this analysis has already been performed by Eichler (2013); Montagnat *et al.* (2014).

To the author's knowledge, the systematic analysis and quantification of errors in microstructural parameters presented in the following is unique. In this context, the matching algorithm (Chapter 4) plays an important role. All methods described in the following are part of the image processing framework published by Binder *et al.* (2013a).

5.2 Grain size

5.2.1 Previous studies

Various methods to measure grain sizes have been applied for ice core analyses so far. The limited accuracy in grain boundary position for fabric analyzer measurements also affects the resolution in grain size. Even if c-axis measurements and sublimation groove mapping were performed at the same resolution of 5 $\mu\text{m}/\text{pixel}$, especially small two-sided grains would remain indistinguishable from inconsistent information in the vicinity of grain boundaries resulting in low quality values.

Furthermore, there is a substantial difference between manual and automatic methods applying image analysis techniques. Manually, cross-sectional areas can only be approximated which has been performed by measuring width and height of selected grains (Gow, 1969) or by the linear intercept method (Gow, 1969; Thorsteinsson *et al.*, 1997), which is based on the number of intercept points between a straight line and grain outlines and assumes circular grains. Automatic methods count the number of pixels forming the acquired segmentation of a grain area (e. g., Gay & Weiss, 1999; Svensson *et al.*, 2003), but even these automatic techniques are inconsistent (Wang *et al.*, 2003). As deformation in ice sheets occurs predominantly in vertical direction, most sections for grain size studies are oriented vertically. Gow *et al.* (1997) compared (the 50 largest) grains in vertical and horizontal section and found similar trends, the variability of grain sizes seems to be higher in horizontal direction. The orientation of vertical sections with respect to the core axis is usually unknown (e. g., Svensson *et al.*, 2003). If grain width and height are not correlated (not the case for NorthGRIP) fluctuations in the mean grain size may be explained by different orientations (Svensson *et al.*, 2003).

Spaulding *et al.* (2010) compared grain sizes extracted from SEM images to grain sizes obtained by applying the methods of Gow (1969) and Gay & Weiss (1999)

(thin sections between crossed polarizers) for three firn/ice cores drilled in East Antarctica. Substantially smaller grains could be extracted from SEM images which would also apply for sublimation groove images and raises the question which fraction of grains should be considered. The advantage of considering only largest grains is that the calculated mean is almost unaffected by the resolution. However, this approach is not representative for the complete population of grain sizes (Durand *et al.*, 2006b). Kipfstuhl *et al.* (2009) found that the evolution of mean grain size in firn differs significantly between the consideration of the 100/500 largest grains and the consideration of all grains.

To conclude, it is very difficult to draw comparisons between obtained results, as measurements of grain size performed so far depend on the method to quantify grain size, the observation method and the considered fraction of grain sizes. Absolute values as well as general trends may be affected by the chosen method. Once the number of pixels for every grain cross-section entirely mapped in a section is determined, different parameters can be extracted.

5.2.2 Grain size parameters

Method, definition

Previous studies can be distinguished by measuring grain size either in one or in two dimensions. The conversion from a cross-sectional area (A) to an equivalent radius, $r = \sqrt{\frac{A}{\pi}}$, suggests spherical shape which is in most cases not given. The roundness perimeter introduced in Section 5.5 quantifies this deviation. As *grain growth* is commonly described by the increase in cross-sectional area (e. g., Woods, 1994; Thorsteinsson *et al.*, 1997; Svensson *et al.*, 2003), the term *grain size* refers to a two-dimensional measurement in the following.

A normalization of the grain-size distribution in a section, i. e. dividing all values by the mean, gains particular importance in connection with the assumption of normal grain growth (Humphreys & Hatherly, 2004). As the expected invariance of the normalized distribution only applies for a small depth range (Svensson

et al. , 2003) normalized grain sizes are not considered.

The present method is not applicable to images acquired from ice core sections close to bedrock, characterized by grains of similar size to the entire section. In the present implementation, grain cross-sections which are not entirely surrounded by visible grain boundaries are excluded. An alternative approach applicable even to ice core section close to bedrock has been proposed by Duval & Lorius (1980). By counting the number of grains within a defined cross-section area a more robust estimate of grain size is obtained. This technique is applied to a small number of sections. However, a grain size distribution is not provided.

Limiting the influence of small-grain artifacts

Disturbances of the polished ice core section (Section 2.3) lead to artifacts which are identified and removed during the extraction of grains and grain boundaries (Section 3.4.3). Additionally, small grain boundary-like structures in the images occur which cannot be identified easily. The longer a surface has sublimated, the more artifacts may occur. Additionally, small grains in the vicinity of bubbles can be created during relaxation (Section 2.2).

For an image characterized by a long sublimation time (NEEM, 146 m depth), all small-grain artifacts have been manually removed. To reduce their influence all grains are sorted by size. Starting with the largest, grains are added until a certain percentage of the area is filled. In Table 5.1, the corresponding mean grain sizes are listed for different fractions of the considered cross-section area. Obviously, the influence can be minimized, e. g., by considering only 95% of the area. In Section 5.3.2, an automatic error estimation verifies the effectiveness of the 95% threshold in the exclusion of artifacts.

The previous definitions of the lower cut-off for grain sizes included in the grain size distribution has been arbitrary, especially since the representativity of the considered grains for the complete population of grain sizes differs from one section to another. The latter problem is resolved as the representativity can be

Table 5.1: Mean grain size for different fractions of the considered cross-sectional area, differences resulting from manual correction of artifacts in image NEEM26650_1

fraction(%)	automatic [mm ²]	artifacts corrected [mm ²]
70	6.01 ± 4.03	6.09 ± 4.07
80	4.97 ± 3.82	5.05 ± 3.86
90	3.93 ± 3.59	4.02 ± 3.62
91	3.81 ± 3.56	3.91 ± 3.59
92	3.68 ± 3.53	3.79 ± 3.57
93	3.56 ± 3.50	3.66 ± 3.54
94	3.42 ± 3.47	3.53 ± 3.51
95	3.28 ± 3.43	3.40 ± 3.47
96	3.12 ± 3.39	3.25 ± 3.43
97	2.94 ± 3.34	3.08 ± 3.39
98	2.70 ± 3.27	2.88 ± 3.34
99	2.31 ± 3.15	2.59 ± 3.26
100	1.36 ± 2.65	1.78 ± 2.93

fixed by choosing a fraction of the cross-sectional area. Furthermore, Binder *et al.* (2013b) suggested varying this fraction and studying the sensitivity of the calculated mean to the actual definition of the cut-off.

5.3 Sources of error in grain size parameterization

5.3.1 Invisible/unextracted grain boundaries

The influence of not extracted sublimation grooves on grain size can be estimated based on conglomerates of grains extracted from c-axis measurements which are mapped to single grains extracted from a sublimation groove image. The method to identify not extracted sublimation grooves is described in Section 4.4.1.

A subdivision into the range between 5° and 10° is implemented as those grain boundaries have possibly been created during migration recrystallization and are less pronounced. Furthermore, this choice is in agreement with Svensson *et al.* (2009); Durand *et al.* (2009).

The decrease in mean grain size by addition of missing grain boundaries is estimated by splitting the grain enclosed by extracted sublimation grooves in the

same ratio as in the conglomerate. In this way, the total grain size remains constant which would not necessarily be the case if grain sizes derived from a sublimation groove image were replaced by grain sizes derived from a fabric analyzer image.

The cut-off in grain size is defined by the 95% fraction of the considered cross-section and is kept constant even if each splitting of a grain larger than the cut-off possibly induces a decrease. However, the considered conglomerates do not cover the entire cross-section. Assuming that the uncovered part is free of any errors is inappropriate as some errors must impede those grains from being matched. Owing to the unconsidered change in the grain size cut-off, the derived decrease in mean grain size is underestimated.

The results, listed in Tab. 5.2, show that at least 43% of grain boundaries which are not extracted as sublimation groove, but from c-axis measurements, exhibit less than 5° misorientation and probably represent artifacts. Care has to be taken to the image pair at 1757 m and even greater depths. A significant number of grain boundaries, characterized by misorientations of less than 5° , does not represent artifacts as the misorientation between random grain pairs decreases. The highest frequency of not extracted sublimation grooves exhibiting more than 10° misorientation is found at 756 m depths and amounts to 38%. This frequency seems rather high, but does not represent the actual influence on mean grain size. If all missing grain boundaries characterized by more than 5° misorientation are inserted in the segmentation of sublimation grooves, mean grain size decreases up to 11% for a fixed cut-off in grain size.

5.3.2 Artifacts among extracted sublimation grooves

Conglomerates of grains, extracted from a sublimation groove image, which are mapped to single grains, extracted from c-axis measurements, serve as basis for the consideration of artificial boundaries as described in Section 4.4.2.

The influence of artifacts (sub-grain boundaries included) on mean grain size is

Table 5.2: Estimation of the error in mean grain size induced by not extracted sublimation grooves. Grains segmented from a sublimation groove image are split if internal boundaries exhibiting more than 5° misorientation are found in the corresponding fabric analyzer measurement.

image pair	initial [mm ²]	split [mm ²]	decrease	<5°	>10°
NEEM, 756 m	11.73 ± 11.24	10.74 ± 10.77	8.4%	48%	38%
NEEM, 850 m	10.84 ± 12.51	10.34 ± 12.24	4.6%	71%	14%
NEEM, 1026 m	20.06 ± 29.18	17.82 ± 27.20	11.1%	51%	34%
NEEM, 1757 m	5.17 ± 5.18	4.81 ± 4.45	7.0%	43%	27%
NEEM, 1801 m	6.08 ± 5.48	5.85 ± 5.32	3.9%	60%	16%
NEEM, 2203 m	8.00 ± 7.66	7.11 ± 7.23	11.1%	65%	11%

estimated by removing two entries from the grain size distribution and inserting their sum if the grain boundary dividing the corresponding grains exhibits a misorientation of less than 5° . The increase in mean grain size is derived from all grains and from grains larger than the cut-off defined by the 95% fraction of the considered cross-section. The sum of two (or several) grains is only inserted to the 95% distribution if at least one component has been included before. Similar to the opposite case discussed before, a recalculation of the cut-off based on the matched grain structures is problematic as assumptions concerning errors in the uncovered part would be required. Owing to the unconsidered change in the grain size cut-off the derived increase in mean grain size is underestimated.

The comparison between the increase for consideration of the 95% fraction and the 100% fraction (values listed in Tab. 5.3) confirms that the influence of artifacts is reduced by the applied cut-off. Consequently, further parameters (grain shape and related to grain boundaries) are derived only from this fraction. The influence of artifacts remains of the order of 10%.

5.3.3 Other sources of error

Sectioning effect

The occurrence of irregular grain boundaries questions the applicability of previous stereological approaches. Simulations of normal grain growth (Anderson

Table 5.3: Estimation of the error in mean grain size induced by artifacts among extracted sublimation grooves. Boundaries not extracted from the corresponding fabric analyzer measurements and exhibiting less than 5° misorientation are removed, adjacent grains are combined. Increase in grain size derived for grains larger than cut-off (95% fraction of considered cross-section) and for all grains.

image pair	initial [mm ²]	merged [mm ²]	increase 95%	increase 100%
NEEM, 756 m	11.73 ± 11.24	12.41 ± 11.63	5.9%	24.6%
NEEM, 850 m	10.84 ± 12.51	11.49 ± 12.81	6.0%	18.0%
NEEM, 1026 m	20.06 ± 29.18	20.88 ± 29.61	4.1%	20.0%
NEEM, 1757 m	5.17 ± 5.18	5.75 ± 5.81	11.3%	16.5%
NEEM, 1801 m	6.08 ± 5.48	6.93 ± 6.72	13.9%	26.9%
NEEM, 2203 m	8.00 ± 7.66	8.57 ± 8.91	7.1%	18.8%

et al., 1989) were employed to estimate the influence of 2-dimensional sections on the mean grain size (Durand *et al.*, 2006b). The assumption that the normalized grain-size distribution is adequately described by a log-normal distribution (in addition to the regularity of grain boundaries a characteristic of normal grain growth, see Humphreys & Hatherly, 2004) only applies for the upper 300 meters (Svensson *et al.*, 2003). However, the sectioning effect influences the calculation of mean grain sizes. As long as the interplay of microdynamic processes, especially the impact of dynamic recrystallization, is not well understood, the application of estimated corrections, e. g., a factor of 1.3 (Thorsteinsson *et al.*, 1995) or 1.5 (Fisher & Koerner, 1986), would be pointless. Cross-sectional areas as obtained directly from the measurements can easily be compared to other studies. C-axis measurements are not influenced assuming a small misorientation within the thickness of the sample (Durand *et al.*, 2006b).

Anisotropic scaling

The direction-dependent deviation in scaling for the sublimation groove images acquired along the NEEM ice core has been estimated to be 3% (Section 2.3.2). Compared to the errors related to missing and artificial grain boundaries, the contribution of the unconsidered direction-dependence plays a minor role. The resolution of the horizontal direction (193.5 pixel/mm) is applied which induces an overestimation.

Visible air inclusions

Currently, no clear definition of grain size with respect to bubbles is established (Weikusat *et al.*, 2009a; Kipfstuhl *et al.*, 2009). As bubbles are not identifiable in c-axes measurements, skeletonization constitutes the only possibility. Filling up the pore space with ice does not provide a realistic representation. An improvement would be to consider bubbles intersecting with the surface plane and to ignore all visible bubbles in other planes (not intersection with the surface). This is not possible without restrictions, but in any case, consistency within a data set is crucial. A comparison requires even consistency between different data sets.

Influence of sublimation on visible bubbles

The duration of surface sublimation constitutes a critical factor for the visible size of bubbles in the NEEM data set as the size of grooves rises with time. Horn (2009) corrected the mean grain size by assuming that the total area of visible bubbles increases linearly with time. Limited analysis of the sublimation behavior of polished ice core sections at Kohnen Station, East Antarctica, (see Fig. 5-1) indicated that initially small bubbles exhibiting high curvatures grow faster than large bubbles. Repeated performance of such analysis in the future may provide information on the dependence on temperature and air humidity. The climatic conditions at Kohnen Station (low temperature, high humidity) caused sublimation to occur significantly slower than in an ice laboratory (usually -20° , low air humidity). As even for the shallowest analyzed sections of the NEEM ice core (102 m) the proportion of visible bubbles on the surface is $\approx 5\%$ (and decreases with depth), the influence of the increase in bubble area on mean grain size does not require further consideration.

Influence of depth of field on visible bubbles

Following Eq. 2.1, the depth of field for the transmission microscopy system, utilized along the EDML ice core, has been estimated to $d \gtrsim 0.3$ mm. The

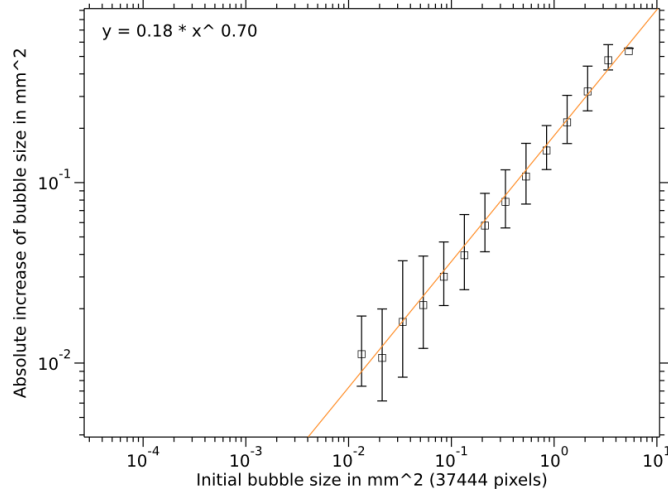


Figure 5-1: Absolute increase of bubble area after 14 hours sublimation at $\approx -40^\circ$ (Kohnen station, B40, 76 m)

question arises to which degree the extend of visible pore space is increased in comparison to images acquired along the NEEM ice core. In the latter case, the visible radius of a spherical bubble with radius r_0 at center point z_0 below/above surface is approximately given by $r_B = \sqrt{r_0^2 - z_0^2}$. The bubble is only visible for $z_0 < r_0$.

Which change is induced by the difference in depth of field? In about half of the cases, the center point of the bubble has been located above the surface so that no modification of r_B occurs. Otherwise, the bubble radius appears as

$$r'_B = \max_{z \leq d}(\sqrt{r_0^2 - (z - z_0)^2}) \quad (5.1)$$

which is split into $r'_B = r_0$ for $z_0 < d$ and $r'_B = \sqrt{r_0^2 - (d - z_0)^2}$ for $d \leq z_0 \leq d + r_0$.

In order to take into account that even the number of visible bubbles is different, an integration of the visible bubble radius in z_0 is required assuming that the distribution of center points is uniform. Integration is conducted for the range in z_0 where bubbles are visible yielding areas perpendicular to the surface. The

ratio of these areas (A and A') equals in average the ratio of visible bubble radii.

$$A = \int_{-r_0}^{r_0} \sqrt{r_0^2 - z_0^2} dz_0 = \frac{\pi r_0^2}{2} \quad (5.2)$$

$$A' = \int_{-r_0}^0 \sqrt{r_0^2 - z_0^2} dz_0 + \int_0^d r_0 dz_0 + \int_d^{d+r_0} \sqrt{r_0^2 - (d - z_0)^2} dz_0 = \frac{\pi r_0^2}{2} + dr_0 \quad (5.3)$$

The visible area of the pore space is proportional to the squared radius. The increase in this area appears when images of the NEEM and the EDML ice core are compared and is given by

$$\frac{A'^2 - A^2}{A^2} = 4 \cdot \frac{\pi dr_0^3 + d^2 r_0^2}{\pi^2 r_0^4} = 4 \cdot \frac{\pi dr_0 + d^2}{\pi^2 r_0^2}. \quad (5.4)$$

Consequently, bubbles exhibiting a radius of $r_0 = 0.20$ mm at their center point induce an increase in visible pore space by about 300%. This applies to 200 m depth where bubbles cover 3% in a sublimation groove image from the NEEM data set. A proportion of at least 12% is expected in a corresponding image from the EDML data set. If the actual proportion is higher than predicted by Eq. 5.4, the depth of field is probably larger than 0.3 mm. Good agreement is found at 200 m depth as shown in Fig. 5-2. Even if bubbles without connection to the perimeter of grains and low gradient magnitude are merged (see Section 3.4.2) with the surrounding area (marked in red), derived grain sizes from the EDML images remain more influenced by bubbles. The relative increase becomes larger with depth, whereas the influence on grain size related to the absolute increase and the frequency of air bubbles connected to grain boundaries is most significant at shallow depth.

Visible clathrate hydrates

Clathrate hydrate (Fig. 2-2) are visible in images acquired along the EDML ice core. In contrast to bubbles and due to their brightness they are extracted as grain areas. However, they cover less than 3% of the cross-section and play a minor

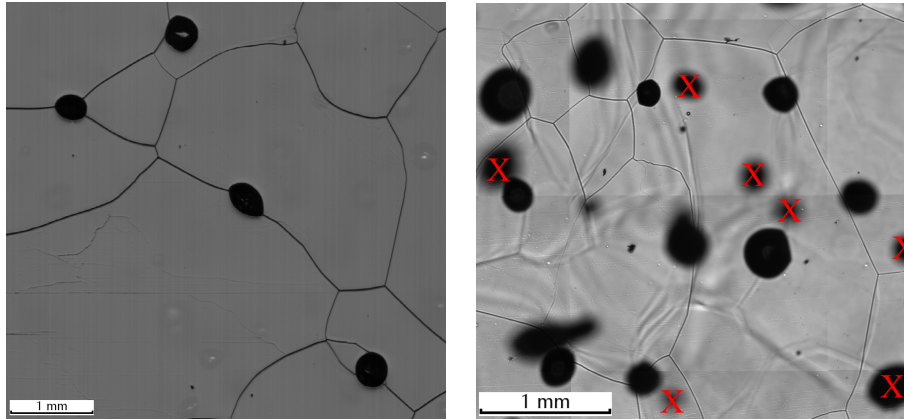


Figure 5-2: Sublimation groove images of NEEM data set (left) and EDML data set (right) at approximately 200 m depth exhibit different number of visible bubbles. All bubbles are extracted, bubbles marked in red are automatically removed. Bubbles exhibiting blurred edges connected to grain boundaries remain.

role compared to the errors related to missing and artificial grain boundaries. Clathrate hydrates cut by the surface resemble cut bubbles.

5.4 Potential for improvements

5.4.1 Image acquisition/combined method

The finding that the mean grain size decreases up to 11% if potentially missing grain boundaries are inserted necessitates a careful examination of underlying causes.

As discussed in Section 2.3.3, the differences in the sublimation behavior and adjusted focus predominantly affect the feasibility to discriminate between grain and sub-grain boundaries based on gray values. This means that under unfavorable conditions some grain boundaries appear as narrow, faint sublimation grooves. Differences in the sublimation behavior can be reduced by the construction of a small chamber in which grooves evolve under the influence of precisely controlled temperature, humidity and air flow. Such a chamber could be utilized even at drill sites where high variability in climatic conditions exists (see Section 2.3.1). If sublimation inside the chamber proceeds significantly faster than outside, the

influence of the time period between polishing and mapping of the surface is reduced. Inconsistencies in the adjusted focus can be ruled out if ice core sections are cut to similar height.

Furthermore, potential for improvements exists regarding the coverage, the area of the cross-section covered by reliably matched grain structures (Section 4.3.3). If sublimation grooves were mapped on the surface of the thin section, deviations induced by reversing and thinning (see Fig. 2-1) could be prevented.

5.4.2 Extraction of grains and grain boundaries

While the data set of acquired measurements is fixed (unless measurements are repeated), the image processing framework can be changed at any time. Only recently, it has become possible to analyze the contribution of individual thresholds and processing steps to the feasibility to extract consistent grain structures from sublimation grooves and *c*-axes measurements.

Various factors can prevent a grain boundary from being segmented. The manual detection shows that few single grain boundaries are filtered out, for instance, based on their mean gray values. This means that a modification with the objective to extract these few grain boundaries correctly might enhance the overall quality of the algorithm. The reliability of an approach aiming at reducing the frequency of artifacts or to recover hardly visible grain boundaries can now be quantified. Exemplarily the reliability of the algorithm to identify scratches (Section 3.4.3) is analyzed. As shown in Fig. 3-1, the problem is to avoid the inadvertent removal of grain boundaries and to identify as many artifacts as possible.

In Tab. 5.4, the influence of missing and artificial grain boundaries (GBs) on the derived mean grains is compared between extraction without and extraction with the correction algorithm applied. As expected, the influence of artificial grain boundaries can be reduced (or kept similar) by application of the correction. As particularly apparent for the fourth image pair, the reduction of artifacts is occasionally obtained at the expense of an enhanced influence of missing grain

Table 5.4: Quantification of the reliability of the algorithm to identify scratches. The influence of missing and artificial grain boundaries is analyzed within matched structures. The coverage (Section 4.3.3) exhibit similar values in both cases.

image pair	without correction		correction applied	
	missing GBs	artificial GBs	missing GBs	artificial GBs
NEEM, 756 m	6.9%	7.5%	8.4%	5.9%
NEEM, 850 m	5.0%	5.6%	4.6%	6.0%
NEEM, 1026 m	10.9%	4.7%	11.1%	4.1%
NEEM, 1757 m	4.7%	18.2%	7.0%	11.3%
NEEM, 1801 m	4.0%	16.3%	3.9%	13.9%
NEEM, 2203 m	11.1%	7.1%	11.1%	7.1%

boundaries. This increase represents inadvertently removed grain boundaries. Nevertheless, the overall uncertainty, the sum of both influences, is reduced.

Similar to the critical aspects regarding image acquisition, potential for improvements exists regarding the image processing framework. To achieve consistency, the specific setting described in Chapter 3 has been applied to the majority of images. Images affected to an extreme extent, for instance, by condensation on the surface are currently excluded from depth profiles. Utilizing the evaluation of errors described here allows to adapt processing steps or to apply correction algorithms so that a similar influence of artifacts on the mean grain size (and other parameters) is obtained.

5.5 Grain shape

5.5.1 Previous studies

Even though previous studies focused on grain size partially utilized manual methods, parameterizations of grain shape have been applied during the last two decades (Durand *et al.*, 2006b). A comparison between the mean vertical and horizontal intercept lengths (Thorsteinsson *et al.*, 1997; Gay & Weiss, 1999) represents a first approach to quantify the deviation from a circular cross-section of a grain without a preferred elongation direction. The aspect ratio of horizontally oriented bounding boxes completely enclosing each grain (Svensson *et al.*,

2003) provides a similar estimation. In contrast to both methods (which do not allow to distinguish a circle from a square), the predominant elongation direction can be determined by an inertia tensor as calculated for each grain by Azuma *et al.* (2000); Wilen *et al.* (2003). The degree of elongation is represented by eigenvalues.

The limited accuracy in grain boundary position for fabric analyzer measurements as well as the lack of image analysis methods impeded the extraction and thus the parameterization of the perimeter of grains. Polygon courses connecting neighboring triple junctions (connection of three grain boundaries) form the basis for the descriptor proposed by Durand *et al.* (2004). The roundness parameter applied by Svensson *et al.* (2003) captures the roughness of the perimeter compared to a circular cross-section of the same size. Deviations from the convex hull of every grain are quantified by the perimeter ratio (Weikusat *et al.* , 2009b).

5.5.2 Grain shape factors

The extraction of individual grain boundaries (Section 3.4), sections of the grain perimeter terminated by two triple junctions, paves the way for arbitrary descriptors. In order to facilitate a comparison to previous studies, the predominant elongation direction is determined by fitting an ellipse to the perimeter. This method, well established in structural geology (Heilbronner & Barrett, 2013), is implemented following Pilu *et al.* (1996); Fitzgibbon *et al.* (1996) and reveals the ratio between long and short axis of the ellipse as well. The bounding box proposed by Svensson *et al.* (2003) is constructed both along the horizontal and the predominant elongation direction. Aspect ratios are derived for both orientations. The perimeter ratio is calculated utilizing the Jarvis March algorithm to compute the convex hull (Jarvis, 1973). Grain shape factors are defined as follows (see also Fig. 5-3):

- Roundness factor: $4 \cdot \pi \cdot \frac{\text{grain size}}{\text{perimeter}^2}$,
highest value: 1 (circular, i. e. perfectly round)

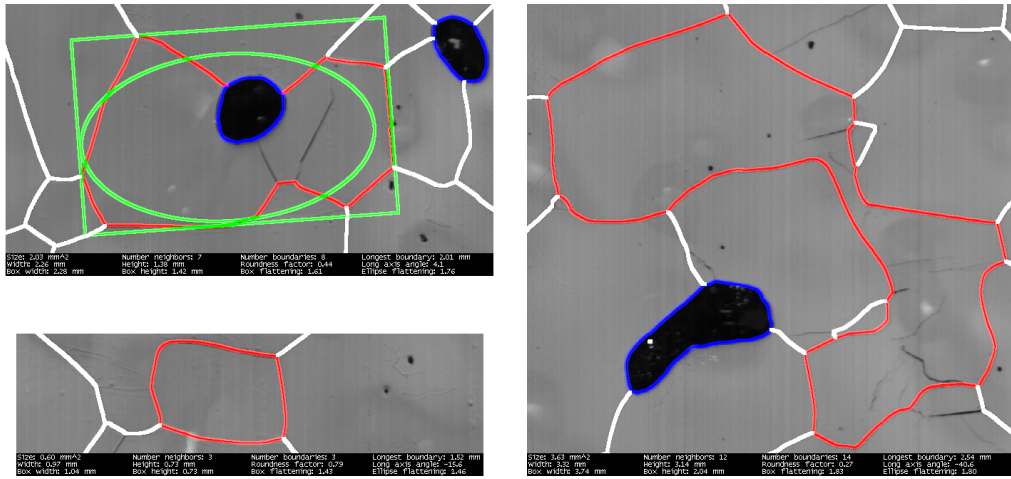


Figure 5-3: Parameterization of grain shape by ellipse and bounding box (top left). Grain with high roundness factor 0.79/perimeter ratio 0.96 (bottom left), grain with low roundness factor 0.27/perimeter ratio 0.75 (right).

- Vertical flattening: $\frac{\text{horizontal width}}{\text{vertical height}}$,
if width < height: flattening factor below 1,
if width > height: flattening factor above 1
- Ellipse flattening: $\frac{\text{ellipse long axis}}{\text{ellipse short axis}}$,
lowest value: 1 (circular, i. e. no direction of maximum elongation)
- Box flattening (elongated along ellipse long axis): $\frac{\text{box long side}}{\text{box short side}}$,
lowest value: 1
- Perimeter ratio: $\frac{\text{convex perimeter}}{\text{real perimeter}}$, highest value: 1 (perfect polygon)

The angles quantifying the direction of predominant elongation are defined as follows:

- Horizontal elongation: $\phi = 0^\circ$
- Inclination in counterclockwise direction: $0^\circ < \phi < 90^\circ$
- Inclination in clockwise direction: $-90^\circ < \phi < 0^\circ$

5.5.3 Error estimation

In case of grains of only a few pixels size, which are excluded by the minimal grain size threshold of 500 pixels (Section 3.4.1), the construction of the convex hull or fitting of the ellipse may fail. Manually drawn circles and polygon courses are utilized to validate the extreme values. This is achieved if the length of grain boundaries is calculated taking into account that the discretization contains steps of different length (Section 5.6).

Air bubbles located along the perimeter of grains constitute a problem, in particular for sublimation groove images of the upper hundreds meters of the EDML ice core (Section 5.3.3). To estimate the resulting error the grain perimeter is discretized in two different ways. On the one hand, by following the bubble boundaries and, on the other hand, by following straight-line connections equivalent to the segments of the convex hull intersecting the bubbles. The deviation in perimeter amounts for the EDML data set to 15% at 100 m depth, to 6% at 500 m depth and to 1% at 1200 m depth. For the NEEM data set, the maximum deviation is determined to be 2% at 100 m depth. As the perimeter enters the calculation of the roundness factor and the perimeter ratio the deviations propagate. As the two different discretization of the grain perimeter constitute lower and upper estimates, the same applies to derived parameters.

The error in grain shape factors induced by missing and artificial grain boundaries can be estimated on the basis of the automatically derived difference in grain boundary properties (Section 4.4). Disregarding the cut-off in grain size, the removal of every artifact among the extracted grain boundaries induces that one grain less is considered. The maximal influence of irregular artificial grain boundaries on the mean grain perimeter ratio is given by the case where they belong to small grains (slightly larger than the cut-off) and the reduced perimeter ratio of those grains is controlled by the reduction in linearity. In general, a significant deviation of a grain perimeter from the corresponding convex hull is associated with a significant deviation of the linearity of grain boundaries. As

the opposite case is not valid the estimated error is over-estimated.

Derived from Tab. 4.3, both the maximal proportion of artifacts among extracted grain boundaries (14%) and the maximal difference in linearity (24%) is found for the first image pair. If these artifacts are removed that maximal decrease in mean perimeter ratio can be estimated by their product amounting $\approx 3\%$. As only depth profiles of mean perimeter ratio are discussed in this thesis, errors for all other shape factors are not estimated here. As missing grain boundaries do not exhibit significantly different shape than validated grain boundaries, the corresponding error is small compared to the error related to artificial grain boundaries. It should be recalled that only grains larger than the cut-off defined by the 95% fraction of the considered cross-section are considered.

5.6 Grain boundary length and shape

5.6.1 Previous studies

The focus of several microstructure analyses of other minerals on the Earth's surface than ice (e. g., quartz) has been laid on the shape and density of (sub-)grain boundaries (Kruhl, 1996; Wheeler *et al.*, 2003; Kuntcheva *et al.*, 2006). Due to the shortcomings of c-axes measurements at grain boundary positions in ice, grain size is more readily accessible than the inverse property, grain boundary density. However, Heilbronner & Barrett (2013) emphasize that “as soon as grains are anisometric and/or convex-concave, grain size and inverse grain boundary density need not be the same anymore”. Assuming exclusively convex grain shape in firn and ice is not justified (Kipfstuhl *et al.*, 2009; Weikusat *et al.*, 2009b). The cross-section of a space-filling convex structure would be composed of straight grain boundaries which is obviously not the case. Consequently, the slope angle derived from the straight connection of the junctions constituting the starting and ending point of a grain boundary (applied by Eichler, 2013) is not adequate for a high proportion of grain boundaries extracted from sublimation groove images. This might not necessarily apply to grain boundaries extracted

from fabric analyzer images.

5.6.2 Implemented parameters

The roundness factor and perimeter ratio allow to quantify this deviation on the grain level, whereas estimations of the curvature of grain boundary constitute the counterpart on the boundary level. In case of serrated grain boundaries, the length of grain boundaries is not equivalent to the equivalent grain radius. Furthermore, the integration of each grain in a grain boundary network determines how the perimeter of the grain is divided into grain boundaries. A large grain entirely surrounded by small grains and a small grain located in a band of small grains correspond two similar averages in grain boundary length. For this reason, the evaluation of grain boundary lengths is encouraged by Binder *et al.* (2013a).

Owing to the discreteness of segmentation, the length of grain boundaries is calculated by accumulation of individual steps. To simplify, assign the length 1 to a step along an axis of the image. Depending on the applied method, the representation of the stair-stepped appearance of a diagonal line contains either less or more pixels than the representation of a corresponding line parallel to an axis of the image. If less, each step corresponds to $\sqrt{2}$, whereas in the second case two consecutive steps (horizontal/vertical) have to be combined to one step of length $\sqrt{2}$.

The components of local tangent vectors along a grain boundary are estimated utilizing Richardson's differentiation scheme (Richardson, 1911). Additional smoothing steps and corrections for jumps in the tangent orientation angle (proposed by Binder, 2011) allow to derive pixel-wise curvature values by the change of orientation from one to the next pixel. It is worth mentioning that quasi-continuous orientations along grain boundaries necessitates to cover a range of 2π , in contrast to the established definition of *orientation* limiting the angle to a range of π (See Fig. 5-4).

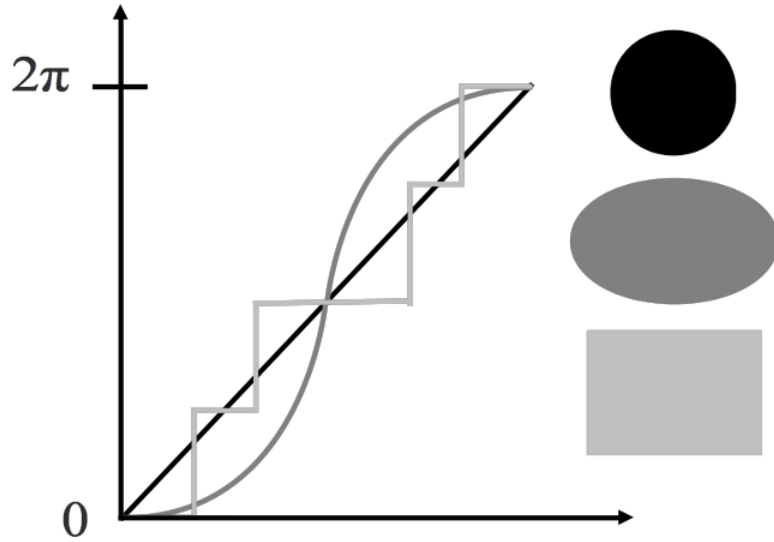


Figure 5-4: Illustration of quasi-continuous orientations along the perimeter of a circle, an ellipse and a rectangle. Note: values cover a range of 2π .

5.6.3 Error estimation

Even though the information content of grain size and grain boundary length is not equivalent, the sources of error are identical. The influence of artifacts is reduced by limiting the analysis to grain boundaries which are shared by two grains larger than the cut-off defined by the 95% fraction of the considered cross-section. In the worst case where all artificial grain boundaries are shared by grains larger than the cut-off, an upper estimate can be estimated from the increase in total grain boundary length and the increase in the number of considered grains. The highest error in grain boundary length amounts $\approx 8\%$ for the first image pair (Tab. 4.3).

The influence of artificial grain boundaries on mean grain boundary curvature can be estimated by the decrease in mean linearity which is inversely proportional to curvature. Derived from Tab. 4.3, the mean curvature of artificial grain boundaries is 1.3 times higher than the mean curvature of validated grain boundaries for the first two image pairs. By consideration of the proportion of total grain boundary length an upper estimate of $\approx 5\%$ can be calculated.

5.7 Orientation of c-axes

5.7.1 Previous studies

The orientation of c-axes is defined by the co-latitude, $\theta \in [0, \pi/2]$, and azimuth, $\phi \in [0, 2\pi]$, angles with respect to the z-axis perpendicular to the plane of the thin section. Most studies of the orientation of c-axes along ice cores utilize a horizontal reference frame (Durand *et al.*, 2006b), i. e. orientation is measured with respect to the vertical core axis.

The spherical unit vector $\mathbf{c}(x, y)$ representing the orientation of c-axis acquired for position (x, y) on the surface of the thin section is transformed into cartesian coordinates and rotated by 90° about the x-axis according to:

$$\mathbf{c}(x, y) = R_x(90^\circ) \begin{pmatrix} \cos \phi(x, y) \sin \theta(x, y) \\ \sin \phi(x, y) \sin \theta(x, y) \\ \cos \theta(x, y) \end{pmatrix} = \begin{pmatrix} \cos \phi(x, y) \sin \theta(x, y) \\ -\cos \theta(x, y) \\ \sin \phi(x, y) \sin \theta(x, y) \end{pmatrix}. \quad (5.5)$$

As the direction of the unit vector is undefined \mathbf{c} and $-\mathbf{c}$ represent the same orientation of the c-axis. However, for the calculation of misorientation between two orientations, see Eq. 3.2, as well as for deriving mean orientations for grains, the choice of rotating by 90° or by -90° is relevant. The dot product between two unit vectors is a priori not restricted to positive values. For the calculation of mean orientations per grain, denoted by \mathbf{c}_i , the direction is chosen so that the dot product between the first and the actual orientation is positive.

Odd-order orientation tensors are characterized by the same inherent problem and depend on the chosen reference frame (Durand *et al.*, 2006b). Following the suggestion by Woodcock (1977), a second-order orientation tensor, $\mathbf{A}^{(2)}$, has often been applied to parameterize the distribution of mean orientations of N grains

$$\mathbf{A}^{(2)} = \sum_{i=1}^N f_i \mathbf{c}_i \otimes \mathbf{c}_i, \quad (5.6)$$

where the cross-sectional grain areas should be used as statistical weight, f_i , as shown by Gagliardini *et al.* (2004). The eigenvalues of $\mathbf{A}^{(2)}$ constitute the basis for further analysis as performed along the NEEM ice core by Eichler (2013). This analysis is not directly linked to the present objectives. Instead, focus is laid on pixel- and grain-wise measurements of c-axis orientation which can be linked to parameterizations obtained from sublimation groove images. Durand *et al.* (2006b) attempted to quantify the misorientation within a grain, but the error in pixel-wise measurement significantly impeded this approach.

5.7.2 Implemented parameters

The mean orientation of c-axes per grain plays an important role as the knowledge of mean orientation of two neighboring grains allows to assign the corresponding misorientation value to the separating grain boundary. A low misorientation value between adjacent grains does not necessarily imply that the grain boundary can be classified as sub-grain boundaries as in the lower part of an ice sheet even the misorientation between random grain pairs exhibit a high frequency of low misorientations (Alley *et al.*, 1995; Wheeler *et al.*, 2001; Durand *et al.*, 2006b; Eichler, 2013). Grains extracted from sublimation groove images are matched to the grain boundary structure derived from c-axes orientations which necessitates the calculation of mean orientation in partitions of the grain (see Section 4.4.2).

Pixels characterized by low quality (Section 2.4.2) or high misorientation (with respect to surrounding pixels) are excluded from the mean. The misorientation threshold chosen by Eichler (2013), 1° , differs from the threshold applied by Durand *et al.* (2006b), 10° . On the one hand, the previous version of the fabric analyzer does not provide automatic identification of inconsistent crystallographic information by means of quality values. On the other hand, utilizing 1° as threshold indicates that (after application of the median filter) the noise level for the

present fabric analyzer is significantly lower.

5.7.3 Error estimation

The angle resolution and influence of noise is discussed in Section 2.4.2. In the present, c-axes measurements constitute exclusively a tool for the validation of extracted sublimation grooves. Consequently, a systematic analysis of the error of mean c-axis orientation within defined regions remains a task for future research. Such an analysis requires the presence of calibration samples with prepared orientations (as conducted on pixel level by Eichler, 2013) or concurrent measurements on ice core section utilizing EBSD or X-ray Laue diffraction (as conducted on pixel level by Weikusat *et al.*, 2011b).

Chapter 6

Extraction of sub-grain structures

6.1 Introductory remarks

Up to now, the extraction of sub-grain structures from sublimation groove images has been conducted manually (Weikusat *et al.* , 2009b). However, difficulties to discriminate between grain and sub-grain boundaries based on gray values are not relevant in this context as the majority of grain boundaries is already extracted by the approach described in Chapter 3. Sub-grain boundaries among them can be identified based on assigned misorientations for the NEEM data set, respectively, based on gray values for the EDML data set.

The calculation of boundary probabilities using a combination of different filters (Section 3.3.1) can be adapted so that the sensitivity for narrow, faint sublimation grooves representing sub-grain boundaries is enhanced. The arising problem that sub-grain boundaries entirely isolated or unilaterally connected to grain boundaries are not segmented by region growing can be resolved by applying a segmentation approach developed in the field of particle streak velocimetry (Voss *et al.* , 2012). All methods described in the following have been incorporated into the image processing framework (Binder *et al.* , 2013a). If not otherwise specified, the influence of parameters and thresholds used throughout this Chapter on the

reliability of extraction has been determined experimentally.

Owing to unmanageable noise in previous attempts to measure the orientation of c-axes on sub-grain level (Durand *et al.* , 2006b), the current approach pursued by the author to extract sub-grain structures from c-axis measurements is at an early stage of development. Therefore, only a brief impression can be provided here.

6.2 Sublimation grooves

6.2.1 Scientific relevance

Slip systems are glide planes and directions of dislocations, which can move in certain crystallographic planes only. They can be determined by analysis of the rotation axis of sub-grain misorientations (Trepied *et al.* , 1980) or by analysis of the trace of sub-grain boundaries (emerging from an accumulation of dislocations) in one direction. Sublimation grooves on the surface of ice core sections allows the determination of these traces. Slip systems are of particular significance in ice as dislocation glide on the basal plane is energetically favored by a factor 60 (Duval *et al.* , 1983). The density of sub-grain structures is relevant to study recrystallization mechanisms (Wheeler *et al.* , 2003; Drury & Urai, 1990).

6.2.2 Extraction

Pixel-wise sub-grain boundary probabilities

Sublimation groove mapping plays an important role as examination method because of its sensitivity to different sub-grain boundary types. A high fraction of sub-grain boundaries is only accessible by means of the visible sublimation groove as the corresponding c-axis misorientation is less than 0.5° (Weikusat *et al.* , 2011b). It has been observed that the sublimation behavior depends on the surface-boundary angle and thus on sample-cutting orientation (Weikusat *et al.* , 2009a). The progressive orientation of c-axes towards the vertical direction in-

duces that with increasing depth more grains are “nicely” oriented. Consequently, the frequency of sub-grain boundaries in shallow depth may be underestimated.

Bischoff (2011) adjusted the combination of filters (Section 3.3.2) in order to enhance the response of narrow, faint sublimation grooves by combining:

- Strength of the strongest curvature direction derived from the Hessian matrix of original image ($\sigma = 1.0$)
- Strength of the second-strongest curvature direction derived from the Hessian matrix of the preprocessed image ($\sigma = 1.0$)
- Difference of two Gaussian smoothed original images ($\sigma_1 = 0.8, \sigma_2 = 6.0$)

A substantial difference between the set optimized for grain boundaries (Section 3.3.2) and the present set lies in the different width of the Gaussian kernel underlying the filter associated with the Hessian matrix. The decrease from $\sigma = 2.0$ to 1.0 induces that the radius of the pixel-wise considered neighborhood is reduced from 8 to 4 pixels following Eq. 3.1. This is in good agreement with the different widths of sublimation grooves as shown in Fig. 4-5. The strongest curvature direction is derived from the Hessian matrix of the original image as the standard preprocessing step utilizes a Gaussian kernel of radius 8 pixels potentially causing a weakening of the response. A typical sublimation groove at the site of a sub-grain boundary provides response to the set of filters in the form of strong curvature along one direction (first filter) and vanishing curvature perpendicular to the strongest curvature direction (second filter). Furthermore, high difference between two differently smoothed images (third filter) is obtained as the structure fades if convolved with a Gaussian kernel of $\sigma = 6.0$.

Pixel-wise sub-grain boundary probabilities are calculated by a Random Forest classifier in three dimensional feature (filter) space. As the visual characteristics of sub-grain boundaries are very similar in sublimation groove images both of the NEEM and the EDML ice core, applicability to both data sets is given. As

demonstrated by Bischoff (2011), the map of sub-grain boundary probabilities has to be convolved with a Gaussian kernel before segmentation is feasible. A choice of $\sigma = 1.5$ reflects a compromise between preservation of fine structures and smoothing of boundaries so that subsequently derived local orientations are less susceptible to single outliers in boundary probability.

Construction of lines

The particle streak velocimetry principle deals with the recording of moving tracer particles in a fluid as streaks utilizing relatively long integration times. The reference to sublimation grooves is given by the assumption that a tracer particle, respectively, a sub-grain boundary is located at the center of the visible structure and the cross-section perpendicular to the orientation of the structure exhibits a Gaussian profile. While gray values serve as basis in the original approach developed by Voss *et al.* (2012), smoothed boundary probabilities are exploited here. Information on the predominant direction of the gradient and the boundary energy is obtained from the boundary tensor introduced by Köthe (2003) and applied as filter in Section 3.3.2. By adjusting the scale of the boundary tensor to $\sigma = 3.0$, which is larger than previously chosen to detect grain boundaries, derived orientations are sufficiently smooth. It is worth mentioning, that in contrast to grain boundaries where local orientation is calculated subsequent to the extraction, it is calculated here to facilitate segmentation.

A sensitivity level defined by a threshold in boundary energy is stepwise lowered. For every pixel passing this threshold a Gaussian bell-curve is fit to 6 pixels oriented along the predominant direction of the gradient of the potential sub-grain boundary. The central component in the related work (Voss *et al.* , 2012) is given by the nonlinear Levenberg-Marquard algorithm to estimate offset, amplitude and width of the bell-curve. It allows to combine single pixels to a straight or continuously bent line. Lines of at least 30 pixels length are initially accepted.

Identification of artifacts

An analysis of sub-grain boundary density based on structures extracted in this way is strongly impacted by the extraction of artificial structures. In contrast, sublimation grooves exhibiting sharp bending or intersecting with other grooves are only partially extracted. The suggestion by Voss *et al.* (2012) to utilize a heterogeneous Mahalanobis distance measure allows to combine separated sub-grain boundaries. However, the decision whether two sub-grain boundaries should be connected or not if geometrically possible without knowledge of misorientations is problematic as EBSD studies in deformed calcite suggest Valcke *et al.* (2006).

Artifacts among extracted sub-grain boundaries related to vertical scratches generated during preparation of the sample are detected by application of Hough transform utilizing a running window as described in Section 3.4.3. The extraction of grain boundaries as sub-grain boundaries can be excluded by applying an appropriate mask. However, it should be avoided that any artifact initially segmented during the extraction of grains and subsequently removed (such as a ghost boundary or related to disturbances of the sublimation process) is extracted as sub-grain boundary. In order to achieve this, a sub-grain boundary is classified as artifact if more than 50% of assigned pixels are less than 5 pixels away from a previously removed artifact.

6.2.3 Applicability

Reconstruction of undetected grain boundaries

As shown in Section 4.4.1, some grain boundaries exhibiting more than 5° misorientation are not automatically extracted from sublimation groove images. Currently, only interactive manipulations are possible to correct this type of error. A reconstruction of missing grain boundaries based on their segmentation from c-axis measurements would be associated with a significant loss of accuracy. In contrast, a reconstruction of grain boundaries by combining extracted sub-grain structures constitutes a method to reduce errors in the grain boundary network.

Determination of slip systems

The trace of sub-grain boundaries is analyzed to determine the orientation and activation of slip systems (Section 6.2.1). As shown in Fig. 6-1, in several grains the distribution of pixel-wise orientations (determined in the same way as for grain boundaries) exhibits a strong maximum. A comparison between all bijectively mapped grains (image pairs described in Chapter 4) leads to the conclusion that this (strongest) maximum is predominantly in good agreement ($\lesssim 5^\circ$) with the trace of the basal plane. The latter is defined as the plane perpendicular to the mean c-axis orientation. A maximum in the distribution of orientations is considered if more than 20% of all sub-grain boundary orientations lie within a range of 5° (up to 5 maxima within a single grain can theoretically be found). 15-20% of all orientation maxima exhibit a significant deviation from the trace of the basal plane. The mean deviation in these cases amounts $80-85^\circ$ (the range of misorientations is $0-90^\circ$).

Assignment of c-axis misorientations

In contrast to grain boundaries, the spacing between individual sub-grain boundaries can be significantly smaller. It approaches the width of the widest sublimation grooves (≈ 0.04 mm, Fig. 4-5). In Section 4.4.2, c-axes measurements in a range of up to 0.6 mm on both sides around the transformed position of extracted sublimation grooves are considered to reduce the influence of c-axis measurements assigned to the false side of the boundary. Frequently, a similar range around sub-grain boundaries would enclose measurements across neighboring sub-grain boundaries. Consequently, an assignment of misorientations to individual sub-grain boundaries is not feasible.

A reduction of the range of uncertain assignment (referred to as range of tolerance in Section 4.3.2) would allow deriving a second, fine matching step (Section 4.5). It requires an independent extraction of sub-grain structures from c-axis measurements (Section 6.3.2).

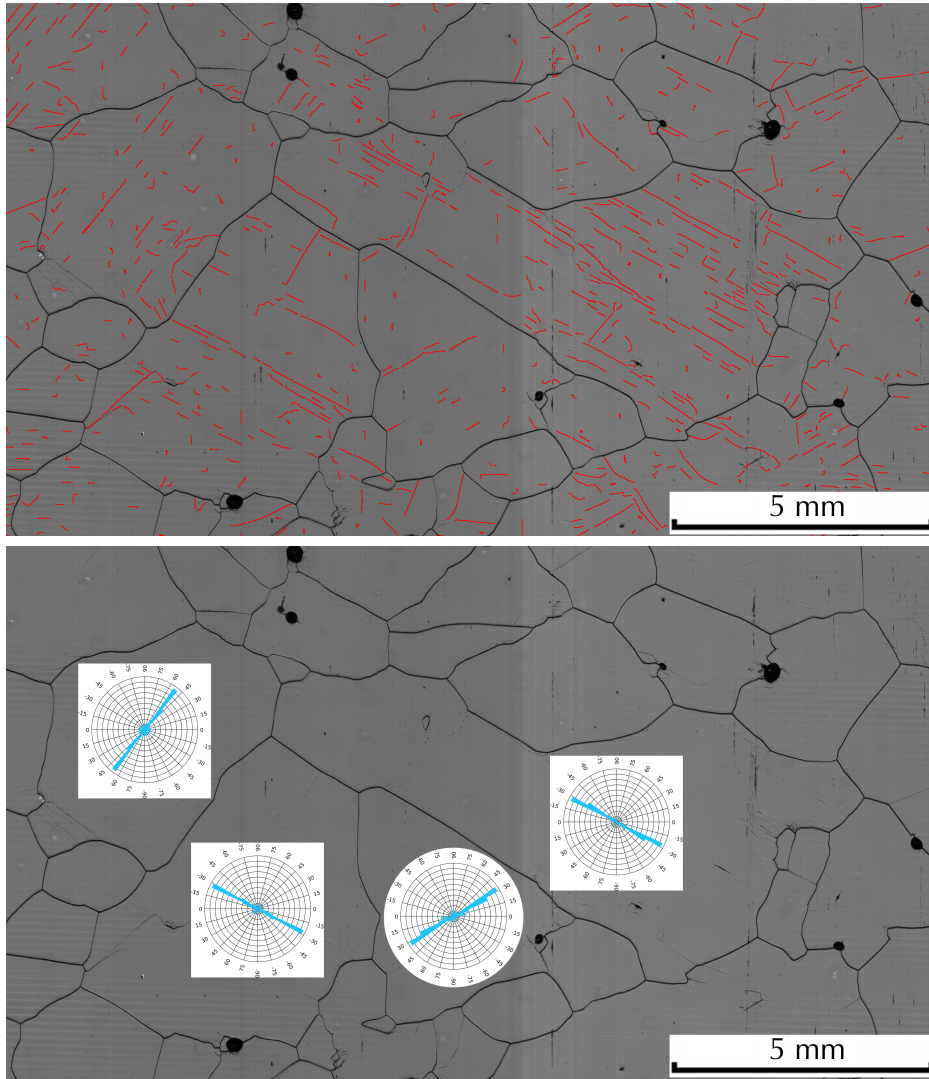


Figure 6-1: Frequently, the distribution of pixel-wise orientations of extracted sub-grain structures (top) exhibits a strong maximum. Corresponding rose plots (bottom) are scaled by the highest frequency. NEEM, 443 m.

6.2.4 Error estimation of sub-grain boundary density

The extraction of narrow, faint sublimation grooves is optimized to reveal a low number of artificial structures, however, at the expense of incompleteness. As an assignment of c-axis misorientations is not feasible, correct and artificial sub-structures cannot be discriminated automatically. In contrast to the threshold of 5° to distinguish grain boundaries from sub-grain boundaries, a threshold to identify artificial structures has not been established and depends strongly on noise and resolution of the applied fabric analyzer (see Sections 2.4.2 and 5.7.3). Even more unclear is the discrimination between artifacts and sub-grain boundaries when extracted from sublimation groove images.

Weikusat *et al.* (2009b) extracted sub-grain boundaries manually from about 2000 grains of the EDML data set (ca. 100 grains per section). The developed method of automatic extraction introduced here allows processing of a statistically much more significant number of grains. However, a comparison between sub-grain boundary densities obtained by application of both approaches to sublimation groove images of the EDML data set leads to a deviation by a factor 1.5 to 2. An example of this significant deviation is shown in Fig. 6-2. Interruptions of almost entirely extracted sub-grain boundaries are reliably identified, whereas other sub-grain boundaries, especially those exhibiting short spacing in between, are not extracted at all. However, the strongest ones, with the most probably highest misorientations thus physically most relevant sub-grain boundaries can be extracted reliably.

For the described configuration of parameters, the radius of the pixel-wise considered neighborhood for calculation of the boundary tensor is most critical as it corresponds to 0.04 mm (EDML images), respectively, 0.06 mm (NEEM images) according to Eq. 3.1. As this radius is in the order of the spacing between several sub-grain structures the feasibility to derive the predominant direction of the gradient from the response to the boundary tensor is considerably affected. However, consideration of a smaller neighborhood would not provide the required smooth-

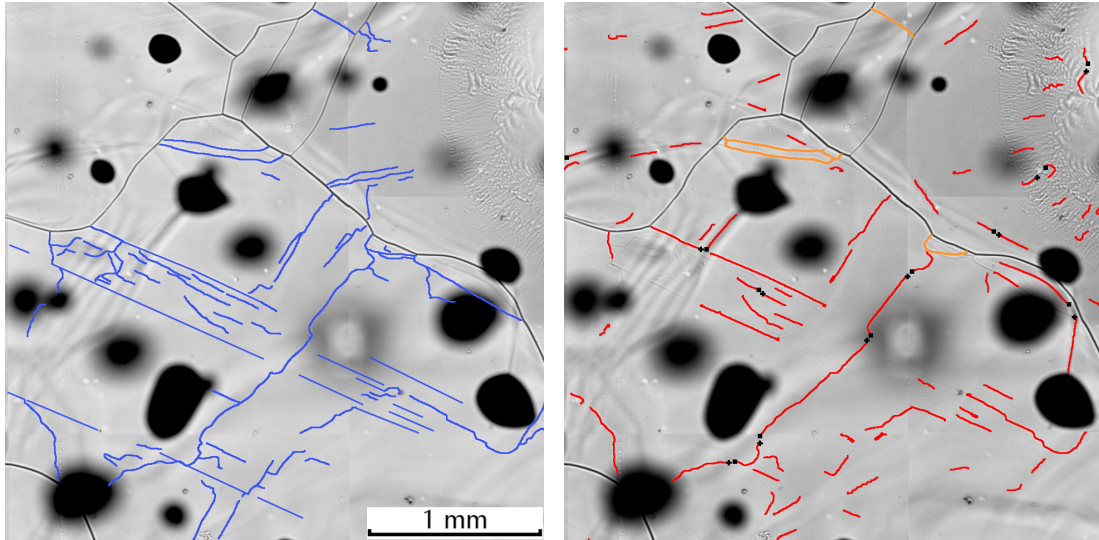


Figure 6-2: Left: Manually extracted sub-grain boundaries as described by Weikusat *et al.* (2009b). Right: Automatically extracted sub-grain boundaries. Sub-grain boundaries initially extracted as grain boundary are labeled in orange and are identified based on mean gray values. Black squares and crosses indicate automatically found connections between separated sub-grain boundaries using a heterogeneous Mahalanobis distance measure. Artificial structures emerge in the upper right corner of the image (EDML, 256 m).

ness of gradient directions. Intersections of sub-grain boundaries constitute the extreme case of narrow spacing and are not extracted.

6.3 C-axes misorientation

6.3.1 Scientific relevance

Apart from the density of visible sub-grain structures, information on the corresponding boundary energies are required to estimate stored strain energy. The dislocation model introduced by Read & Shockley (1950) comprises a strong dependence of sub-grain boundary energy on the full crystallographic misorientation. EBSD and X-ray Laue diffraction measurements constitute an opportunity to obtain this information for manually selected sub-grain boundaries only (Weikusat *et al.* , 2011a,b), whereas automated fabric analyzers allow, in principle, to analyze c-axes misorientations more systematically. As such measurements do not reveal a-axes misorientations the derived energy would be underestimated

(Faria *et al.* , 2013b).

6.3.2 Preliminary results toward automatic extraction

The extraction of sub-grain structures from fabric analyzer measurements represents the first step to derive a transformation rule (fine matching) per grain required for a reliable assignment of c-axis orientations to extracted sublimation grooves. In a first attempt, for every position the angle enclosed by the c-axis orientation and the mean orientation of c-axes in the grain (Section 5.7.2) is determined. Similar to sublimation grooves, a dedicated Random Forest classifier allows to enhance the response of internal structures resembling previously labeled ones. In comparison to extracted sublimation grooves, artificial structures emerge frequently (Fig. 6-3). Analysis of cross-correlations have led to the preliminary conclusion that the range of tolerance cannot be reduced.

6.4 Potential for improvements

6.4.1 Extraction of smooth directions of the gradient

The inadequacy of the present approach to extract a portion of narrow, faint sublimation grooves can be traced back to the small spacing in between. This distance matches frequently the radius of the pixel-wise considered neighborhood for calculation of the boundary tensor (Section 6.2.4). As a smaller radius does not provide a sufficient smoothness of gradient directions, an additional edge-enhancing smoothing step is required. For instance, utilization of anisotropic diffusion (Weickert, 1998) would allow to reduce the neighborhood for calculation of the boundary tensor in size and, therefore, the smallest resolvable spacing between individual sub-grain boundaries. The computing effort to solve the underlying nonlinear partial differential equations impeded the systematic application so far.

However, following the reasoning by Heilbronner & Barrett (2013) (Section 2.2), a more obvious step would be to adjust the applied image acquisition systems to sub-grain boundaries. Acquisition of sublimation groove images can be performed

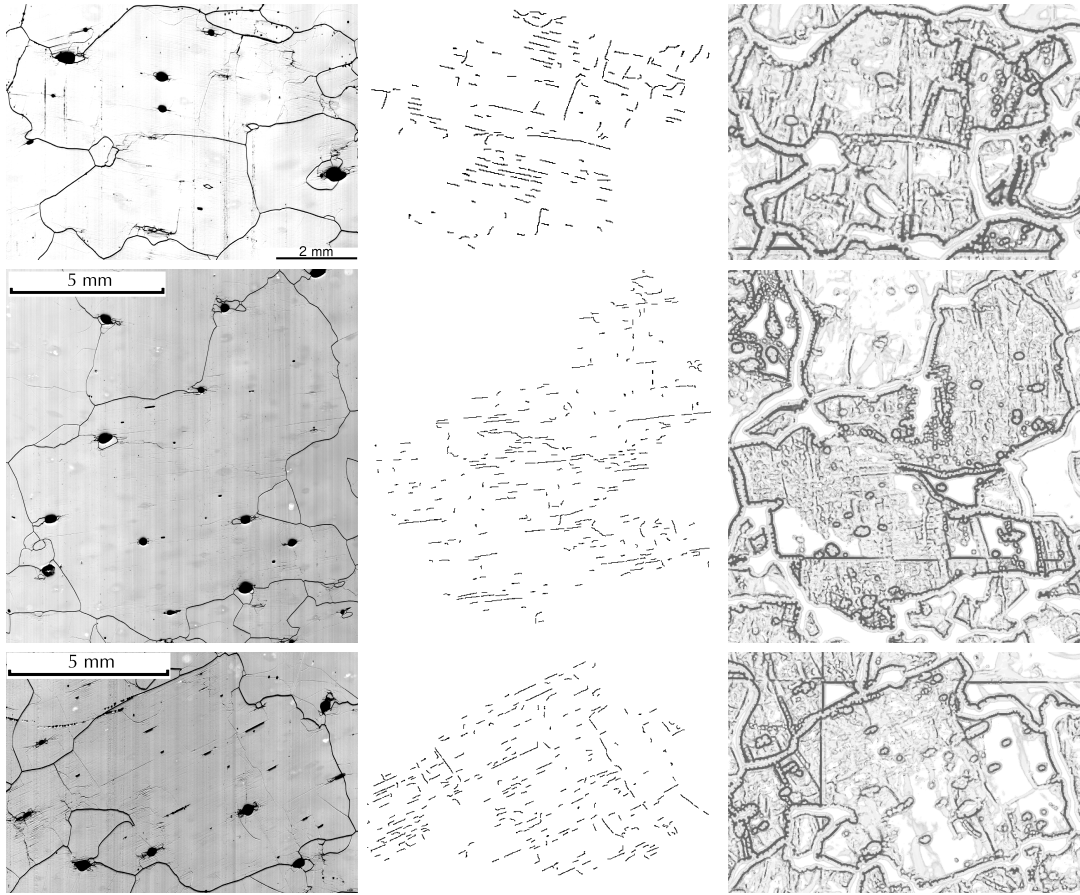


Figure 6-3: Middle column: Extraction of sublimation grooves for which information on misorientation are inaccessible. Right: Visualization of the angle enclosed by pixel-wise c-axis orientation and the mean orientation per grain. Structures are enhanced by dedicated Random Forest classifier. Left: Corresponding sublimation groove images (enhanced contrast). NEEM, 850 m (top), 1026 m (middle, bottom).

within a few seconds utilizing the large area scanning microscope (Section 2.3.2). If a deceleration of the scanning speed and a reduced light intensity can increase the visibility of narrow, faint sublimation grooves, the additional expense for coming microstructural analyses along ice cores will be less than currently required in terms of image processing. It is expected that sublimation under the influence of precisely controlled temperature, humidity and air flow (suggested in Section 5.4.1) enhances even the visibility of sub-grain boundaries.

6.4.2 Assignment of c-axis misorientations

After application of the median filter, the smallest resolvable structure from c-axes measurements is 0.06 mm wide. As this value forms a lower bound for the range of tolerance, the potential for improvements of the described attempt in terms of the reliable assignment of c-axis misorientations to extracted sublimation grooves is limited.

The *G50* fabric analyzer obtains information about the orientation of c-axes by combination of images illuminated from different angles and acquired by different alignments of the crossed polarizers. Owing to the optical anisotropy of ice (Section 2.4.1), variations in color and brightness between grains occur. Under favorable directions of illumination, sublimation grooves are captured in similar quality to the separate method of sublimation groove mapping.

As already mentioned in Section 5.4.1, deviations between grain boundary networks in the combined method induced by reversing and thinning (see Fig. 2-1) could be prevented if sublimation grooves were mapped on the surface of the thin section. In a novel approach to be tested in future, narrow, faint sublimation grooves are mapped on the surface of thin sections utilizing the fabric analyzer as well as the large area scanning microscope. In this case, the inclination of the grain boundary surface does not limit the accuracy in the position of grain boundaries and the range of tolerance can be reduced to less than 0.06 mm. This can be achieved in a second, fine matching step in which the cross-correlation

between separately extracted sublimation grooves is evaluated. In this way, an assignment of misorientations to narrow, faint sublimation grooves would become possible. This includes an automatic extraction of artifacts.

Chapter 7

Evolution of micro-dynamic properties with depth

7.1 Introductory remarks

Studies on grain growth in polar ice have been performed for several decades (see review by Faria *et al.* , 2013a). In contrast, systematic microstructure analyses aiming to collect evidence for dynamic recovery and recrystallization along deep ice cores have not been possible in the past. Pioneering work was conducted by Weikusat *et al.* (2009b) by means of semi-automatic processing of a small fraction of the EDML data set. This explains the lack of comparative studies.

7.2 Grain growth

7.2.1 Current models

Grain growth is driven by a reduction of free energy associated with the grain boundary surface. An increase of mean grain size reduces the grain boundary density per unit volume and leads to an energetically more favorable structure. Grain growth occurs as grain boundary migration, the driving force is inversely

proportional to the grain boundary's radius of curvature (Alley *et al.* , 1986a). For grains smaller than the mean grain size it is negative (Hillert, 1965), i. e. the boundary of an adjacent larger grain will migrate until the small grain is consumed. The boundary velocity is inversely proportional to the grain radius (Burke & Turnbull, 1952).

Normal grain growth is a continuous process in which the microstructure reaches a quasi-stationary state. During normal grain growth a foam structure is expected (Bons *et al.* , 2001). The derivation of Burke & Turnbull (1952) and most mean field theories of grain growth (e. g., Humphreys & Hatherly, 2004) predict a linear increase of the mean grain size (cross-sectional area) with age. As reviewed by Cuffey & Paterson (2010), the mean grain size D^2 at age t is usually expressed by

$$D^2 = D_0^2 + k_g t, \quad (7.1)$$

for an initial mean grain size D_0^2 . The grain growth rate k_g depends on the temperature dependent mobility of grain boundaries and is usually expressed by an Arrhenius type relation of the form

$$k_g = k_0 \exp\left(-\frac{Q_b}{RT}\right) \quad (7.2)$$

with a constant coefficient k_0 , the apparent activation energy for grain boundary self-diffusion Q_b , the gas constant R and temperature T . Except for a large gradient in the uppermost firn, the temperature remains constant over several hundred meters at deep ice core drilling sites in Antarctica and Greenland. The temperature profile along the EDML ice core is described by EPICA community members (2004), whereas the temperature profile along the NEEM ice is approximated by Dahl-Jensen *et al.* (2002). As the centers of most grains do not coincide with the analyzed cross-section, a correction factor of 1.3 (Thorsteinsson *et al.* , 1995) or 1.5 (Fisher & Koerner, 1986) has sometimes been applied.

In the upper part of polar ice sheets a steady increase in grain size has been found

in several ice cores from Greenland and Antarctica (e. g., Thorsteinsson *et al.* , 1997; Gow *et al.* , 1997; Svensson *et al.* , 2003; Wang *et al.* , 2003). The concept of normal grain growth has been applied for parameterization (Gow & Williamson, 1976; Alley, 1992) and the good agreement has been interpreted as evidence that the driving force in firn should be related to the reduction of grain boundary free energy (Stephenson, 1967; Gow, 1969). The occurrence also implies that the strain energy is relatively small (Duval, 1985). These interpretations have been questioned by recent studies on firn (Kipfstuhl *et al.* , 2009) and deep ice cores (Weikusat *et al.* , 2009b; Faria *et al.* , 2013a,b).

7.2.2 Grain size

Evolution with depth

Different methods to quantify grain size have been applied in the past (Section 5.2.1). In particular, the size of the smallest visible grain differs between sublimation groove mapping (utilized for the present analysis) and c-axes orientation measurements (predominantly applied for previous analyses) (Kipfstuhl *et al.* , 2009). Furthermore, differences in the considered fraction of grain sizes may affect absolute values of grain size as well as general trends. For the NEEM and EDML data set, the lower cut-off in grain size is consistently defined by the grain size characterized by the fact that larger grains cover 95% of the surface of the ice core section. In Fig. 7-1, the evolution of corresponding mean values with depth is shown. Shaded ranges represent the standard deviation, whereas the error bars (set to 20%) for the depth regime close to bedrock reflect the high uncertainty caused by grains of a size similar to the entire section. According to Duval & Lorius (1980), the surface of the ice core section is divided by the number of visible grains to obtain a rough estimate.

Sources of error in grain size parameterization

The influence of small-grain artifacts is limited by the cut-off in grain size. The effectiveness is verified manually (described in Section 5.2.2) and automatically

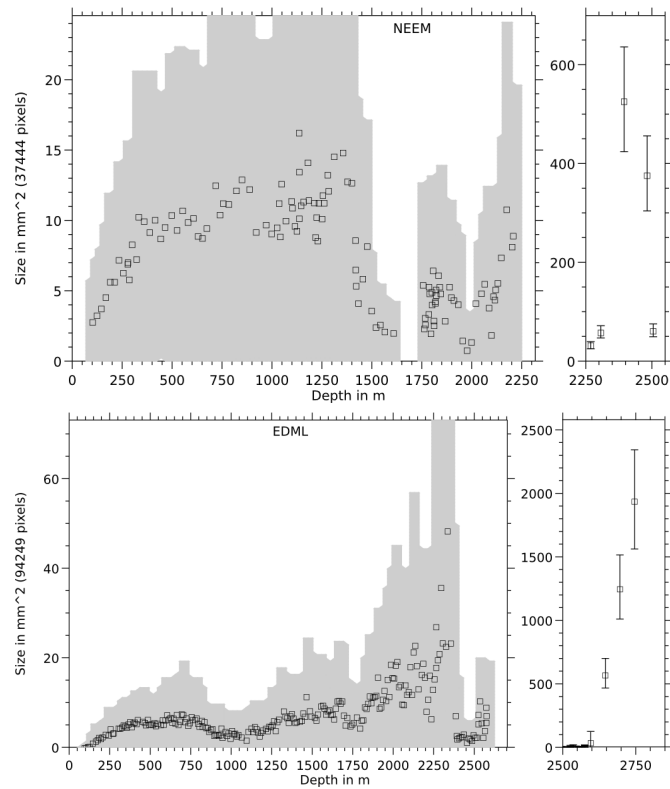


Figure 7-1: Mean grain size measured along the NEEM (top) and EDML (bottom) ice core. Shaded ranges represent standard deviation. Depth regimes close to bedrock have been analyzed by manual counting of visible grains, error bars reflect uncertainty of this estimation.

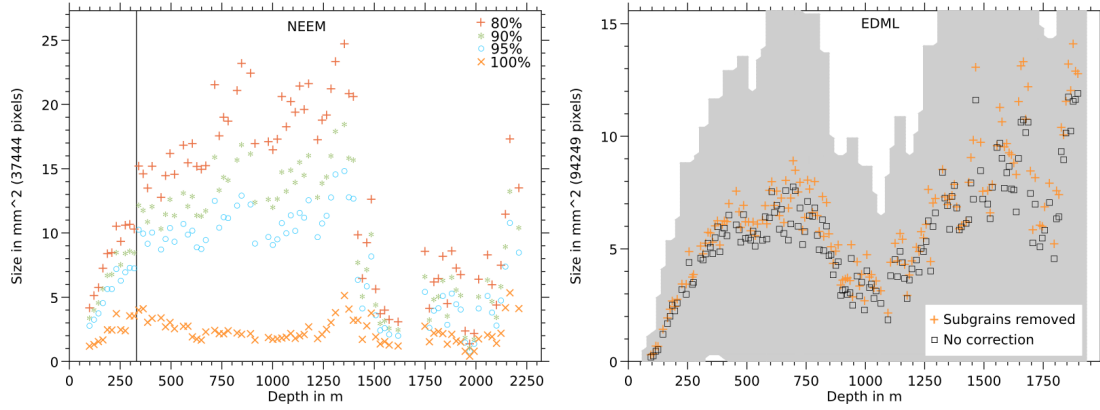


Figure 7-2: Left: Mean grain size measured along the NEEM ice core for different definitions of lower cut-off in grain size, vertical line marks sudden increase explained in Section 7.2.3. Right: Mean grain size measured along the EDML ice core, influence of subsequent removal of sub-grain boundaries from grain boundary network is illustrated. Shaded range represents standard deviation of uncorrected profile.

(described in Section 5.3.2). However, the choice to consider 95% of the area is arbitrary. Varying this fraction and studying the sensitivity of the calculated mean to the actual definition of the cut-off may provide further information. In the left part of Fig. 7-2, the grain size profile along the NEEM ice core is shown for different definitions. It is obvious that the derived grain growth rate increases for higher grain size cut-offs, which clarifies the difficulty to compare the grain size evolution observed along ice cores by means of different methods. Between 320 and 330 m a sudden increase in mean grain size occurs (irrespective of the considered fraction) which is further discussed in Section 7.2.3.

The right part of Fig. 7-2 shows the influence of the subsequently performed removal of sub-grain boundaries (inadvertently extracted as grain boundaries) based on gray value thresholding (Section 2.3.2). The induced increase in mean grain size is of the order of 10-20%.

Error estimation

Both the error induced by invisible/unextracted grain boundaries (Section 5.3.1) and the error induced by artifacts among extracted sublimation grooves (Section 5.3.2) are of the order of 10%. As both errors occur in general, the lower cut-off

in grain size should be kept fixed for a reasonable way to estimate the actual influence. Automatic corrections of the extracted grain boundary network are performed in such a way that excessive occurrence of only one type of influence is avoided. In that respect, the reliability of the algorithm to identify scratches is exemplarily evaluated in Section 5.4.2.

Other sources of error occurring for the NEEM data set are significantly smaller. It therefore seems appropriate to specify the error in mean grain size by 10%. A more accurate, individual specification is possible for sections for which mapping of sublimation grooves and c-axes measurements are automatically matched. Matching of all sections from the NEEM data set forms a medium-term objective and is not pursued in the present context. The area of the cross-section covered by reliably matched grain structures is partially only about 50% (Section 4.3.3). Further development of methodology is required in order to perform systematic grain size analysis exclusively on the basis of matched structures.

Matching of independent measurements of grains and grain boundaries is not feasible for the EDML data set. However, the influence of sub-grain boundaries can be estimated systematically (Fig. 7-2). The frequency of invisible/unextracted grain boundaries cannot be quantified automatically. It is assumed that, similar to the removal of vertical scratches in images of the NEEM data set, even “correct” grain boundaries are occasionally removed together with artificial boundaries matching tile borders of the EDML micrographs.

In the shallowest analyzed section of the NEEM ice core (102 m) the proportion of visible bubbles is $\approx 5\%$ and decreases with depth, whereas the proportion of bubbles in sections of the EDML ice core (after removal of bubbles exhibiting blurred edges inside of grains) amounts to 23% at 150 m depth and decreases to 7% at 200 m (3% at 400 m). For the calculation of the grain growth rate, an error of 20% is assigned to mean grain sizes obtained between 150 and 200 m depth. As the error for shallower depth is even higher, these depths remain unconsidered. Beyond 200 m, sub-grain boundaries among extracted grain boundaries represent

the dominating source of error.

Growth rates

By regression analysis, Cuffey & Paterson (2010) derived the coefficient k_0 and the activation energy for grain boundary self-diffusion Q_b (see Eq. 7.2) from growth rates measured along several ice cores drilled in Greenland and Antarctica. In contrast to the present analysis of grain size, previous studies have not provided error estimations. Consequently, the closeness of agreement between measured growth rates and those predicted by Eq. 7.2 cannot be compared quantitatively. Owing to the application of correction factors and the exclusive consideration of largest grains, grain sizes and growth rates of previous studies are systematically higher than those taking (almost) the whole grain size spectrum into account (Kipfstuhl *et al.* , 2009).

In Fig. 7-3, grain growth rates derived from the NEEM and EDML data set are compared to the prediction of Cuffey & Paterson (2010). The obtained growth rates are significantly lower which indicates that the systematic difference due to methodical differences exceeds the error associated with the present image acquisition and image processing approach. The difference in grain growth rate between the NEEM and EDML drill site at shallow depths can be traced back to the difference in mean annual surface temperature (NEEM: -29°C , EDML: -44.6°C) (NEEM community members, 2013; EPICA community members, 2004). At greater depths, the generally lower concentration of dust particles in Antarctica compared to Greenland (Lambert *et al.* , 2008; Ruth *et al.* , 2003) induces that larger grains are found (for the coupling, see Section 7.2.3).

Growth rates along the NEEM ice core depend on the considered depth range. The average growth rate in the upper 615 m is significantly lower than in the upper 330 m which can be explained by an increased frequency of small grains as shown in Fig. 7-4. In good agreement, Svensson *et al.* (2003) performed a grain size analysis in the upper 880 m of the NorthGRIP ice core (Greenland, -32°C mean annual surface temperature) and observed the appearance of a sec-

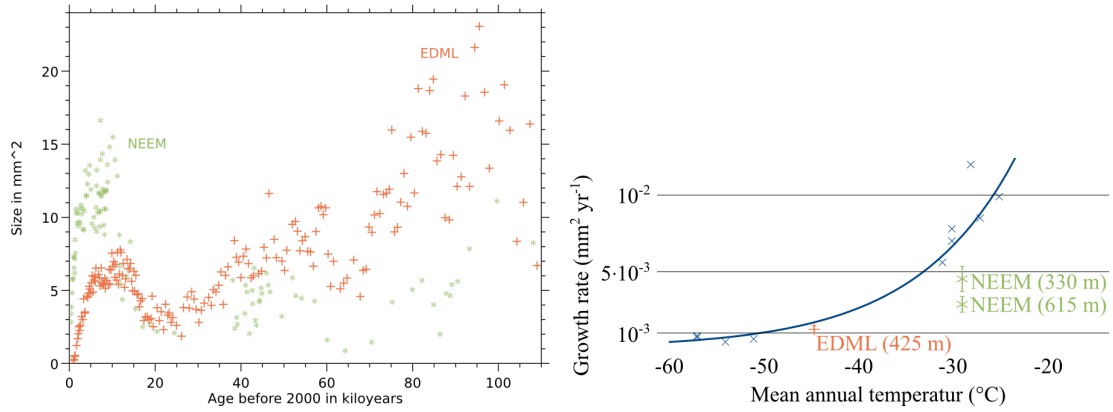


Figure 7-3: Left: Comparison of mean grain size profiles (NEEM and EDML ice core) based on chronology. Right: Comparison of derived grain growth rates (NEEM and EDML ice core) with model of normal grain growth (Cuffey & Paterson, 2010).

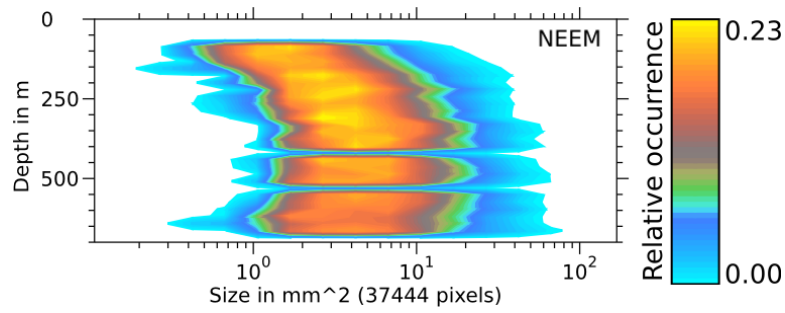


Figure 7-4: Grain size distribution for shallow depths of NEEM ice core.

ond mode of smaller grains between 400 and 500 m depth. Synchronized with the transition from the current interglacial to the last glacial (at 1419 m, NEEM community members, 2013) significantly smaller grains are observed. The most plausible explanation is that impurities exert a pinning pressure on grain boundaries (Thorsteinsson *et al.*, 1997). Changing impurity concentrations play an important role for the grain size evolution and are further discussed in Section 7.2.3.

7.2.3 Influence of changing impurity concentrations

The sudden increase in mean grain size along the NEEM ice core from 320 m ($\approx 7 \text{ mm}^2$) to 330 m ($\approx 10 \text{ mm}^2$) exceeds the assigned error of 10%. The question arises whether this change can be traced back to a change in chemical impurity

concentrations. Hörhold *et al.* (2012) showed that impurities may have a significant impact on the densification of polar firn. Seasonal cycles of Ca^{2+} and density measured along the B29 firn core (Greenland) show a strong correlation at 30 m (water equivalent) depth. Regarding grain size, it is commonly assumed that fluctuations may be the result of interannual variability in the amount of impurities or deviations from the annual-layer thickness (e. g., Svensson *et al.* , 2003).

A specific feature of the NEEM data set is that mean grain size can be extracted continuously for depth intervals of 55 cm. A running mean is calculated by considering all grains (larger than the cut-off) in a window covering a depth range of 6 mm. A grain is assigned to the running mean if the center of mass of the grain is located within the depth range or if the distance does not exceed the equivalent grain radius (defined in Section 5.2.2).

In Fig. 7-5, the continuous profile of mean grain size is compared to the concentration of ammonium ions (NH_4^+) and the number of measured dust particles (in a reference volume). These (currently unpublished) measurements have been performed at the University of Bern, methodically based on Röthlisberger *et al.* (2000); Kaufmann *et al.* (2008). It is obvious that the strong variability in grain size is not adequately represented by the mean values as a random selection of a smaller depth range can lead to significantly different mean values. Here, ammonium ions and dust particles have opposing effects on grain size. Contradictory observations and interpretations exist concerning the influence of ammonium on grain size. Alley & Woods (1996) found a negative correlation between grain size and the concentration of ammonium, whereas a higher frequency of crystallographic defects induced by the incorporation of ammonium can explain a positive correlation (Glen, 1968). The impeding effect of dust particles on grain growth has been analyzed by Durand *et al.* (2006a).

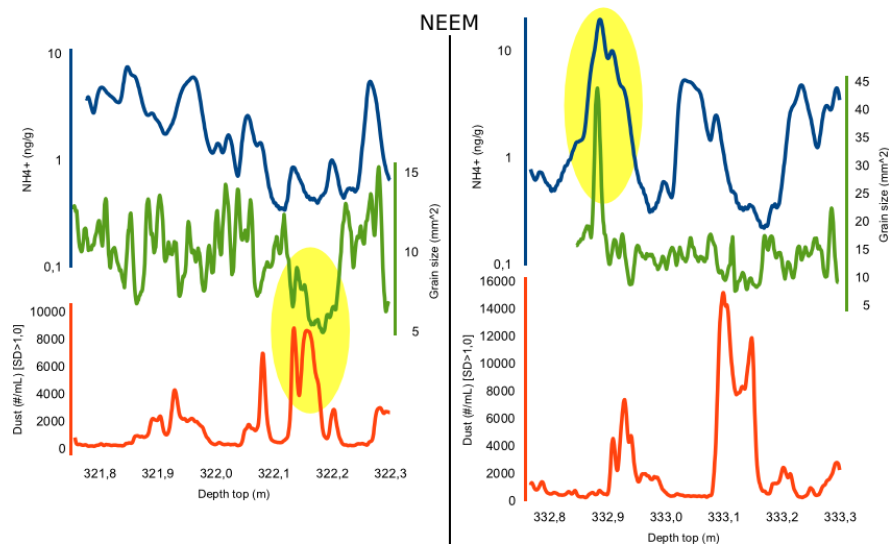


Figure 7-5: Comparison between running mean of grain size (green) with concentration of ammonium (blue) and dust content (red) for 55 cm depth ranges of NEEM ice core, 322 and 333 m.

7.2.4 Grain size sensitivity and vertical strain rate

Composite flow laws

As demonstrated in Figs. 7-4 and 7-5, mean grain size may coincide well with a large proportion of the grains, but smaller as well as larger grains are effectively ignored. By consideration of full grain size distributions and related differences in rheological properties, a discrepancy between observations of calcite mylonites in the laboratory and nature could be solved by Herwegh *et al.* (2005). The basic assumption in composite flow laws (e. g., Freeman & Ferguson, 1986) is that small grains deform by other creep mechanisms than large grains. This is apparently a severe simplification as incompatibilities imposed by neighboring grains (of possibly different size) remain unconsidered.

Vertical strain rate

One reason why composite flow laws have not yet been applied to grain size distributions extracted along ice cores is that an application is usually associated with the assumption of constant strain or constant strain rate (e. g., De Bresser *et al.*, 2001). The Dansgaard-Johnsen model (Dansgaard & Johnson, 1969)

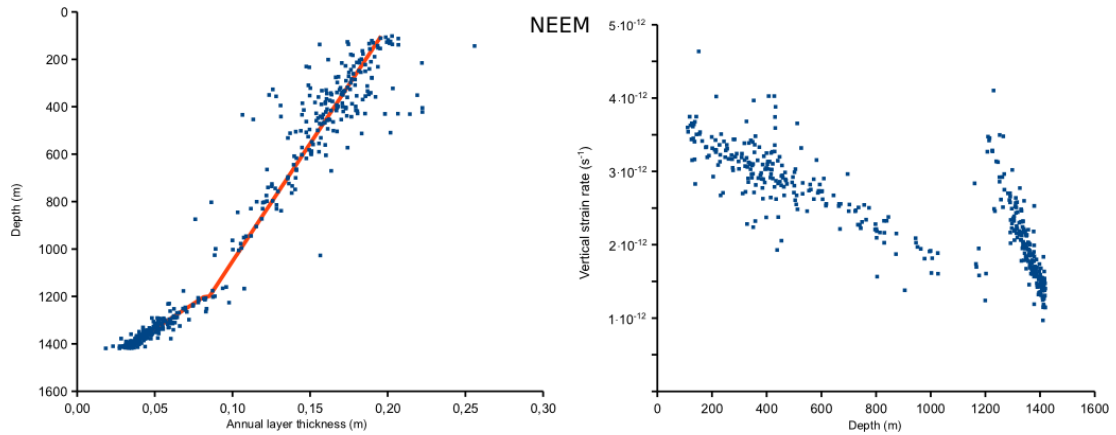


Figure 7-6: Left: Annual layer thickness for upper part of NEEM ice core (Rasmussen *et al.*, 2013). Right: Derived vertical strain rates considering thinning of annual layers.

predicts a dominating, constant vertical strain rate for the upper two thirds of the ice sheet, whereas in the lower ice column vertical shear becomes the main driver for ice deformation. Alternatively, if intervals of constant accumulation rate are assumed, a derivation of vertical strain rates from the thinning of annual layers becomes possible. To the author’s knowledge, it is unclear which assumption is more realistic. However, in the second case, proposed here, the chronology derived for ice cores providing valuable information is taken into account.

For the NEEM ice core the evolution of annual layer thickness has been determined by Rasmussen *et al.* (2013). Sublimation groove images of the NEEM data set reveal that pore space is closed off at 100 m depth. This close-off defines the *firn-ice transition* associated with a density of $830 \frac{\text{kg}}{\text{m}^3}$ (Cuffey & Paterson, 2010). The assumption of a constant density of $900 \frac{\text{kg}}{\text{m}^3}$ and a constant accumulation rate for the last 8000 years (corresponding to 1200 m depth) allows to estimate a depth profile of vertical strain rate for this depth regime as shown in Fig. 7-6. A lower accumulation rate is assumed for the time period corresponding to the interval between 1200 and 1400 m depth. However, the shear strain rate (movement of ice in horizontal direction) in this depth regime (estimated by Montagnat *et al.*, 2014) reaches a value of 10^{-12} s^{-1} , which means that vertical strain is no longer dominating.

Orowan's equation (Orowan, 1934) relates strain rate (combination of vertical and shear strain) to the density of dislocations (Section 7.4). Among others, Montagnat & Duval (2000) deduced a link between the evolution of grain size and dislocation density under strong assumptions on dominating processes. These assumptions are increasingly questioned (Faria *et al.*, 2013b).

7.3 Densification

7.3.1 Current models

It is unthinkable to study snow deforming under its own weight in laboratory until the pore space is closed off. At drill sites of deep ice cores, this process takes typically several centuries (Cuffey & Paterson, 2010).

Models describing densification as steady burial and sintering process by considering empirical relations between overburden pressure and firn density (e. g., Kameda *et al.*, 1994) have recently been questioned (Hörhold *et al.*, 2012). In the following, focus is laid on the increase in ice density subsequent to the firn-ice transition. It is assumed that bubbles are compressed in one dimension only. Probably, deviations from this assumption can occur locally (e. g., Nye, 1953), but the approximation is valid around ice core drilling sites, where the horizontal stresses are tensile.

7.3.2 Pressurization of air bubbles

The question arises how long the pressurization of air bubbles takes. At the firn-ice transition, the pore space has just been closed off. Consequently, the pressure of air bubbles corresponds to atmospheric pressure. Measurements of bubble pressures would provide information on the process of pressurization. To the author's knowledge, the only measurement of unrelaxed bubble pressure has been performed by Lipenkov *et al.* (1997) along the Vostok ice core. The obtained profile suggests that the pressurization process extends over 200 m. This observation can only be explained if the difference between bubble pressure and

hydrostatic pressure increases initially.

At the firn-ice transition, the densities of ice (ρ), air bubbles (ρ_B) and bubble-free ice (ρ_I) are given by: $\rho = 830 \frac{\text{kg}}{\text{m}^3}$, $\rho_B \approx 1,5 \frac{\text{kg}}{\text{m}^3}$, $\rho_I = 917 \frac{\text{kg}}{\text{m}^3}$. The volume of air bubbles (V_B) in a unit volume (V) is

$$\rho = \frac{V_B}{V} \cdot \rho_B + (1 - \frac{V_B}{V})\rho_I \Leftrightarrow \frac{V_B}{V} = \frac{\rho_I - \rho}{\rho_I - \rho_B} = 0,095. \quad (7.3)$$

The increase in overburden pressure within 1 m equivalent ice depth is

$$\Delta p = 1 \text{ m} \cdot 917 \frac{\text{kg}}{\text{m}^3} \cdot 9,81 \frac{\text{kg} \cdot \text{m}}{\text{s}^2} = 8996 \text{ Pa}. \quad (7.4)$$

Following the ideal gas law, the product $p_B \cdot V_B$ stays constant if the temperature does not change. Consequently,

$$(p_B + \Delta p) \cdot (V_B - \Delta V_B) = p_B \cdot V_B \Leftrightarrow \Delta V_B = \frac{\Delta p \cdot V_B}{p_B + \Delta p}. \quad (7.5)$$

Next, assume that the volume of air bubbles is compressed in one dimension as much as an accommodation to the increase in overburden pressure requires. The bubble pressure at the firn-ice transition is $p_B = 10^5 \text{ Pa}$. 1 m equivalent ice depth at the firn-ice transition at NEEM corresponds to $\Delta t = 4,1 \text{ a}$ (Rasmussen *et al.*, 2013). This results in a vertical strain rate

$$\dot{\epsilon} = \frac{\Delta V_B}{V \cdot \Delta t} = \frac{\Delta p}{V} \cdot \frac{1}{\Delta t} \cdot \frac{V_B}{p_B + \Delta p} = \frac{\Delta p}{\Delta t} \cdot \frac{\rho_I - \rho}{(\rho_I - \rho_B) \cdot (p_B + \Delta p)} = 6,0 \cdot 10^{-11} \text{ s}^{-1} \quad (7.6)$$

which is about one order of magnitude higher than estimated in Section 7.2.4. The term $\frac{\Delta p}{V}$ stays constant with depth (equivalent ice depth is applied). Δt increases slightly, at 250 m core depth at NEEM $\Delta t = 4,9 \text{ a}$, whereas the ratio $\frac{V_B}{(p_B + \Delta p)}$ decreases.

Density measurements along the GISP2 ice core (Greenland, Gow *et al.*, 1997)

suggests $\rho \gtrsim 910 \frac{\text{kg}}{\text{m}^3}$ at 250 m depth. Therefore, $\rho_I - \rho \lesssim 7 \frac{\text{kg}}{\text{m}^3}$ represents an upper estimate proportional to $\dot{\epsilon}$.

As 250 m core depth corresponds to approximately 120 m equivalent ice depth and the overburden pressure is $p \approx 120 \text{ m} \cdot 917 \frac{\text{kg}}{\text{m}^3} \cdot 9,81 \frac{\text{kg} \cdot \text{m}}{\text{s}^2} = 1,08 \cdot 10^6 \text{ Pa}$.

As a measurement of absolute, unrelaxed bubble pressure at about 250 m depth is not available assume $p_B \approx 10^6 \text{ Pa}$ which leads to

$$\rho_B \approx 14,3 \frac{\text{kg}}{\text{m}^3}, \quad \frac{V_B}{V} \approx 0,0078 \quad \text{and} \quad \dot{\epsilon} \approx 4,5 \cdot 10^{-13} \text{ s}^{-1}. \quad (7.7)$$

Obviously, the increase in overburden pressure below the firn-ice transition is smaller than bubble compression can accommodate for. After an initial increase, the difference between bubble pressure and overburden pressure declines.

7.3.3 Clathration

The depth profile of bubble pressure obtained by Lipenkov *et al.* (1997) suggests that the difference between bubble pressure and hydrostatic pressure increases again at the depth where air bubbles are transformed into clathrate hydrates. Potentially, the change in volume covered by the air inclusion plays an important role and is discussed here.

The mole volume of an air bubble ($V_{m,b}$) depends on the ice temperature and pressure following the ideal gas law:

$$V_{m,b} = \frac{RT}{p}. \quad (7.8)$$

Using $T=250 \text{ K}$ and $p=50 \text{ bar}$ results in a mole volume of an air bubble about $4.1 \cdot 10^{-4} \text{ m}^3 \text{ mol}^{-1}$. The corresponding volume $V_{m,h}$ of a hydrate is given by Uchida *et al.* (1994)

$$V_{m,h} = \frac{VN_0}{n\alpha} \quad (7.9)$$

with the volume of a unit cell of the air-hydrate crystal, $V = 4.91 \cdot 10^{-27} \text{ m}^3$, Avogadro's number $N_0 = 6.02 \cdot 10^{23} \text{ mol}^{-1}$, the number of cages in a unit cell ($n = 24$) and the site occupancy (α) ranging between 0.6 and values larger than 1.0 (Chazallon & Kuhs, 2002). Assuming that the value of α is about unity leads to a mole volume of an air-hydrate crystal about $1.2 \cdot 10^{-4} \text{ m}^3 \text{ mol}^{-1}$ which is less than one third of that of an air bubble. This difference ceases with depths. At the lower bound of the bubble clathrate transition zone, no change in volume is expected.

The difference in covered volume implies that cavities are created in the ice during the transition. This observation as well as the previous discussion on pressurization of air bubbles contribute to explaining the depth profile of grain shape.

7.3.4 Grain shape

As discussed in Section 5.5, the perimeter of grains extracted from sublimation groove images of the EDML ice core is interrupted at sites where bubbles below the surface are visible. The perimeter ratio is especially suitable to compare the case in which interruptions are closed by straight lines (coinciding with the convex hull) with the case in which the boundary of the bubble is considered as grain boundary. In Fig. 7-7, the depth profiles of both parameterizations along the NEEM and the EDML ice are shown. The error of the perimeter ratio induced by errors in extracted grain boundaries has been estimated to $\approx 3\%$ (Section 5.5.3).

As the visible pore space of the considered depth range of the NEEM ice core does not exceed 5%, the difference is much smaller than observed for the EDML ice core. According to Eq. 5.4, the relative difference between the visible pore space in both data sets increases with depths. This explains why despite decreasing bubble size a significant difference between both parameterizations is found for several hundred meters along the EDML ice core.

Both for the NEEM and the EDML ice core a change in the trend is found

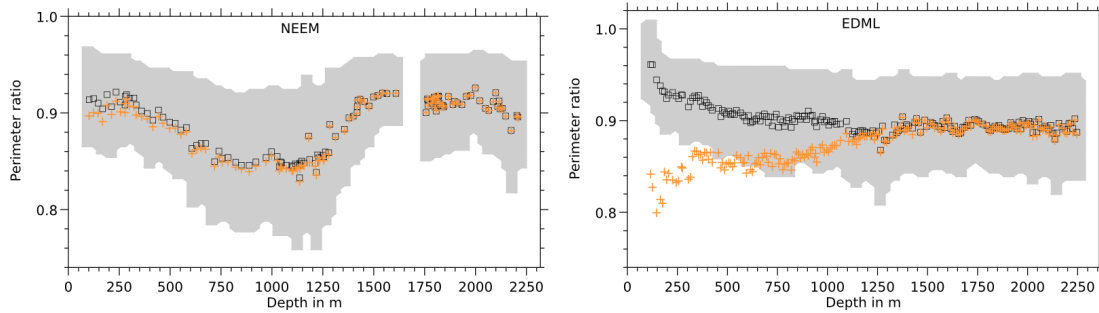


Figure 7-7: Mean perimeter ratio measured along the NEEM (left) and EDML (right) ice core. Black squares: Bubble boundaries are considered as grain boundaries, shaded ranges represent standard deviation. Orange crosses: Bubble boundaries are replaced by straight lines.

at about 300 m depth. For the NEEM data set both parameterizations start declining after a slight initial increase. If bubble boundaries are considered as grain boundaries for the EDML data, the derived perimeter ratio stabilizes at about 0.86. Possibly, deformation between the firn-ice transition and 300 m depth is dominated by densification, which means that bubbles exhibiting lower pressure than the hydrostatic load are slowly pressurized. During this process less incompatibilities between neighboring grains occur than at greater depth as grains can grow almost unhamperedly into bubbles. The considerable growth of grains is associated with the migration of air bubbles from grain boundaries to the inside of grains (Alley *et al.*, 1986b). This explains why grains appear to become more regular for both ice core if bubble boundaries are considered as grain boundaries. This trend ceases at 300 m depth.

For depths greater than 300 m, a trend towards more irregularity is found if bubbles are replaced by straight lines. In accordance with the limited study on the EDML data set by Weikusat *et al.* (2009b), this trend is less pronounced along the EDML ice core than along the NEEM ice core. The difference in temperature induces a difference in grain growth kinetics (see Section 7.2.2). Owing to the difference in accumulation rate (NEEM: 0.22 m, EDML: 0.03 m ice equivalent per year) (NEEM community members, 2013; EPICA community members, 2004), the time during which annual layers are moving down is significant longer at the

drill site of the EDML ice core. Consequently, the effectiveness of recovery is enhanced impeding the development of grain shapes strongly deviating from the energetically favored configuration. To illustrate, snow precipitated 8000 years ago is found in the NEEM ice core at 1200 m depths, whereas only at 500 m of the EDML ice core (Rasmussen *et al.* , 2013; Ruth *et al.* , 2007).

The question arises how much pressure relaxation after drilling the ice core contributed to the development of highly irregular grain shapes along the NEEM ice core. Predominantly small grains are affected (Section 2.2). They are excluded by means of the lower cut-off in grain size. Ice core section between 1040 and 1160 m have been stored several months longer than sections from adjacent depth regimes. The observation that a trend towards more regularity present at 1000 m ceases subsequently can be interpreted as evidence for the influence of relaxation on grain shape. Even though the smooth change of grain shape is contradictory, the influence of relaxation cannot be ruled out. It is hard to believe that the relaxation of air bubbles covering a small volume fraction may affect the entire perimeter of grains. To the author's knowledge, studies focusing on relaxation are very rare (Gow, 1971; Miyamoto *et al.* , 2009).

On the basis of both parameterizations in the range between 800 and 1200 m of the EDML ice core, the onset of the transition from air bubbles to clathrate hydrates becomes obvious (transition at Dome F, Antarctica: 500 - 1200 m, Ohno *et al.* , 2004). The visibility of bubbles below the surface in the EDML data set causes that the "real" perimeter ratio consistent to the values obtained along the NEEM ice core are under- and overestimated, respectively. Consequently, the disappearance induces the convergence of both parameterizations to an intermediate value.

The considerable gap between both parameterization for the upper 1000 m along the EDML ice cores does not allow the identification of a general trend. This is not the case along the NEEM ice core for which a significant trend towards more irregularity is observed between 300 and 900 m depth. At depths greater

than 1200 m, the small gap between both parameterizations ceases providing evidence for the transition from air bubbles to clathrate hydrates (transition at NorthGRIP, Greenland, 900 - 1600 m, Kipfstuhl *et al.* , 2001). This convergence coincides with a clear trend towards more regularity down to about 1500 m depth. The synchronization with the formation of clathrate hydrates can be explained by the generation of cavities (Section 7.3.3). The decline in irregularity proceeds in a way similar to shallow depths where grains can grow almost unhamperedly into bubbles.

7.4 Evolution of dislocation density

7.4.1 Current models

Previous models on the evolution of dislocation density describe the reduction solely by rotation recrystallization apart from the deepest hundreds of meters (e. g., Montagnat & Duval, 2000). The effect of this process on mean grain size is modeled based on *c*-axes measurements (Alley *et al.* , 1995) and the good agreement with observed grain size profiles has been interpreted as verification of these models. However, dislocation density can also be reduced by dynamic recovery and recrystallization. A systematic quantification of the curvature of grain boundaries and the density of sub-grain boundaries allows estimating the contribution of these previously neglected processes.

7.4.2 Grain boundary shape

The problem that bubbles interrupt the perimeter of grains does not affect the characterization of grain boundaries. By limiting the analysis to grain boundaries to those located between two grains larger than the lower cut-off the influence of artificial grain boundaries is reduced. The error of grain boundary curvature has been estimated to $\approx 5\%$ (Section 5.6.3).

Under the assumption that strain-induced grain boundary migration occurs, the curvature of grain boundaries provides an estimation of the difference in dislo-

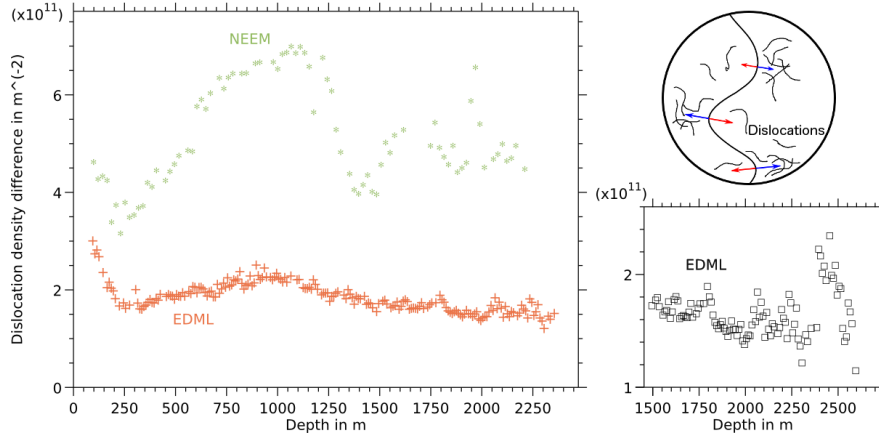


Figure 7-8: Left: Mean curvature (converted to difference in dislocation density) measured along the NEEM and EDML ice core. Top right: Schematic representation of assumed equilibrium between opposing driving forces. Bottom right: Difference in dislocation density for bottom part of EDML ice core.

cation density between both sides of the boundary. This difference represents the driving force for strain-induced grain boundary migrations counteracting the driving force reducing the surface energy (Kipfstuhl *et al.*, 2009; Weikusat *et al.*, 2009b). In Fig. 7-8, the average values calculated for the NEEM and EDML ice core are shown. They are at all depths higher than modeled by Montagnat & Duval (2000).

Curvatures extracted from the NEEM data set are generally higher than those extracted from the EDML data set. Between 100 and 150 m depth the highest curvatures along the EDML ice core and the smallest difference between both depth profiles are found. For both cores the mean curvature decreases down to about 250 m. This trend can be explained by the almost unhampered growth of grains into bubbles exhibiting lower pressure than the hydrostatic load. This influence has already been discussed for the perimeter ratio (Section 7.3.4).

At greater depths, the highest curvature values coincide with the presence of highest bubble pressures (at the onset of the transition from air bubbles to clathrate hydrates) and smallest grain sizes (glacial periods characterized by high impurity concentrations). For the EDML ice core, the influence of relaxation has been strongly limited due to cold storage temperatures at the drill site (Miyamoto

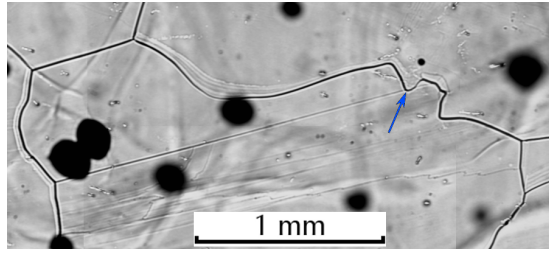


Figure 7-9: High local curvature (indicated by arrow) of a grain boundary induced by sub-grain boundary pinning (EDML, 896 m).

et al., 2009). Consequently, the observation that the curvature of grain boundaries increases with bubble pressure along both ice cores indicates that not only relaxation effects caused the formation of irregular grain boundaries. It is assumed that the presence of pressurized air bubbles influences the migration of grain boundaries (Roessiger *et al.*, 2013).

In the case that grain boundaries are pinned by air bubbles, impurities or sub-grain boundaries, the acting driving force is not related to a difference in dislocation density, but to the exerted pinning pressure. However, in both cases the generation of high local curvatures of grain boundaries is induced. This deviation from a configuration of minimal surface energy is not adequately captured by models considering solely rotation recrystallization.

In Fig. 7-9, a grain boundary exhibiting high curvatures visible in a sublimation groove image from the EDML ice core (896 m) is shown. In this particular case, sub-grain boundaries play an important role.

7.4.3 Sub-grain boundary density

As discussed before, high differences in dislocation density as well as pinning of grain boundaries by sub-grain boundaries can induce high local curvatures of grain boundaries. During recovery sub-grain boundaries are formed by alignment of dislocations. In Fig. 7-10, the densities of automatically extracted sub-grain boundaries along the NEEM and EDML ice core are shown. Based on a comparison to manually extracted densities of sub-grain boundaries, it is concluded that

typically only the half of sub-grain boundaries is automatically detected (Section 6.2.4). As illustrated in Fig. 6-2, some grain boundaries are subsequently classified as sub-grain boundaries. The influence of their removal as grain boundary on mean grain size is shown in Fig. 7-2. Here, the increasing influence on the density of sub-grain boundaries is shown.

It is remarkable that the density of sub-grain boundaries in the upper 750 m of the EDML ice core is twice as high as observed in the NEEM ice core. The noticeable difference in the depth profiles of the perimeter ratio has been explained by the assumption that recovery is more effective along the EDML ice core. The observation of high densities of sub-grain boundaries confirms this assumption. Synchronized with the formation of clathrate hydrates in the EDML ice core, the density of sub-grain boundaries decreases. As grain boundaries exhibit high curvatures at this depth, it seems that the balance between strain-induced grain boundary migration and recovery is displaced towards more effective strain-induced grain boundary migration. However, contradictions exist concerning the development in greater depths.

Both impurities and sub-grain boundaries can exert a pinning pressure on grain boundaries. A comparison of the profile of sub-grain boundary densities to stratigraphic layers visible in radar profiles along the NEEM ice core suggests that both aspects may be closely related. Those layers are characterized by a high concentration of impurities (Svensson *et al.*, 2005). It is assumed that impurities impede the glide of dislocations by representing obstacles at which dislocations are aligned into sub-grain boundaries (Glen, 1968). In this way, high concentrations of impurities exert influence on grain boundaries by means of sub-grain boundaries.

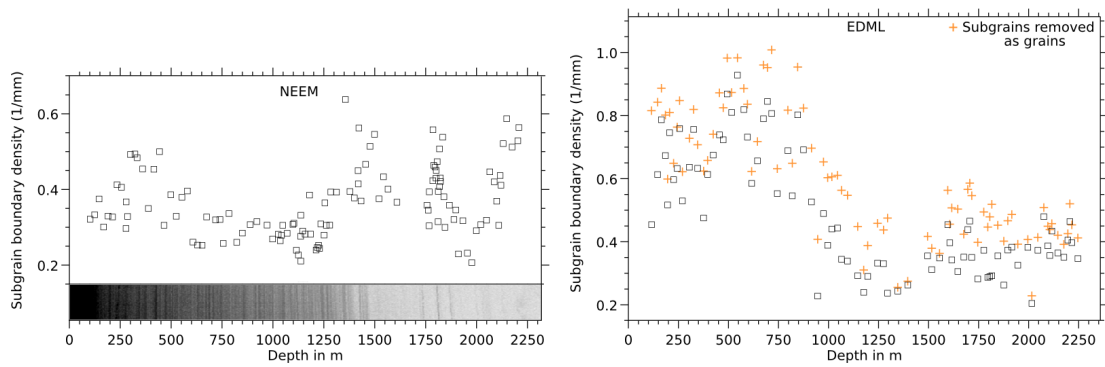


Figure 7-10: Mean sub-grain boundary density measured along the NEEM (left) and EDML (right) ice core. Left: Comparison with radar depth sounder profile at NEEM drill site, CReSIS (Gogineni). Right: Comparison between initial density (black) and density considering sub-grain boundaries inadvertently extracted as grain boundary.

Chapter 8

Summary

A digital image processing approach has been developed to extract microstructural information from large sets of sublimation groove images acquired along deep polar ice cores. The method has been applied to image data from the EDML (East Antarctica) and NEEM (Greenland) ice cores. A particular characteristic of this analysis technique is the high resolution of the mapped grain boundary networks. This represents a significant improvement in comparison to previously applied methods like c-axes orientation measurements. The automatic extraction of grains and grain boundaries enables a fast parameterization of grain boundary networks, which in turn allows for a high vertical resolution along the core. With the novel method mean values of grain size, grain shape and the shape of grain boundaries can be derived in a consistent way from a large amount of data.

Due to the higher vertical resolution of grain geometry parameters presented in this study, it becomes clear that previous assumptions about strength and variability of internal stresses have to be questioned. The results support recent studies (Kipfstuhl *et al.* , 2009; Weikusat *et al.* , 2009b; Faria *et al.* , 2013b) which reported that the dominating recrystallization processes are not only dependent on depth.

In this context, the development of a preferred orientation of c-axes plays an

important role. For all sections of the NEEM ice core for which sublimation grooves have been mapped, the orientation of *c*-axes has been acquired subsequently. The analysis of the *c*-axes orientation by means of the here presented image processing techniques is subject of a Diploma thesis (Eichler, 2013).

The availability of highly resolved grain boundaries and the orientation of *c*-axes for the same set of ice core sections provides the possibility to compare the results from these two very different methods and to estimate possible errors. An automatic matching algorithm has been developed to estimate errors in the parameterization of grain boundary networks, which arise as missing or falsely detected grain boundaries during acquisition and processing of sublimation groove images. A long-term perspective is to systematically assign *c*-axis misorientations to reliably extracted, highly resolved grain boundaries from sublimation grooves. For six automatically matched NEEM image pairs the area fraction of grain cross-sections reliably assigned to *c*-axes orientation lies in the range of 50-80%. The presented matching algorithm has been found to be an effective tool for error estimation and for identifying problems in the assignment of grains and grain boundaries.

During this study several ideas to improve the image acquisition method have been developed. Unpredictable sublimation behavior can be reduced if grooves on the polished ice surface evolve in a chamber of defined climatic conditions, which is technically feasible even at drill sites. Manual adjustment of the focus is no longer necessary if ice core sections are cut to uniform thickness. Subsequent to mapping of sublimation grooves, thick sections of the NEEM ice core have been further processed to thin sections. It is assumed that sublimation grooves mapped on the surface of thin sections exhibit less deviations in comparison to the measurement of *c*-axis orientation, which have to be performed on thin sections by a fabric analyzer in transmitting light. As the latter is capable to map sublimation grooves at low resolution, the application of both acquisition methods on thin sections can reduce inaccuracies associated with the present matching algorithm.

Every processing step on the sublimation groove images can be verified by / compared with the extracted grain boundaries from measurements of *c*-axes orientation. Occasionally, the algorithm to remove vertical scratches (caused during polishing of the surface) label grain boundaries as artifacts. Based on the matched image pairs, the influence of this algorithm on the agreement of extracted grain boundaries has been quantified. Generally, it has become possible to reconsider the choice of parameters and thresholds used throughout the image processing approach in a systematic way.

In addition to grains and grain boundaries, also sub-grain boundaries have been extracted from sublimation groove images by the developed image processing approach. However, this part of the processing is in an early stage of development. A comparison between automatic and previously performed manual extraction (Weikusat *et al.* , 2009b) shows that typically only half of the sub-grain boundaries is detected. This discrepancy has been traced back to the inadequacy of the present method to separately detect sub-grain boundaries in close vicinity. As solving this problem by means of anisotropic diffusion is associated with a drastic increase in computing effort, it seems more appropriate to first examine whether improved image acquisition is sufficient. As the sublimation grooves at the site of sub-grain boundaries are represented by gray values similar to those inside grains, an increased contrast could enable their automatic extraction.

Owing to the fine resolution in the position of grain boundaries, much smaller grains can be extracted from sublimation groove images in comparison to *c*-axes measurements. This raises the question how many of the small grains should be considered for the calculation of the mean grain size. A lower cut-off has been defined based on the area fraction of considered grain cross-sections to limit the influence of small-grain artifacts. A comparison of grain growth rates derived from the EDML and NEEM data sets by means of this cut-off to previously derived growth rates suggests that more small grains than previously are considered. This allows measuring the development of a second mode of smaller grains which has previously been identified, but not measured (e. g., Svensson *et al.* , 2003).

Comparison of grain geometry data from the NEEM ice core with results from continuous flow analysis revealed a correlation between the occurrence of small grains and the dust content at 320 m depth. 10 meters below, a thin band of larger grains (increased by a factor of 10) appears to correlate with a high concentration of ammonium. These examples highlight that one mean values in grain size for an entire section or even a wider range do not reflect the mechanism-related variability on mm and cm scale adequately. The evolution of grain shape with depth has been analyzed. Changes in trend can partially be attributed to the presence of effective negative pressures caused by air bubbles and clathrate hydrates. Significant differences between the profiles of the NEEM and EDML ice cores are observed. Apart from methodical differences, deviations can be explained by the difference in age scales between both ice cores, which suggest that recovery is more effective along the EDML ice core. The obtained densities of sub-grain boundaries (derived from sublimation grooves) confirms this conclusion which is in good agreement with a previous comparison of the EDML ice core to experimentally deformed ice (Weikusat *et al.* , 2009a).

For the NEEM ice core, high sub-grain boundary densities coincide with stratigraphic layers visible in radar profiles. Those layers are characterized by a high concentration of impurities (Svensson *et al.* , 2005), which confirms that a sound understanding of the coupling between different aspects of multi-scale variability (Faria *et al.* , 2009) is required to develop an improved micro-dynamical basis for mean-field approaches in ice sheet modeling. The presented method enables an objective quantification of consistency and deviations between microstructural observations in nature, deformation experiments and simulations.

References

- Adams, R., & Bischof, L. 1994. Seeded Region Growing. *IEEE Trans. Pattern Anal. Mach. Intell.*, **16**, 641–647.
- Alley, R.B. 1992. Flow-law hypotheses for ice-sheet modeling. *J. Glaciol.*, **38**, 245–256.
- Alley, R.B., & Woods, G.A. 1996. Impurity influence on normal grain growth in the GISP2 ice core, Greenland. *J. Glaciol.*, **42**, 255–260.
- Alley, R.B., Perepezko, J.H., & Bentley, C.R. 1986a. Grain growth in polar ice: I. Theory. *J. Glaciol.*, **32**, 415–424.
- Alley, R.B., Perepezko, J.H., & Bentley, C.R. 1986b. Grain growth in polar ice: II. Application. *J. Glaciol.*, **32**, 425–433.
- Alley, R.B., Gow, A.J., & Meese, D.A. 1995. Mapping c-axis fabrics to study physical processes in ice. *J. Glaciol.*, **41**, 197–203.
- Anderson, M.P., Grest, G.S., & Srolovitz, D.J. 1989. Computer simulation of normal grain growth in three dimensions. *Philos. Mag. B*, **59**, 293–329.
- Arnaud, L., Gay, M., Barnola, J.M., & Duval, P. 1998. Imaging of firm and bubbly ice in coaxial reflected light: a new technique for the characterization of these porous media. *J. Glaciol.*, **44**, 326–332.
- Ashby, M.F., & Duval, P. 1985. The Creep of Polycrystalline Ice. *Cold Reg. Sci. Technol.*, **11**, 285–300.

- Azuma, N., & Higashi, A. 1985. Formation processes of ice fabric pattern in ice sheets. *Ann. Glaciol.*, **6**, 130–134.
- Azuma, N., Wang, Y., Yoshida, Y., Narita, H., Hondoh, T., Shoji, H., & Watanabe, O. 2000. Crystallographic analysis of the Dome Fuji ice core. *Pages 45–61 of: Hondoh, T. (ed), Physics of Ice Core Records.*
- Bartels, R.H., Beatty, J.C., & Barsky, B.A. 1998. *An Introduction to Splines for Use in Computer Graphics and Geometric Modeling.* San Francisco, CA: Morgan Kaufmann.
- Bartozzi, M., Boyle, A.P., & Prior, D.J. 2000. Automated grain boundary detection and classification in orientation contrast images. *J. Struct. Geol.*, **22**, 1569–1579.
- Bendel, V., Ueltzhöffer, K.J., Freitag, J., Kipfstuhl, S., Kuhs, W.F., Garbe, C.S., & Faria, S.H. 2013. High-resolution variations in size, number and arrangement of air bubbles in the EPICA DML (Antarctica) ice core. *J. Glaciol.*, **59**, 972–980.
- Binder, T. 2011. Microstructure Analysis of Polar Ice Cores by Means of Digital Image Processing. *Diploma Thesis*, Universität Heidelberg.
- Binder, T., Garbe, C.S., Wagenbach, D., Freitag, J., & Kipfstuhl, S. 2013a. Extraction and parametrization of grain boundary networks in glacier ice, using a dedicated method of automatic image analysis. *J. Microsc.*, **250**, 130–141.
- Binder, T., Weikusat, I., Freitag, J., Garbe, C.S., Wagenbach, D., & Kipfstuhl, S. 2013b. Microstructure through an ice sheet. *Mater. Sci. Forum*, **753**, 481–484.
- Bischoff, A. 2011. Mikrostrukturanalyse von Eisbohrkernbildern mit Hilfe digitaler Bildverarbeitung. *Bachelor Thesis*, Universität Heidelberg.
- Bons, P.D., Jessell, M.W., Evans, L., Barr, T., & Stüwe, K. 2001. Modelling of anisotropic grain growth in minerals. *Pages 39–49 of: Koyi, H.A., & Manck-*

- telow, N.S. (eds), *Tectonic modeling: a volume in honor of Hans Ramberg*. GSA Memoirs, vol. 193. Geological Society of America.
- Bons, P.D., Koehn, D., & Jessell, M.W. 2008. *Microdynamic Simulation*. Lecture notes in earth sciences, vol. 106. Springer, Berlin.
- Breiman, L. 2001. Random forests. *Mach. Learn.*, **45**, 5–32.
- Budd, W.F., & Jacka, T.H. 1989. A review of ice rheology for ice sheet modelling. *Cold Reg. Sci. Technol.*, **16**, 107–144.
- Burke, J.E., & Turnbull, D. 1952. Recrystallization and grain growth. *Pages 220–292 of: Progress in Metal Physics*. Pergamon Press.
- Calle, M.Luz, & Urrea, V. 2010. Letter to the Editor: Stability of Random Forest importance measures. *Brief. Bioinform.*, **12**, 86–89.
- Castelnau, O., Duval, P., Montagnat, M., & Brenner, R. 2008. Elastoviscoplastic micromechanical modeling of the transient creep of ice. *J. Geophys. Res.*, **113**, B11203.
- Chazallon, B., & Kuhs, W.F. 2002. In situ structural properties of N₂-, O₂-, and air-clathrates by neutron diffraction. *Journal of Chemical Physics*, **117**, 308–320.
- Crowley, J.L., & Demazeau, Y. 1993. Principles and Techniques for Sensor Data Fusion. *Signal Processing*, **32**, 5–27.
- Cuffey, K.M., & Paterson, W.S.B. 2010. *The Physics of Glaciers*. 4th edn. Elsevier.
- Dahl-Jensen, D., Gundestrup, N., Miller, H., Watanabe, O., Johnson, S.J., Steffensen, J.P., Clausen, H.B., Svensson, A., & Larsen, L.B. 2002. The NorthGRIP deep drilling programme. *Ann. Glaciol.*, **35**, 1–4.
- Dansgaard, W., & Johnson, S.J. 1969. A flow model and time scale for the ice core from Camp Century, Greenland. *J. Glaciol.*, **8**, 215–223.

- De Bresser, J.H.P., Ter Heege, J.H., & Spiers, C.J. 2001. Grain size reduction by dynamic recrystallization: can it result in major rheological weakening? *Int. J. Earth Sci. (Geol Rundsch)*, **90**, 28–45.
- De La Chapelle, S., Castelnau, O., Lipenkov, V., & Duval, P. 1998. Dynamic recrystallization and texture development in ice as revealed by the study of deep ice cores in Antarctica and Greenland. *J. Geophys. Res.*, **103**, 5091–5106.
- Drury, M.R., & Urai, J.L. 1990. Deformation-related recrystallization processes. *Tectonophysics*, **172**, 235–253.
- Durand, G., Graner, F., & Weiss, J. 2004. Deformation of grain boundaries in polar ice. *Europhysics Letter*, **67**, 1038–1044.
- Durand, G., Weiss, J., Lipenkov, V., Barnola, J.M., Krinner, G., Parrenin, F., Delmonte, B., Ritz, C., Duval, P., Röthlisberger, R., & Bigler, M. 2006a. Effect of impurities on grain growth in cold ice sheets. *J. Geophys. Res.*, **111**, F01015.
- Durand, G., Gagliardini, O., Thorsteinsson, T., Svensson, A., & Dahl-Jensen, D. 2006b. Ice microstructure and fabric: An up to date approach for measuring textures. *J. Glaciol.*, **52**, 619–630.
- Durand, G., Svensson, A., Persson, A., Gagliardini, O., Gillet-Chaulet, F., Sjolte, J., & Dahl-Jensen, D. 2009. Evolution of the Texture along the EPICA Dome C Ice Core. *Pages 91–113 of: Hondoh, T. (ed), Physics of Ice Core Records II*, vol. 68.
- Duval, P. 1985. Grain growth and mechanical behaviour of polar ice. *Ann. Glaciol.*, **6**, 79–82.
- Duval, P., & Castelnau, O. 1995. Dynamic recrystallization of ice in polar ice sheets. *J. Phys IV*, **5**, 197–205.
- Duval, P., & Lorius, C. 1980. Crystal size and climatic record down to the last ice age from Antarctic ice. *Earth Planet. Sci. Lett.*, **48**, 59–64.

- Duval, P., Ashby, M.F., & Anderman, I. 1983. Rate controlling processes in the creep of polycrystalline ice. *Journal of Physical Chemistry*, **87**, 4066–4074.
- Eichler, J. 2013. C-axis analysis of the NEEM ice core - An approach based on digital image processing. *Diploma Thesis*, Freie Universität Berlin.
- Ekaykin, A.A., Lipenkov, V.Y., Barkov, N.I., Petit, J.R., & Masson-Delmotte, V. 2002. Spatial and temporal variability in isotope composition of recent snow in the vicinity of Vostok station, Antarctica: implications for ice-core record interpretation. *Ann. Glaciol.*, **35**, 181–186.
- EPICA community members. 2004. Eight glacial cycles from an Antarctic ice core. *Nature*, **429**, 623–628.
- Ettema, J., van den Broeke, M.R., van Meijgaard, E., van de Berg, W.J., Bamber, J.L., Box, J.E., & Bales, R.C. 2009. Higher surface mass balance of the Greenland ice sheet revealed by high-resolution climate modeling. *Geophysical Research Letters*, **36**, L12501.
- Faria, S.H., & Kipfstuhl, S. 2004. Preferred slip band orientations and bending observed in the Dome Concordia ice core. *Ann. Glaciol.*, **39**, 386–390.
- Faria, S.H., Azuma, N., Freitag, J., Weikusat, I., Murshed, M.M., & Kuhs, W.F. 2009. The Multiscale Structure of Antarctica Part I: Inland Ice. *Pages 39–59 of: Hondoh, T. (ed), Physics of Ice Core Records II*, vol. 68.
- Faria, S.H., Freitag, J., & Kipfstuhl, S. 2010. Polar ice structure and the integrity of ice-core paleoclimate records. *Journal of Quaternary Science Reviews*, **29**, 338–351.
- Faria, S.H., Weikusat, I., & Azuma, N. 2013a. The Microstructure of Polar Ice. Part I: Highlights from Ice Core Research. *J. Struct. Geol.*
- Faria, S.H., Weikusat, I., & Azuma, N. 2013b. The Microstructure of Polar Ice. Part II: State of the Art. *J. Struct. Geol.*

- Fischler, M.A., & Bolles, R.C. 1981. Random Sample Consensus: A Paradigm for Model Fitting with Applications to Image Analysis and Automated Cartography. *Communications of the ACM*, **24**, 381–395.
- Fisher, D.A., & Koerner, R.M. 1986. On the special rheological properties of ancient, microparticle-laden northern-hemisphere ice as derived from bore-hole and core measurements. *J. Glaciol.*, **32**, 501–510.
- Fitzgibbon, A.W., Pilu, M., & Fisher, R.B. 1996. Direct least-square fitting of Ellipses. *In: International Conference on Pattern Recognition*.
- Förstner, W. 1986. A Feature Based Corresponding Algorithm for Image Matching. *Int. Arch. Photogramm. Remote Sens.*, **26**, 150–166.
- Freeman, B., & Ferguson, C.C. 1986. Deformation mechanism maps and micro-mechanics of rocks with distributed grain sizes. *J. Geophys. Res.*, **91(B)**, 3849–3860.
- Fuhrer, K., Neftel, A., Anklin, M., & Maggi, V. 1993. Continuous measurements of hydrogen peroxide, formaldehyde, calcium and ammonium concentrations along the new GRIP ice core from summit, central Greenland. *Atmos. Environ. Part A*, **27**, 1873–1880.
- Gagliardini, O., Durand, G., & Wang, Y. 2004. Grain area as a statistical weight for polycrystal constituents. *J. Glaciol.*, **50**, 87–95.
- Gauss, C.F. 1887. *Abhandlungen zur Methode der kleinsten Quadrate*. Berlin. Pages 1–91.
- Gay, M., & Weiss, J. 1999. Automatic reconstruction of polycrystalline ice microstructure from image analysis: application to the EPICA ice core at Dome Concordia, Antarctica. *J. Glaciol.*, **45**, 547–554.
- Glen, J.W. 1955. The Creep of Polycrystalline Ice. *Proc. Roy. Soc. A*, **228**, 519–538.

- Glen, J.W. 1968. The Effect of Hydrogen Disorder on Dislocation Movement and Plastic Deformation of Ice. *Phys. kondens. Materie*, **7**, 43–51.
- Gogineni, P. *CReSIS Radar Depth Sounder Data, Lawrence, Kansas, USA*.
- Gow, A.J. 1969. On the rates of growth of grains and crystals in south polar firn. *J. Glaciol.*, **8**, 241–252.
- Gow, A.J. 1971. Relaxation of Ice in Deep Drill Cores from Antarctica. *J. Geophys. Res.*, **76**, 2533–2541.
- Gow, A.J., & Williamson, T. 1976. Rheological implications of the internal structure and crystal fabrics of the West Antarctic ice sheet as revealed by deep core drilling at Byrd station. *CRREL Report*, 76–35.
- Gow, A.J., Meese, D.A., Alley, R.B., Fitzpatrick, J.J., Anandakrishnan, S., Woods, G.A., & Elder, B.C. 1997. Physical and structural properties of the Greenland Ice Sheet Project 2 ice core: A review. *J. Geophys. Res.*, **102**, 26,559–26,575.
- Harris, C.G., & Stevens, M.J. 1988. A Combined Corner and Edge Detector. *In: Proc. of 4th Alvey Vision Conference*.
- Heilbronner, R. 2000. Automatic grain boundary detection and grain size analysis using polarization micrographs or orientation images. *J. Struct. Geol.*, **22**, 969–981.
- Heilbronner, R., & Barrett, S. 2013. *Image Analysis in Earth Sciences*. Springer.
- Herwegh, M. 2000. A new technique to automatically quantify microstructures of fine grained carbonate mylonites: two-step etching combined with SEM imaging and image analysis. *J. Struct. Geol.*, **22**, 391–400.
- Herwegh, M., De Bresser, J.H.P., & Ter Heege, J.H. 2005. Combining natural microstructures with composite flow laws: an improved approach for the extrapolation of lab data to nature. *J. Struct. Geol.*, **27**, 503–521.

- Hillert, M. 1965. On the theory of normal and abnormal grain growth. *Acta Metallurgica*, **13**, 227–238.
- Hirth, J.P., & Lothe, J. 1992. *Theory of Dislocations*. 2nd edn. Krieger Publishing Company, Malabar, FL.
- Hörhold, M.W., Laepple, T., Freitag, J., Bigler, M., Fischer, H., & Kipfstuhl, S. 2012. On the impact of impurities on the densification of polar firn. *Earth Planet. Sci. Lett.*, **325-326**, 93–99.
- Horn, M. 2009. Ein Linescanner zur Erfassung von Korngrößenparametern: Entwicklung, Aufbau und Anwendung. *Diploma Thesis*, Universität Bremen.
- Howat, I.M., Ahn, Y., Joughin, I., van den Broeke, M.R., Lenaerts, J.T.M., & Smith, B. 2011. Mass balance of Greenland’s three largest outlet glaciers, 2000-2010. *Geophysical Research Letters*, **38**, L12501.
- Humphreys, F.J., & Hatherly, M. 2004. *Recrystallization and Related Annealing Phenomena*. 2nd edn. Elsevier.
- Jarvis, R.A. 1973. On the identification of the convex hull of a finite set of points in the plane. *Information Processing Letters*, **2**, 18–21.
- Jessell, M., Bons, P., Evans, L., Barr, T., & Stüwe, K. 2001. Elle: the numerical simulation of metamorphic and deformation microstructures. *Comput. Geosci.*, **27**, 17–30.
- Jessell, M.W., & Bons, P.D. 2002. *Deformation Mechanisms, Rheology and Tectonics: Current Status and Future Perspectives*. Spec. Publ., vol. 200. Geol. Soc, London. Chap. The numerical simulation of microstructure, pages 1137–1147.
- Kameda, T., Shoji, H., Kawada, K., Watanabe, O., & Clausen, H.B. 1994. An empirical relation between overburden pressure and firn density. *J. Glaciol.*, **20**, 87–94.

- Kaufmann, P.R., Federer, U., Hutterli, M.A., Bigler, M., Schüpfbach, S., Ruth, U., Schmidt, J., & Stocker, T.F. 2008. An Improved Continuous Flow Analysis System for High-Resolution Field Measurements on Ice Cores. *Environ. Sci. Technol.*, **42**, 8044–8050.
- Kipfstuhl, S., Pauer, F., Kuhs, W.F., & Shoji, H. 2001. Air bubbles and clathrate hydrates in the transition zone of the NGRIP deep ice core. *Geophysical Research Letters*, **28**, 591–594.
- Kipfstuhl, S., Hamann, I., Lambrecht, A., Freitag, J., Faria, S.H., Grigoriev, D., & Azuma, N. 2006. Microstructure mapping: a new method for imaging deformation-induced microstructural features of ice on the grain scale. *J. Glaciol.*, **52**, 398–406.
- Kipfstuhl, S., Faria, S.H., Azuma, N., Freitag, J., Hamann, I., Kaufmann, P., Miller, H., Weiler, K., & Wilhelms, F. 2009. Evidence of dynamic recrystallization in polar firn. *J. Geophys. Res.*, **114**, B05204.
- Köthe, U. 1995. Primary Image Segmentation. *Pages 554–561 of: Sagerer, G., Posch, S., & Kummert, F. (eds), Mustererkennung, 17th DAGM Symposium.* Springer-Verlag, London.
- Köthe, U. 2003. Integrated Edge and Junction Detection with the Boundary Tensor. *Pages 424–431 of: Proc. 9th Intl. Conf. Computer Vision.*
- Kruhl, J.H. 1996. Prism- and basal-plane parallel subgrain boundaries in quartz: a microstructural geothermobarometer. *J. metamorphic Geol.*, **14**, 581–589.
- Kuntcheva, B., Kruhl, J.H., & Kunze, K. 2006. Crystallographic orientations of high-angle grain boundaries in dynamically recrystallized quartz: First results. *Tectonophysics*, **421**, 331–346.
- Kuroiwa, D., & Hamilton, W.L. 1963. Studies of ice etching and dislocation etch pits. *Pages 34–55 of: Kingery, W.D. (ed), Ice and snow: properties, processes, and applications.* Cambridge, MA: MIT Press.

- Lambert, F., Delmonte, B., Petit, J.R., Bigler, M., Kaufmann, P.R., Hutterli, M.A., Stocker, T.F., Ruth, U., Steffensen, J.P., & Maggi, V. 2008. Dust2climate couplings over the past 800,000 years from the EPICA Dome C ice core. *Nature*, **452**, 616–619.
- Langway, Jr., C.C. 1958. Ice fabrics and the universal stage. *SIPRE Tech. Rep.*
- Lindeberg, T. 1994. *Scale-Space Theory in Computer Vision*. Kluwer.
- Lipenkov, V., Salamatin, A.N., & Duval, P. 1997. Bubbly-ice densification in ice sheets: II. Applications. *J. Glaciol.*, **43**, 397–407.
- Miller, S.L. 1969. Clathrate Hydrates of Air in Antarctic Ice. *Science*, **165**, 489–490.
- Miyamoto, A., Saito, T., & Hondoh, T. 2009. Visual Observation of Volume Relaxation under Different Storage Temperatures in the Dome Fuji Ice Core, Antarctica. *Pages 73–79 of: Hondoh, T. (ed), Physics of Ice Core Records II*, vol. 68.
- Montagnat, M., & Duval, P. 2000. Rate controlling processes in the creep of polar ice: influence of grain boundary migration associated with recrystallization. *Earth Planet. Sci. Lett.*, **183**, 179–186.
- Montagnat, M., Castelnau, O., Bons, P.D., Faria, S.H., Gagliardini, O., Gillet-Chaulet, F., Grennerat, F., Grier, A., Lebensohn, R.A., Moulinec, H., Roesiger, J., & Suquet, P. 2013. Multiscale modeling of ice deformation behavior. *J. Struct. Geol.*
- Montagnat, M., Azuma, N., Dahl-Jensen, D., Eichler, J., Fujita, S., Gillet-Chaulet, F., Kipfstuhl, S., Samyn, D., Svensson, A., & Weikusat, I. 2014. Fabric measurement along the NEEM ice core, Greenland, and comparison with GRIP and NGRIP ice cores. *The Cryosphere Discuss.*, **8**, 307–335.
- Mullins, W.W. 1957. Theory of thermal grooving. *J. Appl. Phys.*, **28**, 333–339.

- NEEM community members. 2013. Eemian interglacial reconstructed from a Greenland folded ice core. *Nature*, **493**, 489–494.
- Nye, J.F. 1953. The Flow Law of Ice from Measurements in Glacier Tunnels, Laboratory Experiments and the Jungfraufirn Borehole Experiment. *Proc. Roy. Soc. A*, **219**, 477–489.
- Ohno, H., Lipenkov, V., & Hondoh, T. 2004. Air bubble to clathrate hydrate transformation in polar ice sheets: A reconsideration based on the new data from Dome Fuji ice core. *Geophysical Research Letters*, **31**, L21401.
- Olgaard, D.L., & Evans, B. 1986. Effect of Second-Phase Particles on Grain Growth in Calcite. *J. Am. Ceram. Soc.*, **69**, C272–C277.
- Orowan, E. 1934. *Z. Physik*, **89**, 605, 614, 634.
- Parrenin, F., Dreyfus, G., Durand, G., Fujita, S., Gagliardini, O., Gillet, F., Jouzel, J., Kawamura, K., Lhomme, N., Masson-Delmotte, V., Ritz, C., Schwander, J., Shoji, H., Uemura, R., Watanabe, O., & Yoshida, N. 2007. 1-D-ice flow modelling at EPICA Dome C and Dome Fuji, East Antarctica. *Clim. Past*, **3**, 243–259.
- Pilu, M., Fitzgibbon, A.W., & Fisher, R.B. 1996. Ellipse-specific Direct least-square Fitting. *In: IEEE International Conference on Image Processing*.
- Rasmussen, S.O., Abbott, P., Blunier, T., Bourne, A., Brook, E., Buchardt, S.L., Bulzert, C., Chappellaz, J., Clausen, H.B., Cook, E., Dahl-Jensen, D., Davies, S., Guillevic, M., Kipfstuhl, S., Laepple, T., Selerstad, I.K., Severinghaus, J.P., Stowasser, C., Svensson, A., Vallelonga, P., Vinther, B.M., Wilhelms, F., & Winstrup, M. 2013. A first chronology for the NEEM ice core. *Clim. Past Discuss.*, **9**, 2967–3013.
- Read, W.T., & Shockley, W. 1950. Dislocation Models of Crystal Grain Boundaries. *Phys. Rev.*, **78**, 275–289.

- Ren, X., & Malik, J. 2003. Learning a Classification Model for Segmentation. *Pages 10–17 of: Proc. 9th Intl. Conf. Computer Vision.*
- Richardson, L.F. 1911. The approximate arithmetical solution by finite differences of physical problems including differential equations, with an application to the stresses in a masonry dam. *Phil. Trans. R. Soc. Lond. A*, **210**, 307–357.
- Riesterer, J.L. 2009. Reconstructing Oxide Surfaces. *PhD Thesis*, University of Minnesota.
- Roessiger, J., Bons, P.D., & Faria, S.H. 2013. Influence of bubbles on grain growth in ice. *J. Struct. Geol.*
- Röthlisberger, R., Bigler, M., Hutterli, M., Sommer, S., Stauffer, B., Junghans, H., & Wagenbach, D. 2000. Technique for continuous high-resolution analysis of trace substances in firn and ice cores. *Environ. Sci. Technol.*, **34**, 338–342.
- Ruth, R., Wagenbach, D., Steffensen, J., & Bigler, M. 2003. Continuous record of microparticle concentration and size distribution in the central Greenland NGRIP ice core during the last glacial period. *J. Geophys. Res.*, **108**, 4098.
- Ruth, U., Barnola, J.-M., Beer, J., Bigler, M., Blunier, T., Castellano, E., Fischer, H., Fundel, F., Huybrechts, P., Kaufmann, P., Kipfstuhl, S., Lambrecht, A., Morganti, A., Oerter, H., Parrenin, F., Rybak, O., Severi, M., Udisti, R., Wilhelms, F., & Wolff, E. 2007. "EDML1": a chronology for the EPICA deep ice core from Dronning Maud Land, Antarctica, over the last 150 000 years. *Clim. Past*, **3**, 475–484.
- Sammonds, P.R. 1999. Understanding the fundamental physics governing the evolution and dynamics of the Earth's crust and ice sheets. *Phil. Trans. R. Soc. Lond. A*, **357**, 3377–3401.
- Saylor, D.M., & Rohrer, G.S. 1999. Measuring the influence of grain-boundary misorientation on thermal groove geometry in ceramic polycrystals. *J. Am. Ceram. Soc.*, **82**, 1529–1565.

- Serra, J.P., & Cressie, N.A. 1982. *Image Analysis and Mathematical Morphology*. Academic Press.
- Shepherd, A., Ivins, E.R., A, G., Barletta, V.R., Bentley, M.J., Bettadpur, S., Briggs, K.H., Bromwich, D.H., Forsberg, R., Galin, N., Horwath, M., Jacobs, S., Joughin, I., King, M.A., Lenaerts, J.T.M., Li, J., Ligtenberg, S.R.M., Luckman, A., Luthcke, S.B., McMillan, M., Meister, R., Milne, G., Mouginot, J., Muir, A., Nicolas, J.P., Paden, J., Payne, A.J., Pritchard, H., Rignot, E., Rott, H., Sørensen, L.S., Scambos, T.A., Scheuchl, B., Schrama, E.J.O., Smith, B., Sundal, A.V., van Angelen, J.H., van de Berg, W.J., van den Broeke, M.R., Vaughan, D.G., Velicogna, I., Wahr, J., Whitehouse, P.L., Wingham, D.J., Yi, D., Young, D., & Zwally, H.J. 2012. A Reconciled Estimate of Ice-Sheet Mass Balance. *Science*, **338**, 1183–1189.
- Spaulding, N.E., Meese, D.A., Baker, I., Mayewski, P.A., & Hamilton, G.S. 2010. A new technique for firn grain-size measurements using SEM image analysis. *J. Glaciol.*, **55**, 12–19.
- Stephenson, P.J. 1967. Some considerations of snow metamorphism in the Antarctic ice sheet in the light of ice crystal studies. *Physics of Snow and Ice*, **1**, 725–740.
- Svensson, A., Schmidt, K.G., Dahl-Jensen, D., Johnson, S.J., Wang, Y., Kipfstuhl, S., & Thorsteinsson, T. 2003. Properties of ice crystals in NorthGRIP late- to middle-Holocene ice. *Ann. Glaciol.*, **37**, 113–118.
- Svensson, A., Nielsen, S.W., Kipfstuhl, S., Johnson, S.J., Steffensen, J.P., Bigler, M., Ruth, U., & Röthlisberger, R. 2005. Visual stratigraphy of the North Greenland Ice Core Project (North-GRIP) ice core during the last glacial period. *J. Geophys. Res.*, **110**, D02108.
- Svensson, A., Durand, G., Mathiesen, J., Persson, A., & Dahl-Jensen, D. 2009. Texture of the Upper 1000m in the GRIP and NorthGRIP IceCores. *Pages 107–113 of: Hondoh, T. (ed), Physics of Ice Core Records II*, vol. 68.

- Thorsteinsson, Th., Kipfstuhl, J., Eicken, H., Johnson, S.J., & Fuhrer, K. 1995. Crystal size variations in Eemian-age ice from the GRIP ice core, Central Greenland. *Earth Planet. Sci. Lett.*, **131**, 381–394.
- Thorsteinsson, Th., Kipfstuhl, S., & Miller, H. 1997. Textures and fabrics in the GRIP ice core. *J. Geophys. Res.*, **102**, 26583–26599.
- Trepied, L., Doukhan, J.C., & Paquet, J. 1980. Subgrain Boundaries in Quartz Theoretical Analysis and Microscopic Observations. *Phys. Chem. Minerals*, **5**, 201–218.
- Uchida, T., Hondoh, T., Mae, S., Lipenkov, V., & Duval, P. 1994. Air-hydrate crystals in deep ice-core amples from Vostok Station, Antarctica. *J. Glaciol.*, **40**, 79–86.
- Ueltzhöffer, K. 2009. Microstructure Analysis of Polar Ice Cores by Means of Digital Image Processing. *Diploma Thesis*, Universität Heidelberg.
- Ueltzhöffer, K.J., Bendel, V., Freitag, J., Kipfstuhl, S., Wagenbach, D., Faria, S.H., & Garbe, C.S. 2010. Distribution of air bubbles in the EDML and EDC (Antarctica) ice cores, using a new method of automatic image analysis. *J. Glaciol.*, **56**, 339–348.
- Valcke, S.L.A., Pennock, G.M., Drury, M.R., & De Bresser, J.H.P. 2006. Electron backscattered diffraction as a tool to quantify subgrains in deformed calcite. *J. Microsc.*, **224**, 264–276.
- Vincent, L., & Soille, P. 1991. Watersheds in Digital Spaces: An Efficient Algorithm Based on Immersion Simulations. *IEEE Trans. Pattern Anal. Mach. Intell.*, **13**, 583–598.
- Voss, B., Stapf, J., Berthe, A., & Garbe, C.S. 2012. Bichromatic particle streak velocimetry bPSV. *Exp Fluids*, **53**, 1405–1420.
- Wang, Y., & Azuma, N. 1999. A new automatic ice-fabric analyzer which

- uses image-analysis techniques A new automatic ice-fabric analyzer which uses image-analysis techniques. *Ann. Glaciol.*, **29**, 155–162.
- Wang, Y., Kipfstuhl, S., Azuma, N., Thorsteinsson, Th., & Miller, H. 2003. Ice-fabrics study in the upper 1500 m of the Dome C (East Antarctica) deep ice core. *Ann. Glaciol.*, **37**, 97–104.
- Weertman, J., & Weertman, J.R. (eds). 1992. *Elementary Dislocation Theory*. Oxford University Press, New York.
- Weickert, J. 1998. *Anisotropic Diffusion in Image Processing*. ECMI Series. Stuttgart, Germany: Teubner-Verlag.
- Weikusat, I., Kipfstuhl, S., Azuma, N., Faria, S.H., & Miyamoto, A. 2009a. Deformation Microstructures in an Antarctic Ice Core (EDML) and in Experimentally Deformed Artificial Ice. *Pages 115–124 of: Hondoh, T. (ed), Physics of Ice Core Records II*, vol. 68.
- Weikusat, I., Kipfstuhl, S., Azuma, N., & Miyamoto, A. 2009b. Subgrain boundaries and related microstructural features in EDML (Antarctica) deep ice core. *J. Glaciol.*, **55**, 461–472.
- Weikusat, I., De Winter, D.A.M., Pennock, G.M., Hayles, M., Schneijdenberg, C.T.W.M., & Drury, M.R. 2011a. Cryogenic EBSD on ice: preserving a stable surface in a low pressure SEM. *J. Microsc.*, **242**, 295–310.
- Weikusat, I., Miyamoto, A., Faria, S.H., Kipfstuhl, S., Azuma, N., & Hondoh, T. 2011b. Subgrain boundaries in Antarctic ice quantified by X-ray Laue diffraction. *J. Glaciol.*, **57**, 111–120.
- Wheeler, J., Prior, D.J., Jiang, Z., Spiess, R., & Trimby, P.W. 2001. The petrological significance of misorientations between grains. *Contrib Mineral Petrol*, **141**, 109–124.
- Wheeler, J., Jiang, Z., Prior, D.J., Tullis, J., Drury, M.R., & Trimby, P.W. 2003. From geometry to dynamics of microstructure: using boundary lengths

- to quantify boundary misorientations and anisotropy. *Tectonophysics*, **376**, 19–35.
- Wilén, L.A. 2000. A new technique for ice-fabric analysis. *J. Glaciol.*, **46**, 129–139.
- Wilén, L.A., Prinzio, C.L. Di, & Azuma, N. 2003. Development, principles, and applications of automated ice fabric analyzers. *Microsc. Res. Techniq.*, **62**, 2–18.
- Wilson, C.J.L., Russell-Head, D.S., & Sim, H.M. 2003. The application of an automated fabric analyzer system to the textural evolution of folded ice layers in shear zones. *Ann. Glaciol.*, **37**, 7–17.
- Woodcock, N.H. 1977. Specification of fabric shapes using an eigenvalue method. *Geol. Soc. Am. Bull.*, **88**, 1231–1236.
- Woods, G.A. 1994. *Grain growth behavior of the GISP2 ice core from central Greenland*. Tech. rept. 94-002. Earth Syst. Sci. Cent., Penns. State Univ.

List of Figures

2-1	Combined image acquisition method	9
2-2	Visible features in sublimation groove images	11
2-3	Estimation of minimal depth of field (EDML)	12
2-4	Scanning error, deviation in vertical resolution (NEEM)	14
2-5	Gray values along grain boundaries in sublimation groove images .	16
2-6	Width of sublimation grooves	19
3-1	Detection of vertical scratches and tile borders	35
3-2	Ghost boundaries	36
4-1	Order of grain neighbors for validation of grain pairs	40
4-2	Bijjective mapping between grains	44
4-3	Comparison of local tangent profiles for verification	47
4-4	Considered range around grain boundaries for assignment of c-axes measurements	51
4-5	Sublimation grooves of sub-grain boundaries	53

5-1	Increase of visible pore space during sublimation	64
5-2	Comparison visible pore space (NEEM/EDML)	66
5-3	Parameterization of grain shape	70
5-4	Local tangent orientation along circle, ellipse, and rectangle	74
6-1	Pixel-wise orientation of extracted sub-grain structures	85
6-2	Comparison extracted sub-grain structures (automatic/manual)	87
6-3	Sub-grain structures extracted from sublimation grooves/c-axes measurements	89
7-1	Mean grain size (NEEM/EDML)	96
7-2	Sources of error in grain size parameterization	97
7-3	Growth rates (NEEM/EDML)	100
7-4	Grain size distribution, shallow depth NEEM	100
7-5	Grain size/impurity concentration, NEEM 322 m/333 m)	102
7-6	Derivation of vertical strain rate from annual layers (NEEM)	103
7-7	Mean perimeter ratio (NEEM/EDML)	108
7-8	Mean curvature/difference dislocation density (NEEM/EDML)	111
7-9	Sub-grain boundary pinning	112
7-10	Mean sub-grain boundary density (NEEM/EDML)	114

List of Tables

4.1	Estimation of mismatches	42
4.2	Coverage of matched grains	48
4.3	Properties of missing/unextracted grain boundaries	50
4.4	Properties of artificial grain boundaries	52
5.1	Analysis grain size cut-off, manual correction	59
5.2	Error mean grain size, missing grain boundaries	61
5.3	Error mean grain size, artificial grain boundaries	62
5.4	Performance analysis for identification of vertical scratches	68

Acknowledgements

I am looking back on exciting years and would like to thank all of those who gave me the opportunity to gain experience in so many areas. Especially the multitude of personal contacts motivated me to challenge the adventure science. I fear that I will wake up tomorrow with the realization that my acknowledgments are incomplete. If you feel addressed: “Thank you for your support!”

I would like to thank my supervisor, PD Dr. Christoph Garbe, for his scientific guidance, professional support and constant availability. Being member of his working group was a pleasure. Whenever I traveled around the world, even in the far south, “Image Processing and Modeling” was my scientific home.

During the work on this thesis it became apparent that interdisciplinary connections had to be established and I encountered so many open doors.

I felt that doors at AWI were wide open. Ilka Weikusat, Sepp Kipfstuhl, Daniela Jansen, Johannes Freitag, Andreas Frenzel, Frank Wilhelms, and many others offered their support and advice. In particular, during the last weeks you kept me alive.

Equally open doors I found at IUP. I have never seen Dietmar Wagenbach’s door closed and would like to thank him for valuable discussions and advice for occasional re-adjustment of scientific navigation instruments. Thanks even to Johanna Kerch for being and organizing important help in the final stage of this thesis.

I would also like to thank Paul Bons, Sérgio Faria, Anders Svensson, Hans de Bresser, Nobuhiko Azuma and Denis Samyn for fruitful discussions and new impulses.

I hope very much that these acknowledgments do not mean an end, but rather a starting signal!

Of course, there is a life outside science. Thanks to my family and friends for all the support I experienced and the understanding of my prioritization during the last months. The signs may hopefully change soon.

Special thanks are directed to Daniel Ritter who forced me to maintain daily and weekly routines and to struggle against laziness.

I gratefully acknowledge support from the German Science Foundation (DFG) through the grant GA1271/8-1 within the Priority Program SPP-1158.

NEEM is directed and organized by the Center of Ice and Climate at the Niels Bohr Institute and US NSF, Office of Polar Programs. It is supported by funding agencies and institutions in Belgium (FNRS-CFB and FWO), Canada (NR-Can/GSC), China (CAS), Denmark (FIST), France (IPEV, CNRS/INSU, CEA and ANR), Germany (AWI), Iceland (RannIs), Japan (NIPR), Korea (KOPRI), The Netherlands (NWO/ALW), Sweden (VR), Switzerland (SNF), United Kingdom (NERC) and the USA (US NSF, Office of Polar Programs).

The EDML ice core was drilled within the European Project for Ice Coring in Antarctica (EPICA) programme, a joint European Science Foundation/European Commission scientific programme, funded by the European Union (EPICA-MIS) and by national contributions from Belgium, Denmark, France, Germany, Italy, the Netherlands, Norway, Sweden, Switzerland and the United Kingdom. The main logistic support was provided by the French and Italian polar research institutes, IPEV and PNRA, (at Dome C) and AWI (at Dronning Maud Land).

I gratefully acknowledge travel funding provided by the ESF Research Networking

Programme Micro-Dynamics of Ice (MicroDIce) and by the Heidelberg Graduate School of Mathematical and Computational Methods for the Sciences (GSC 220).

I acknowledge the use of CFA measurements provided by colleagues at the University of Bern.

I acknowledge the use of data from CReSIS generated with support from NSF grant ANT-0424589 and NASA grant NNX10AT68G.